Fall 2018

Multiphase macroscale models for macrosegregation and columnar to equiaxed transition during alloy solidification

Mahdi Torabi Rad
University of Iowa

MULTIPHASE MACROSCALE MODELS FOR MACROSEGREGATION AND COLUMNAR TO EQUIAXED TRANSITION DURING ALLOY SOLIDIFICATION

by

Mahdi Torabi Rad

A thesis submitted in partial fulfillment
of the requirements for the Doctor of Philosophy degree
in Mechanical Engineering
in the Graduate College of
The University of Iowa

Dec. 2018
Thesis Supervisor: Professor Christoph Beckermann

Graduate College
The University of Iowa
Iowa City, Iowa

CERTIFICATE OF APPROVAL

Ph.D. THESIS

This is to certify that the Ph.D. thesis of

Mahdi Torabi Rad

has been approved by the Examining Committee
for the thesis requirement for Doctor of Philosophy
degree in Mechanical Engineering at the December 2018 graduation.

Thesis Committee :

Christoph Beckermann, Thesis Supervisor

H.S. Udaykumar

Pablo M. Carrica

James H.J. Buchholz

Hongtao Ding

To my family

Acknowledgements

First and foremost, I would like to express my sincere gratitude to my academic adviser, Professor Christoph Beckermann, for his valuable guidance and precious comments. The thesis would not have come to a successful completion without his help and continuous support. Also my sincere thanks go to my thesis committee members, Professor Udaykumar, Professor Carrica, Professor Buchholz, and Professor Ding for their time and insightful comments on my dissertation.

I would also like to thank my dear friends at the Solidification Lab for all their help and encouragement. We had great discussions and fun times during the past years.

Last but not the least, I would like to thank my wonderful family. I owe a lot to my parents, Masoumeh and Alyar, and to my sister and brother, Mojdeh and Tohid, for their support throughout my entire life. Words cannot explain how much I love you all!

Abstract

In the field of metal casting, solute composition inhomogeneities at the macroscale are called macrosegregation, and the transition from the elongated grains in the outer portions of a casting to the more rounded grains in the center is termed Columnar to Equiaxed Transition (CET). Simultaneous prediction of macrosegregation and CET is still an important challenge in the field. One of the open questions is the role of melt convection on the CET and the effect of the CET on macrosegregation. A three-phase macroscale model for macrosegregation and CET was developed. The model accounts for numerous phenomena such as columnar dendrite tip undercooling, undercooling behind the columnar tips, and nucleation of equiaxed grains. This three-phase model was used to develop a less complex model that consists of two phases only and disregards undercooling behind the columnar tips and nucleation of equiaxed grains. An in-house parallel computing code on the OpenFOAM platform was developed to solve the equations of these models. The models were used to perform columnar solidification simulations of a numerical benchmark problem. It was found that the predictions of these models are nearly identical. It was also found that the dendrite tip selection parameter, which appears in the constitutive relation for the dendrite tip velocity, plays a key role in these models. With a realistic value for this parameter these models account for columnar dendrite tip undercooling, but as its value is increased in the simulations, predictions of these models converge to predictions of a model that neglects undercooling. Next, the three-phase model was used to perform CET simulations in the numerical solidification benchmark problem in the presence of melt convection. It was found that accounting for stationary equiaxed grains does not change the overall macrosegregation pattern nor the form of channel segregates. Finally, for the first time in the field of solidification, we developed accurate constitutive relations for macroscale solidification models that are based on a formal mesoscale analysis on the scale of a representative elementary volume that is used in developing volume-averaged macroscale models. This upscaling enabled us to present relations that incorporate changes in the shape of grains and solute diffusion conditions around them during growth. The models and constitutive relations we developed can now be used to predict critical phenomena such as macrosegregation, channel segregates, and CET in castings.

Public abstract

The metal casting industry continues to struggle with the formation of defects, which weaken the overall quality of the cast products. Castings are rejected during the quality control stage of the manufacturing process, creating not only significant financial losses for the foundries but also environmental costs. One of the most common defects is macrosegregation. Macrosegregation refers to the solute composition inhomogeneities at the macroscale. Another important phenomena in metal casting is the transition from the elongated grains in the outer portions of a casting to the more rounded grains in the center. Understanding this transition is fundamental to determining what type of grain structure forms in castings of most metal alloys. Predicting macrosegregation and CET before casting a product is therefore critical for the industry. Simultaneous prediction of macrosegregation and the CET is, however, still an important challenge in the field. One of the open questions is the role of melt convection on the CET and the effect of the CET on macrosegregation. In this study, macroscale models for macrosegregation and CET were developed. These models account for numerous phenomena such as liquid undercooling and nucleation of equiaxed grains. The models were used to perform simulations of a numerical solidification benchmark problem. It was found that accounting for undercooling and/or the nucleation of motionless equiaxed grains does not change the overall macrosegregation pattern, but changes the form and number of the predicted channel segregates. Finally, for the first time in the field of solidification, mesoscopic simulation results were upscaled to develop accurate constitutive relations for macroscopic modeling of solidification. This upscaling enabled us to present relations that incorporate changes in the shape of grains and solute diffusion conditions around them during growth.

Table of contents

List of figures

List of nomenclature

$\overline{C}_d$	Solute concentration in the inter-dendritic liquid (wt. pct.)
$\overline{C}_e$	Solute concentration in the extra-dendritic liquid (wt. pct.)
$\overline{C}_l$	Average solute concentration in liquid (wt. pct.)
C_l^*	Equilibrium concentration (wt. pct.)
$\overline{C}_s$	Solute concentration in the solid (wt. pct.)
C_{ref}	Reference solute concentration (wt. pct.)
c_p	Specific heat ($Jkg^{-1}K$)
D_0	solute mass diffusivity in the liquid (m^2s^{-1})
h_{sl}	Latent heat (Jkg^{-1})
$\boldsymbol{g}$	Acceleration due to gravity (ms^{-2})
g_d	Inter-dendritic liquid concentration (-)
g_e	extra-dendritic liquid fraction (-)
g_l	Liquid fraction (-)
g_s	Solid fraction (-)
Iv^{-1}	Inverse Ivantsov function (-)
K	Permeability of the semi-solid mush (m^2)
k_0	Partition coefficient (-)
m_l	Liquidus slope (-)
$\overline{p}$	Average pressure (Nm^2)
Pe	Sphere growth Péclet number (-)
R_e	instantaneous sphere radius (m)
R_f	Final grain radius (m)
S_{env}	average envelope surface area per unit volume of the REV (m^{-1})
T	Temperature (ºC)

T_{ref}	Reference temperature (ºC)
T_{liq}	Liquidus temperature (ºC)
T_{eut}	Eutectic temperature (ºC)
$\bar{\boldsymbol{v}}_l$	Average liquid velocity (ms^{-1})
$\bar{\boldsymbol{v}}_m$	Average mixture velocity (ms^{-1})
w_{env}	Average envelope growth velocity (ms^{-1})

Greek letters

α_0	Thermal diffusivity
β_T	Thermal expansion coefficient (K^{-1})
β_C	Solutal expansion coefficient (wt. $pct.^{-1}$)
Γ	Gibbs-Thomson coefficient (mK)
Γ_{sd}	Mass generation source due to phase change at the sd interface ($kgsm^{-3}$)
Γ_{ed}	Mass generation source due to phase change at the ed interface ($kgsm^{-3}$)
δ_{env}	average diffusion length around the envelope (m)
λ_1	Primary arm spacing (m)
λ_2	Secondary arm spacing (m)
μ_l	Liquid viscosity (Pas)
$\tilde{\rho}_l$	Liquid density in the buoyancy term of the liquid momentum equation (kgm^{-3})
ρ_0	Nominal density (kgm^{-3})
σ^*	Tip selection parameter (-)
Ω_e	Average undercooling in the extra-dendritic liquid (-)
Ω_l	Average undercooling in the liquid (-)

Chapter 1: Introduction

1.1 Background and motivation

The transition from the elongated grains in the outer portions of a casting to the more rounded grains in the center is termed columnar to equiaxed transition (CET). CET has fascinated researchers in the solidification area for more than 50 years (1). Understanding CET is fundamental in determining what type of grain structure forms in castings of most metal alloys. Often, a fully equiaxed structure is preferred, but the fully columnar structure of many turbine blades are an important exception. Realistic modeling and simulation of CET is still very challenging, because it requires one to simultaneously take into account numerous physical phenomena at several length scales: heat/solute transfer, melt flow, nucleation of equiaxed grains, and growth of columnar and equiaxed grains into an undercooled melt.

In the past decade, there have been numerous modeling efforts to address the challenging problem of CET. Most of these efforts are based on the framework developed in the pioneering work of Wang and Beckermann (2). These authors used their framework to develop a model for equiaxed solidification in the presence of melt convection and a model for CET in the absence of melt convection. Martorano et al. (3) used the same framework to develop another model for CET in the absence of melt convection. In addition to disregarding melt convection, these CET models are based on constitutive relations that are overly simplified. For example, these relations do not incorporate the changes in the shape of the equiaxed grains during growth.

1.2 Objective of the present study

The main objectives of this study is to use the framework of Wang and Beckermann (2) to develop a model for CET in the presence of melt convection and to develop more accurate constitutive relations for equiaxed growth. Incorporating melt convection in our CET model, allows one to predict macrosegregation and CET simultaneously. The model that is developed for CET in the presence of melt convection is used to derive a simpler, two-phase model for macrosegregation in

the presence of primary dendrite tip undercooling. These models are analyzed in detail and their predictions are compared with the predictions of a model that is available in the literature and neglects the liquid undercooling entirely. Finally, for the first time in the field of solidification, we developed accurate constitutive relations for macroscale solidification models that are based on a formal mesoscale analysis. This upscaling enabled us to present relations that incorporate changes in the shape of grains and solute diffusion conditions around them during growth.

Chapter 2: Literature Review

In this chapter, the concept of multiphase modeling of solidification is introduced first. Then, the CET and macrosegregation models that are available in the literature are reviewed. It is noted that the literature review in this chapter is intended to provide only the background knowledge that is necessary to understand the rest of the thesis and more detailed review on the specific topics will be provided in the next chapters as they become directly relevant.

2.1 Multiphase macroscale modeling of solidification

Using computational models that can make predictions on the engineering scale is now commonplace in almost every engineering field (4-7). In the field of solidification, computational macroscale models is specifically challenging because realistic macroscopic modeling of solidification requires one to consider phenomena taking place at the microscale and mesoscales. However, with the current available computational resources, it is practically impossible to solve the transport equations at the micro and macro scales simultaneously. To overcome this limitation, a so-called *micro-macroscopic modeling approach* was introduced in the mid-1980s. The main goal in this modeling approach is to incorporate fundamental microscale phenomena (such as nucleation, grain growth, etc.) in the macroscopic transport equations, only to the extent that they influence macroscopic behavior. To develop a macroscopic model that account for microscale phenomena, the microscopic conservation equations for each phase are formally averaged over a *Representative Elementary Volume* (REV). The outcome of this averaging procedure is a volume-averaged macroscopic model where equations contain phase-interaction terms, which represent the effect of microscale phenomena on the macroscopic phenomena, such as columnar-to-equiaxed transition or macrosegregation. The phase interaction terms need to be modeled through constitutive relations.

One of the first volume-averaged solidification models was the two-phase model developed by Ni and Beckermann (8). The model consists of separate volume-averaged conservation equations for

the solid and liquid phases. Different types of growth, i.e. columnar/equiaxed, can be consistently incorporated into the model through the constitutive relations.

Two-phase volume-averaged solidification models cannot *adequately* reflect the microscale phenomena in the final macroscopic equations (9). This is because these models describe the phase behaviors by a single scale averaging, which makes no distinction between properties of phases associated with different microscopic length scales. In dendritic growth, however, there are at least three different microscopic length scales: 1) primary arm spacing, 2) secondary arm spacing, and 3) dendrite tip radius. These scales are all smaller than the characteristic size of an averaging volume. Models based on single scale averaging do not provide sufficient resolution to capture the transport phenomena happening on these multiple length scales. However, such resolution is indeed required for an adequate incorporation of microscopic effects in any macroscopic model. Therefore, there was a need to develop multi-phase/-scale models for solidification.

2.1.1 Multiphase macroscale models of solidification

Wang and Beckermann (10) proposed a multi-phase/-scale macroscopic model for dendritic solidification. The model consists of three phases: 1) solid, 2) inter-dendritic liquid, and 3) extra-dendritic liquid. The two liquid phases are distinguished by their different interfacial length scales; and are separated by a smooth surface connecting the primary and secondary dendrite arm tips, i.e. dendrite envelope. Introducing this new interface enables one to incorporate more microscale details (compared to the two-phase models) in the macroscopic model and transfer information from two different length scales.

Wu and Ludwig developed a five-phase model for mixed columnar/equiaxed solidification (11). These phases include three so-called "thermodynamic phases" and two so-called "hydrodynamic phases". The three distinct thermodynamic phases are: 1) solid, 2) inter-dendritic liquid, and 3) extra-dendritic. The two hydrodynamic phases are: 1) extra-dendritic liquid, and 2) combined solid and inter-dendritic liquid. This indicates that the solid and inter-dendritic liquid phases are assumed to have the same velocity. They later presented a model for globular/dendritic equiaxed

solidification (12) and then improved it further for globular/dendritic mixed equiaxed/columnar solidification (11, 13).

Very recently, Martorano et al. (14) introduced a multi-phase multi-grain model for the equiaxed solidification. The model consists of an extra-dendritic liquid phase and phases representing different classes of grains. Each class of grains consist of grains that have nucleated within a same time interval. Grains in the same class have equal size and growth velocity which is calculated individually for each class.

2.2 Studies on columnar-to-equiaxed transition

The transition from the elongated grains in the outer portions of a casting to more rounded grains in the center in called *Columnar-to-Equiaxed transition* (CET) (15). The equiaxed grains nucleate and grow in the constitutionally undercooled liquid ahead of the moving columnar front. The CET occurs when the equiaxed grains block the movements of the columnar front.

Next, studies on CET are reviewed in two sections: first models to predict CET and then experimental observations of CET.

2.2.1 CET models

Hunt (16) proposed the first CET mechanism which is now referred to as *mechanical-blocking*. The hypothesis behind this mechanism is that equiaxed grains nucleate and grow in the constitutionally undercooled liquid region ahead of the columnar front. If the volume fraction of the equiaxed grains just ahead of the columnar front becomes greater than 0.49, equiaxed grains will mechanically block further advancement of the front; therefore, CET will occur. Hunt's criterion has been widely used in the literature to predict CET, but the mathematical derivation of the criterion is based on empirical equations. Furthermore, Hunt's assumption that the blocking will take place when the equiaxed grain fraction reaches 0.49 is somewhat arbitrary. In fact, Biscuola and Martorano (17) showed that, at least for the Al-Si alloys, using the equiaxed blocking fraction of 0.2 will result in CET predictions that are in better agreement with experiments.

Gandin (18) proposed the concept of *constrained-to-unconstrained* growth transition as a CET mechanism. Growth is considered constrained when the liquid is superheated and its thermal gradient is positive. On the other hand, growth is considered unconstrained when the columnar front reheats the liquid; therefore, makes the temperate gradient in the liquid negative. Gandin developed a one-dimensional model and performed experiments on the upward directional solidification of Al-Si ingots. He found that during the initial stages of solidification, when growth is constrained, tip velocity increases with time. Later on, when the growth becomes unconstrained, the tip velocity decreases with time. Therefore, the time evolution of the tip velocity will experience a maxima and this maximum coincides with the CET position.

To overcome the shortcomings of the mechanical blocking criterion, Martorano et al. (3) introduced the concept of *solutal-blocking*. The physical basis of this criterions is as follows: equiaxed grains can nucleate and grow in the constitutionally undercooled region ahead of the columnar front. These grains reject solute into the liquid surrounding the grains and enrich it. When the liquid ahead of the columnar front is highly enriched the local undercooling becomes zero; and, therefore, the columnar gets solutally blocked. To incorporate this concept into the mathematical model, the undercooling had to be defined relative to the average local liquid solute concentration, rather than the initial liquid concentration, as was done by Hunt. As a result of this new definition for undercooling, when the liquid concentration reaches the equilibrium concentration locally, the local undercooling ahead of the columnar front becomes zero and the columnar front stops: CET happens.

Martorano et al. (17) compared the solutal and mechanical blocking mechanisms. They found out that for small thermal gradients the solutal-blocking mechanism results in the same CET predictions as the mechanical-blocking mechanism. However, for intermediate values of thermal gradients, there is a significant difference between the predictions of two mechanisms: solutal blocking predicts earlier CET. The reason is that at the intermediate thermal gradients, the solutal interactions between the growing equiaxed grains and advancing columnar front are important and, when considered, will result in earlier CET.

Browne (19) proposed the *Peak Equiaxed Index Criterion* for CET. Equiaxed index is a measure of the total undercooling in the bulk liquid. At the start of solidification, its value is zero and increases with the size of the undercooled liquid region. At later times, when the size of the undercooled liquid region decreases to zero, the equiaxed index also decreases to zero. As a result of the initial increase and the subsequent decrease, the time evolution of the equiaxed index criterion will have a maxima. According to the peak equiaxed index criterion, CET happens when equiaxed index reaches its maxima.

Mcfadden et al. (20) compared constrained-to-unconstrained, critical cooling rate, and Peak equiaxed index CET criteria. Prediction of CET using these criteria does not require one to consider equiaxed nucleation; therefore, they are typically termed indirect CET criteria. The constrained-to-unconstrained and peak-equiaxed-index criteria predicted a CET position which agreed well with the experimental observations. However, the critical cooling rate criteria did not. Close to the CET position, the cooling rate at the columnar front reached a critical minimum value (as expected by the cooling rate criterion). However, the value of this minimum was different from the values previously reported by Peres et al. (21). The difference was because, in evaluating the cooling rate at the position of the columnar front, Peres et al. (21) did not take into account the columnar tip undercooling. It was recommended that, in predicting CET in simulations, if equiaxed nucleation is not taken into account, then the critical cooling rate criterion should not be used.

Ludwig and Wu (22) used their three-phase model (23), reviewed in the previous section, to predict CET using both solutal and mechanical mechanisms. They recommended that, especially in the presence of melt convection and grain sedimentation, accurate predictions of CET requires one to consider both mechanisms.

2.2.2 CET experiments

In this section we will review experimental studies of the CET. These experiments are introduced in two sections: 1) one earth experiments, i.e. CET in the existence of gravity, and 2) microgravity experiments.

2.2.2.1 On-earth CET experiments

On-earth CET experiments are reviewed in two sub-sections: 1) experiments without melt flow and 2) experiments with significant (buoyancy induced) melt flow.

2.2.2.1.1 Experiments without melt flow

Ares and Schvezov (24) studied the effect of cooling rate and alloy composition on the CET in upward directional solidification of Pb-Sn alloys. CET occurred when the columnar front temperature gradient dropped below 0.8 Kcm^{-1}. This value was estimated from the experimental cooling curves. It was observed that the CET does not take place in a sharp plane, but rather in a zone where and a fully columnar structure *gradually* transitions into a fully equiaxed structure and the columnar and equiaxed grains coexist. The thickness of this "coexisting" zone was about 1 cm. Ares et al. observed similar progressive CET mode in An-Al (25) and Al-Cu (26) alloys.

Mahapatra and Weinberg (27) studied CET during upward directional solidification of Sn-Pb alloys. A one dimensional model that does not account for the columnar tip undercooling was used to estimate the temperatures gradients in the casting. The boundary conditions for the model were extracted from the measured temperatures. It was found that CET happens when the columnar front temperature gradient reaches the critical value of 0.112 Kmm^{-1}.

Siqueira et al. (28, 29) conducted a similar experiment but with a higher heat extraction rate. The same procedure was used to calculate liquidus isotherm velocity and the temperature gradient at the position of liquidus isotherm. Their data did not support the CET criterion of Mahapatra and Weinberg (27). In fact, the columnar tip velocity and the temperature gradient at the location of CET were more than two times different from the values reported in Mahapatra and Weinberg (27). However, the tip cooling rate at the CET position agreed with the results of Mahapatra and Weinberg (27). Hence, they suggested that, a more realistic CET criterion should be based on the columnar front cooling rate rather than the temperature gradient ahead of the columnar front (as originally proposed by Mahapatra and Weinberg). The critical cooling rate, which was found to be independent of the solute content of the alloy or the imposed thermal conditions, was 0.01 Ks^{-}

[1] for Sn-Pb alloys and 0.2 Ks^{-1} for Al-Cu alloys. These critical cooling rates were specific to the alloy system but independent of the composition. However, one should note that, in both of these studies, the model that was used to estimate the thermal conditions at the columnar front did not take into account columnar tip undercooling. In other words, the temperature gradient and the isotherm velocity at the columnar front were assumed to be equal to the temperature gradient and the isotherm velocity at the liquidus respectively. Similar experiments were conducted by Peres et al. (21) with the Al-Si alloys with the Si content ranging between 3 to 9 wt. pct. The critical cooling rate for this system was found to be between 0.15 and 0.2 Ks^{-1}. In another study, the critical cooling rate for Al-Ni and Al-Sn systems was found to be 0.3 and 0.16 Ks^{-1} (30).

2.2.2.1.2 Experiments with melt flow

Spinelli et al. (31) performed experiments on the influence of melt convection on CET in downward directional solidification of Sn-Pb alloys. The observed that melt convection transports the dendrite fragments from the semi-solid mush into the bulk liquid. These fragments promote equiaxed nucleation and therefore, stimulate CET. The critical cooling rate for CET was found to be 0.03 Ks^{-1}.

Hachani et al. (32, 33) performed benchmark solidification experiments involving Sn-Pb with different cooling rates and nominal solute concentrations of 3, 6, and 10 wt. pct.. CET was observed for all solute concentrations. The size of the final equiaxed zone increased with the nominal solute concentration.

2.2.2.2 Microgravity experiments

Lie et al. (34) carried out directional solidification experiments under microgravity with both refined and non-refined Al-7 wt. pct. Si alloys. They examined different pulling velocities. When the pulling velocity was low, CET was observed to be progressive (i.e. the transition from a fully columnar structure to a fully equiaxed structure happened over a region). This is because, at low velocities, the constitutional undercooling ahead of the columnar front is low; therefore nucleation

will be slow. Slow nucleation will give old equiaxed grains enough time to elongate before they get blocked by new equiaxed grains. Elongated equiaxed grains will ultimately form a columnar-like zone in casting and CET will be progressive. On the other hand, at high pulling velocities, fast-repeated nucleation of new equiaxed grains will prevent the elongation of old equiaxed grains and, therefore, CET will be sharp.

In a later study, Lie et al. (35) simulated only the refined alloys in the above experiment and investigated two additional variables: (1) the thickness of the undercooled liquid region and (2) the maximum constitutional undercooling in this region. They found out that the thickness of the undercooled liquid region, rather than the maximum constitutional undercooling, is responsible for the different CET modes: sharp or progressive. A thick undercooled liquid region will promote the sharp CET mode. They also found out that there is a critical thermal gradient below which grain-elongation is controlled by thermal gradient and above which grain-elongation is controlled by the liquidus velocity.

Reinhart et al. (36) performed experiments and simulations of CET in the upward directional solidification of Al-3.5 wt. pct. Ni alloys. In the experiments, CET position was extracted (or measured) from X-ray radiographs showing the time evolution of the columnar front. In the simulations, CET was predicted by a 2D CAFÉ model, in the presence and absence of melt convection. CET predictions were in agreement with the experiments only when melt convection was considered.

2.3 Studies on macrosegregation

Solute composition inhomogeneities at the macro-scale (scale of whole casting) are termed *macrosegregation* (15). Macrosegregation forms when the micro-segregated melt adjacent to the solid is swept away by the relative motion between the solid and its adjacent liquid(37). This relative movement can be caused by: 1) solidification shrinkage, 2) natural or forced convection, 3) grain movement, and 4) deformation of the mushy zone, and 5) motion of gas bubbles that might develop during the solidification. The reader is referred to reference (15) for more information on how each of these mechanisms can cause macrosegregation.

Bellet et al. (38) proposed a numerical benchmark solidification problem with the objective of testing the different numerical algorithms and verifying different numerical codes. The benchmark uses a simple solidification model (infinite back diffusion in solid, fully columnar, no tip undercooling, and no solid motion) and the problem consists of Sn-Pb and Pb-Sn alloys solidifying in a rectangular cavity cooled from the side. In a later study, Combeau et al. (39) analyzed results from four different codes/contributors for this benchmark. The overall segregation patterns predicted by different codes was similar; however, in the regions where channels exist, predictions were noticeably different. One of the sources contributing to this difference was the discretization of the convection term in the liquid solute balance equation. It was conclude that, when channels form, it is unrealistic to seek a unique reference solution.

Combeau and co-workers have studied macro-segregation and channel segregates. For example, Kumar et al. studied the effects of various types of permeability relations on the predicted macro-segregation and channel segregates. The permeability predicted by these relations were different only in the near liquidus regions of the mush. The predicted channels were found to be very sensitive to the choice of the permeability relation. Only relations that permitted bulk liquid to penetrate into the near-liquidus regions of the mush predicted channels. In a later study, Kumar et al. (40) incorporated inertial effects into his model by adding a quadratic Forchheimer drag term to the liquid momentum equation and investigated the effects of inertia on macro-segregation. Adding the Forchheimer term hardly changed the global macro-segregation pattern; however, it slightly reduced the number of predicted channels. In another study, Kumar et al. (41) investigated the effect of numerical integration of the permeability term and the mesh size on the predicted macro-segregation and channel segregates. Predicted macro-segregation was not sensitive to the numerical treatment of the permeability term. Predicted channels, however, were sensitive to numerical treatment of the permeability term but only on the coarse mesh (1 mm). They also showed that, since channels can be as narrow as 1 mm, fully resolving them requires one to use mesh size as fine as 0.2 mm.

Felice et al. (42) presented a three-dimensional simulation of channel formation. At low dendrite arm spacing (i.e. low permeability), channels had a two-dimensional lamellar structure; however,

as arm spacing increases, channels become lamellar-tubular with some three-dimensional structures. As arm spacing increases even further, the structure becomes branched-tubular which is fully three-dimensional. Even when arm spacing is high enough, to result (or resulting) in a 3D branched-tubular structure, the initial growth of channels is still two-dimensional lamellar, and the structure *gradually* transitions to the final three-dimensional tubular structure.

Ludwig and Wu (43-45) used their two-phase columnar solidification model to study the formation of channel segregates. They showed that channel segregates form only in the regions where flow suppresses the local solidification rate. They termed these regions solidification-retarded zones and showed that: 1) re-melting is not necessary for channel formation (2) the predominant structure of channels is discontinuous lamellar. They hypothesized that, after a channel forms, the interaction between flow and solidification will determine if the channel can survive or not. These interactions are correlated with the $\boldsymbol{u} \cdot \nabla \overline{C}_l$ term in the liquid solute balance equation, which they name the flow-solidification interaction term. Channels can survive only in the regions where this term is negative. This is because, in these regions, an increase in flow velocity suppresses the local solidification rate, which promotes channel growth. Channel growth, in return, strengthens (or reinforces) flow, and hence, the flow-solidification interaction term decreases further below zero (instead of more negative). Thus, channels grow and become stable.

Chapter 3: A truncated-Scheil-type macroscale model for columnar solidification of binary alloys in the presence of melt convection

3.1 Abstract

A truncated-Scheil-type macroscale model is developed for columnar solidification of binary alloys in the presence of melt convection. The model assumes Scheil type solidification behind the primary tips and accounts for columnar dendrite tip undercooling. It is used to perform simulations of a numerical solidification benchmark problem. The predictions of the model in the absence and presence of melt convection are compared with the predictions of the Scheil model, which neglects undercooling entirely, and a three-phase model, which accounts for undercooling both behind and ahead of the primary tips. It is found that the truncated-Scheil-type and three phase models predict nearly identical results. This indicates that, for columnar solidification, the undercooling behind the primary tips can be disregarded and the model developed here can be used instead of the significantly more complex three-phase models. It was found that by increasing a parameter in the model, its predictions smoothly converge to the predictions of the Scheil model. The effect of undercooling on the melt convection during solidification, overall macrosegregation pattern, and the channel segregates is also investigated.

3.2 Introduction

Solidification on earth, where the gravity is present, typically occurs in the presence of melt convection. Melt convection is the main reason for defects such as macrosegregation, which is the solute composition inhomogeneities at the macro scale, and the only reason for the formation of a critical defect known as channel segregates, which are narrow pencil-like macrosegregation patterns that are highly enriched by various solute elements. These defects can be predicted only if melt convection is incorporated in models. Due to practical importance, incorporating melt convection in solidification models has been the subject of numerous studies in the past. The simplest models that account for melt convection are models that neglect undercooling and assume

lever/Scheil type solidification (which refer to solidification with infinite/zero solute back-diffusion from liquid to solid). These models consist of two phases only: a solid and a liquid phase. Having only two phases makes the numerical implementation of these models relatively simple and they have been, therefore, used extensively in the literature to predict macrosegregation and channel segregates. But, again, these relatively simple models neglect undercooling (15).

Accounting for undercooling in solidification models can be expected to be in general important because undercooling is crucial in determining the velocity of the columnar primary tips (15). In addition, complex phenomena such as columnar to equiaxed transition can be predicted only if undercooling is taken into account. In the literature, models that incorporate undercooling and melt convection are available. These model are typically based on the framework developed in the pioneering work of Wang and Beckermann (10). A model developed using this framework consist of three phases: a solid phase, an inter-dendritic liquid phase, and an extra-dendritic liquid phases. Existence of an additional liquid phase in the model makes the numerical implementation of these models significantly more complex than the models that do not account for undercooling and consist of only two phases. In addition, computational cost of these models are so high that mesh sensitive phenomena such as channel segregates are rarely fully resolved (46).

In this chapter, a two-phase model for columnar solidification is developed that incorporates melt convection and primary tip undercooling. This model is referred to as the truncated-Scheil-type model, instead of truncated-Scheil, because similar to the original truncated-Scheil model (47) it assumes Scheil type solidification behind the primary tips, but unlike that model it accounts for melt convection. Predictions of the model in the absence and presence of melt convection are compared with the Scheil model and a three-phase model that account for undercooling behind the primary tips. The effect of undercooling on the melt convection during solidification, overall macrosegregation pattern, and the channel segregates is investigated.

The rest of the chapter is organized as follows: the three-phase, truncated-Scheil-type, and Scheil-type models are introduced in section 3.3. In section 3.4, the numerical scheme that was developed to update the solid fractions in the simulations is discussed. In section 3.5, the solidification

numerical benchmark problem is introduced. Finally, in section 3.6, predictions of the models in the absence and presence of melt convection are discussed.

3.3 Mathematical models

In this section, a brief introduction of the three models that have been used in this study is first given. Then, the derivation of the equations of these models is discussed.

3.3.1 Three-phase model, truncated-Scheil-type model, and Scheil-type model

The first model in this chapter is a three-phase model that does not make any simplifying assumptions regarding the liquid undercooling. In other words, it accounts for liquid undercooling everywhere in the domain: both behind and ahead of the primary tips. This model is developed using the framework develop in the pioneering work of Wang and Beckermann (10). The reader is referred to that chapter for more details. This framework has been widely accepted in the literature. In brief, models based on this framework consist of three phases: solid, inter-dendritic liquid, and extra-dendritic liquid. The difference between the two liquid phases is that the inter-dendritic liquid is well-mixed and is at the equilibrium concentration while the extra-dendritic liquid is, in general, undercooled. Wang and Beckermann (2, 48, 49) used this framework to develop a model for equiaxed solidification in the presence of melt convection and a model for columnar and equiaxed solidification in the *absence* of melt convection (50). In this chapter, the framework of Wang and Beckermann (10) is used to develop a model for columnar solidification in the presence of melt convection. The main difference between this model and the model of Wang and Beckermann (2, 48, 49) is that the latter model was for equiaxed solidification only and therefore did not require tracking of the columnar front.

The second and third models in this chapter are truncated-Scheil-type and Scheil-type models that consist of a solid phase and only one liquid phase, as opposed to the three-phase model which consists of two liquid phases. These models assume that solidification inside the semi-sold mush takes place under equilibrium conditions: with zero liquid undercooling and with no solute back-diffusion from the liquid to solid. The only difference between these two models is that the

truncated-Scheil-type model accounts for liquid undercooling ahead of the primary tips while Scheil-type model neglects liquid undercooling entirely.

3.3.2 Equations for conservation of mass, momentum, energy, and solute in solid

The continuity equation in terms of the mixture velocity $\overline{\boldsymbol{v}}_m$, which, in the absence of solid motion, is equal to $g_l\overline{\boldsymbol{v}}_l$, reads (38)

$$\nabla\cdot\left(g_l\overline{\boldsymbol{v}}_l\right)=\nabla\cdot\overline{\boldsymbol{v}}_m=0 \tag{3-1}$$

The liquid momentum equation in terms of the liquid velocity reads (38)

$$\rho_0\frac{\partial}{\partial t}\left(g_l\overline{\boldsymbol{v}}_l\right)+\rho_0\nabla\cdot\left(g_l\overline{\boldsymbol{v}}_l\overline{\boldsymbol{v}}_l\right)=-g_l\nabla\overline{p}\ +\nabla\cdot\left[\mu_l\nabla\left(g_l\overline{\boldsymbol{v}}_l\right)\right]+g_l\tilde{\rho}_l\boldsymbol{g}-\frac{\mu_l g_l^{\,2}}{K}\overline{\boldsymbol{v}}_l \tag{3-2}$$

where ρ_0, g_l, $\overline{\boldsymbol{v}}_l$, $\overline{p}$, μ_l, $\tilde{\rho}_l$, and K are the reference density, liquid fraction, average liquid velocity, average pressure, liquid dynamic viscosity, liquid density in the buoyancy term, and the permeability of the semi-solid mush. The liquid density in the buoyancy term is calculated from $\tilde{\rho}_l=\rho_0\left[1-\beta_T\left(T-T_{ref}\right)-\beta_C\left(\overline{C}_l-C_{ref}\right)\right]$ (38), where β_T and β_C are the thermal and solutal expansion coefficients, respectively, and T_{ref} and C_{ref} are the reference temperature and solute concentration, respectively. The permeability of the semi-solid mush is calculated from the Kozeny-Carman relation: $K=\lambda_2^{\,2}g_l^{\,3}\Big/\left[180\left(1-g_l\right)^2\right]$ (38), where λ_2 is the secondary arm spacing.

It is common to re-write equation (3-2) in terms of the mixture velocity $\overline{\boldsymbol{v}}_m$. The first term on the left-hand side and the second and fourth terms on the right-hand side can be easily written in terms of $\overline{\boldsymbol{v}}_m$ using $\overline{\boldsymbol{v}}_m=g_l\overline{\boldsymbol{v}}_l$ (see the discussion above equation (3-1)). To re-write the second term in terms of $\overline{\boldsymbol{v}}_m$, one needs to first recognize that $\nabla\cdot\left(\overline{\boldsymbol{v}}_l\overline{\boldsymbol{v}}_m\right)=\left(\overline{\boldsymbol{v}}_l\cdot\nabla\right)\left(\overline{\boldsymbol{v}}_m\right)+\overline{\boldsymbol{v}}_l\left(\nabla\cdot\overline{\boldsymbol{v}}_m\right)=\left(1/g_l\right)\left(\overline{\boldsymbol{v}}_m\cdot\nabla\right)\overline{\boldsymbol{v}}_m$, where the first equality holds for any pair

of vectors $\overline{\boldsymbol{v}}_l$ and $\overline{\boldsymbol{v}}_m$, and the second equality follows simply from equation (3-1); the right-hand side of the second equality can be re-written as $\left(\overline{\boldsymbol{v}}_m \cdot \nabla\right)\overline{\boldsymbol{v}}_m = \left[\nabla\cdot\left(\overline{\boldsymbol{v}}_m\overline{\boldsymbol{v}}_m\right) - \overline{\boldsymbol{v}}_m\left(\nabla\cdot\overline{\boldsymbol{v}}_m\right)\right] = \nabla\cdot\left(\overline{\boldsymbol{v}}_m\overline{\boldsymbol{v}}_m\right)$. Combining these two relations one gets $\nabla\cdot\left(g_l\overline{\boldsymbol{v}}_l\overline{\boldsymbol{v}}_l\right) = \left(1/g_l\right)\nabla\cdot\left(\overline{\boldsymbol{v}}_m\overline{\boldsymbol{v}}_m\right)$ and substituting this into equation (3-2) gives the final momentum equation in terms of the mixture velocity $\overline{\boldsymbol{v}}_m$

$$\rho_0\frac{\partial\overline{\boldsymbol{v}}_m}{\partial t} + \rho_0\frac{1}{g_l}\nabla\cdot\left(\overline{\boldsymbol{v}}_m\overline{\boldsymbol{v}}_m\right) = -g_l\nabla\overline{p} + \nabla\cdot\left(\mu_l\nabla\overline{\boldsymbol{v}}_m\right) + g_l\tilde{\rho}_l\boldsymbol{g} - \frac{\mu_l g_l}{K}\overline{\boldsymbol{v}}_m \tag{3-3}$$

The energy equation reads (38)

$$\frac{\partial T}{\partial t} + \nabla\cdot\left(\overline{\boldsymbol{v}}_m T\right) = \alpha_0\nabla^2 T + \frac{h_{sl}}{c_p}\frac{\partial g_s}{\partial t} \tag{3-4}$$

where T, α_0, h_{sl}, c_p, and $g_s = 1 - g_l$ are the temperature, thermal diffusivity, latent heat, specific heat capacity, and solid fraction, respectively.

As discussed in section 3.3.1, the three models introduced in this chapter assume that there is no solute back-diffusion from the liquid to the solid and therefore the solute conservation equation in the solid is written as (38)

$$\frac{\partial}{\partial t}\left(g_s\overline{C}_s\right) = k_0 C_l^*\frac{\partial g_s}{\partial t} \tag{3-5}$$

3.3.3 Solute conservation in liquid(s)

The main difference between the three-phase, truncated-Scheil-type, and Scheil-type models is in the equation for the solute balance in liquid. The derivation of this equation for each of the models is discussed next.

3.3.3.1 Three-phase model

In the three-phase model, the solute conservation equation in the inter-dendritic liquid reads (2, 10, 48, 49)

$$\rho_0 \frac{\partial}{\partial t}\left(g_d \bar{C}_d\right) + \rho_0 \nabla \cdot \left(g_d \bar{\boldsymbol{v}}_l \bar{C}_d\right) = -k_0 \Gamma_{sd} \bar{C}_d - \Gamma_{ed} \bar{C}_d - \rho_0 \frac{S_{env} D_0}{\delta_{env}} \left(\bar{C}_d - \bar{C}_e\right) \tag{3-6}$$

where g_d, $\bar{C}_d$, Γ_{sd}, Γ_{ed}, S_{env}, δ_{env}, and $\bar{C}_e$ are the inter-dendritic liquid fraction, average solute concentration in the inter-dendritic liquid, the average interfacial mass generation source due to phase-change at the interface between the solid and inter-dendritic liquid and the interface between inter-dendritic liquid and extra-dendritic liquid, surface area of the envelope per unit volume of the REV, average diffusion length around the envelope. The solute conservation equations in the extra-dendritic liquid reads (2, 10, 48, 49)

$$\rho_0 \frac{\partial}{\partial t}\left(g_e \bar{C}_e\right) + \rho_0 \nabla \cdot \left(g_e \bar{\boldsymbol{v}}_l \bar{C}_e\right) = \Gamma_{ed} \bar{C}_d + \rho_0 \frac{S_{env} D_0}{\delta_{env}} \left(\bar{C}_d - \bar{C}_e\right) \tag{3-7}$$

where $g_e = 1 - g_s - g_d$ is the extra-dendritic liquid fraction.

Next, in equations (3-7) and (3-8), the convective fluxes on the left-hand side (i.e., $g_d \bar{\boldsymbol{v}}$ and $g_e \bar{\boldsymbol{v}}_l$) and the interfacial mass generation sources due to phase-change on the right-hand side (i.e., Γ_{sd} and Γ_{ed}) need to be rewritten in terms of the mixture velocity $\bar{\boldsymbol{v}}_m = g_l \bar{\boldsymbol{v}}_l$ and phase fractions, respectively. To substitute Γ_{sd} and Γ_{ed}, one first need to write the continuity equations for the solid and extra-dendritic liquids, which read (2, 10, 48, 49)

$$\rho_0 \frac{\partial g_s}{\partial t} = \Gamma_{sd} \tag{3-8}$$

$$\rho_0 \frac{\partial g_e}{\partial t} + \rho_0 \nabla \cdot \left(g_e \bar{\boldsymbol{v}}_l\right) = \Gamma_{ed} = -\rho_0 S_{env} w_{env} \tag{3-9}$$

and w_{env} is the average growth velocity of the envelope. Substituting Γ_{ed} from the first equality in equation (3-9) and noting that $\nabla\cdot\left(g_e\bar{\boldsymbol{v}}_l\bar{C}_e\right)=\nabla\cdot\left[\bar{\boldsymbol{v}}_m\left(g_e/g_l\right)\bar{C}_e\right]=\left(g_e/g_l\right)\nabla\cdot\left(\bar{\boldsymbol{v}}_m\bar{C}_e\right)+\bar{C}_e\nabla\cdot\left(\bar{\boldsymbol{v}}_m\, g_e/g_l\right)$ (where the first equality follows directly from the discussion above equation (3-1) and the second equality follows from the mathematical identity governing the divergence of a product of a scalar and a vector and equation (3-1)) equation (3-7) becomes

$$g_e\frac{\partial\bar{C}_e}{\partial t}+\frac{g_e}{g_l}\nabla\cdot\left(\bar{\boldsymbol{v}}_m\bar{C}_e\right)=\left(\bar{C}_d-\bar{C}_e\right)\frac{\partial g_e}{\partial t}+\left(\bar{C}_d-\bar{C}_e\right)\nabla\cdot\left(\bar{\boldsymbol{v}}_m\frac{g_e}{g_l}\right)+\frac{S_{env}D_0}{\delta_{env}}\left(\bar{C}_d-\bar{C}_e\right) \tag{3-10}$$

Similarly, Γ_{sd} and Γ_{ed} on the left-hand side of equation (3-6) can be substituted using equations (3-8) and (3-9), respectively, and the last term can be substituted from equation (3-10) to get

$$\begin{aligned}\frac{\partial}{\partial t}\left(g_d\bar{C}_d\right)+\nabla\cdot\left(g_d\bar{\boldsymbol{v}}_l\bar{C}_d\right)&=\left(1-k_0\right)\frac{\partial g_s}{\partial t}\bar{C}_d+\left[\frac{\partial g_d}{\partial t}+\nabla\cdot\left(g_d\bar{\boldsymbol{v}}_l\right)\right]\bar{C}_d\\&-\left[g_e\frac{\partial\bar{C}_e}{\partial t}+\frac{g_e}{g_l}\nabla\cdot\left(\bar{\boldsymbol{v}}_m\bar{C}_e\right)-\left(\bar{C}_d-\bar{C}_e\right)\frac{\partial g_e}{\partial t}-\left(\bar{C}_d-\bar{C}_e\right)\nabla\cdot\left(\bar{\boldsymbol{v}}_m\frac{g_e}{g_l}\right)\right]\end{aligned} \tag{3-11}$$

Now if the time and spatial derivatives on the left-hand-side are expanded, then the terms inside the second brackets on the right-hand-side can be dropped by their counterparts on the left-hand side and the result will be

$$\begin{aligned}g_d\frac{\partial\bar{C}_d}{\partial t}+g_d\bar{\boldsymbol{v}}_l\cdot\nabla\bar{C}_d&=\left(1-k_0\right)\frac{\partial g_s}{\partial t}\bar{C}_d\\&-\left[g_e\frac{\partial\bar{C}_e}{\partial t}+\frac{g_e}{g_l}\nabla\cdot\left(\bar{\boldsymbol{v}}_m\bar{C}_e\right)-\left(\bar{C}_d-\bar{C}_e\right)\frac{\partial g_e}{\partial t}-\left(\bar{C}_d-\bar{C}_e\right)\nabla\cdot\left(\bar{\boldsymbol{v}}_m\frac{g_e}{g_l}\right)\right]\end{aligned} \tag{3-12}$$

Next, equation (3-12) needs to be re-written in the conservative form, where the inner product on the left-hand side is substituted by a divergence, and in terms of the mixture velocity $\bar{\boldsymbol{v}}_m$ only. Using $\left(\bar{C}_d-\bar{C}_e\right)\nabla\cdot\left(\bar{\boldsymbol{v}}_m\, g_e/g_l\right)=\nabla\cdot\left[\bar{\boldsymbol{v}}_m\left(g_e/g_l\right)\left(\bar{C}_d-\bar{C}_e\right)\right]-\bar{\boldsymbol{v}}_m\left(g_e/g_l\right)\cdot\nabla\left(\bar{C}_d-\bar{C}_e\right)$ and

$g_d \bar{\boldsymbol{v}}_l \cdot \nabla \bar{C}_d = (g_l - g_e)(\bar{\boldsymbol{v}}_m / g_l) \cdot \nabla \bar{C}_d = \nabla \cdot (\bar{\boldsymbol{v}}_m \bar{C}_d) - (g_e / g_l) \nabla \cdot (\bar{\boldsymbol{v}}_m \bar{C}_d)$, equation (3-12) becomes

$$g_l \frac{\partial \bar{C}_d}{\partial t} + \nabla \cdot (\bar{\boldsymbol{v}}_m \bar{C}_d) = (1 - k_0) \bar{C}_d \frac{\partial g_s}{\partial t} - \frac{\partial}{\partial t}\left[g_e (\bar{C}_e - \bar{C}_d) \right] - \nabla \cdot \left[\bar{\boldsymbol{v}}_m \frac{g_e}{g_l} (\bar{C}_e - \bar{C}_d) \right] \tag{3-13}$$

Next, equations for the solute balance in the inter-dendritic and extra-dendritic liquids (i.e., equations (3-6) and (3-7)) are used to derive the equation for the solute balance in the liquid for the truncated-Scheil-type and Scheil-type model.

3.3.3.2 Truncated-Scheil-type and Scheil-type models

As already discussed in sub-section 3.3.1, the truncated-Scheil-type model has only one liquid phase and the equation for solute conservation in this phase needs to be written in terms of the average solute concentration in liquid $\bar{C}_l$, which is defined as

$$g_l \bar{C}_l = g_d \bar{C}_d + g_e \bar{C}_e \tag{3-14}$$

The equation for $\bar{C}_l$ is obtained by adding-up equations (3-7) and (3-6), substituting $g_d \bar{C}_d + g_e \bar{C}_e$ from equation (3-14), $g_l \bar{\boldsymbol{v}}_l$ from the first equality in equation (3-1), Γ_{sd} from equation (3-8), and using $\bar{C}_d \, \partial g_s / \partial t = C_l^* \, \partial g_s / \partial t$ as

$$\rho_0 \frac{\partial}{\partial t}(g_l \bar{C}_l) + \rho_0 \nabla \cdot (\bar{\boldsymbol{v}}_m \bar{C}_l) = -k_0 C_l^* \frac{\partial g_s}{\partial t} \tag{3-15}$$

Expanding the time derivative on the left-hand side and adding and subtracting $k_0 \bar{C}_l \, \partial g_l / \partial t$ to and from the right-hand side gives

$$g_l \frac{\partial \bar{C}_l}{\partial t} + \nabla \cdot (\bar{\boldsymbol{v}}_m \bar{C}_l) = k_0 (C_l^* - \bar{C}_l) \frac{\partial g_l}{\partial t} + \bar{C}_l (1 - k_0) \frac{\partial g_s}{\partial t} \tag{3-16}$$

The truncated-Scheil-type and Scheil-type models assume that in the presence of solidification (i.e., behind the columnar front or the edge of the semi-solid mush), the liquid is not undercooled: $C_l^* = \overline{C}_l$; therefore, the first term on the right-hand-side is zero. In the absence of solidification, this term is again zero (because $\partial g_l / \partial t = 0$). Therefore, equation (3-16) becomes

$$g_l \frac{\partial \overline{C}_l}{\partial t} + \nabla \cdot \left(\overline{\boldsymbol{v}}_m \overline{C}_l \right) = \overline{C}_l \left(1 - k_0 \right) \frac{\partial g_s}{\partial t} \tag{3-17}$$

3.3.4 Phase-diagram relations for the three-phase, truncated-Scheil-type and Scheil-type models

In this section, the phase-diagram relations for the three-phase, truncated-Scheil-type and Scheil-type models are introduced. These relations are first written down for the three-phase model and then it is discussed how they should be modified for the truncated-Scheil-type and Scheil-type models. For the three-phase model, under the assumption that the interface between the inter-dendritic and extra-dendritic liquids is at the equilibrium concentration given by the phase diagram C_l^*, and the assumption that the inter-dendritic liquid is well-mixed, one has $\overline{C}_d = C_l^*$ during solidification. In addition, during the eutectic reaction, the temperature is equal to the eutectic temperature T_{eut} and there is no solute rejection: the partition coefficient is equal to unity:

$$\begin{aligned} &\text{Primary solidification}: \; T \le T_{liq}\left(\overline{C}_e\right) \text{ and } \phi > 0 \quad \rightarrow \quad \overline{C}_d = C_l^* = \frac{T - T_f}{m_l} \\ &\text{Eutectic solidification}: \; \overline{C}_d = C_{eut} \text{ and } g_l \ge 0 \quad \rightarrow \quad T = T_{eut} \quad \text{and} \quad k_0 = 1 \end{aligned} \tag{3-18}$$

where $T_{liq}\left(\overline{C}_d\right) = T_f + m_l \overline{C}_d$ is the liquidus temperature corresponding to the local inter-dendritic liquid concentration $\overline{C}_d$, and ϕ is a continuous indicator field, known as phase-filed, that distinguishes the semi-solid mushy region behind the columnar front (which is a smooth imaginary surface that connects the columnar primary tips), which has $\phi > 0$, from the (undercooled or superheated) liquid region ahead of the columnar front, which has $\phi < 0$. The columnar front itself corresponds to iso-contour $\phi = 0$.

To obtain the phase-diagram relations for the truncated-Scheil-type and Scheil-type models, equation (3-18) needs to be modified. For the truncated-Scheil-type model, $\overline{C}_d$ in this equation needs to be replaced with $\overline{C}_l$; for the Scheil model, in addition to replacing $\overline{C}_d$ with $\overline{C}_l$, the condition $\phi > 0$ needs to be removed.

3.3.5 Other constitutive relations for the three-phase model

In this section, the relations to calculate the average envelope surface area per unit volume of the REV, S_{env}, and the diffusion length around the envelopes δ_{env}, appearing in equation (3-10), are listed. The relation to calculate S_{env} reads (3)

$$S_{env} = \begin{cases} 0 & \phi < 0 \\ \dfrac{3\left(1-g_e\right)^{2/3}}{R_f} & \phi \geq 0 \end{cases} \tag{3-19}$$

where $R_f = \lambda_1/2$ is the final grain radius and λ_1 is the primary arm spacing. The diffusion length δ_{env} is calculated from (3)

$$\frac{\delta_{env}}{R_e} = \frac{3R_e e^{Pe}}{R_f^3 - R_e^3} \int_{R_e}^{R_f} \left(\int_{R_e}^{r} \frac{e^{-Pe\frac{r'}{R_e}}}{r'^2} dr' \right) r^2 dr \tag{3-20}$$

where $Pe = w_{env} R_e / D_l$ is the growth Péclet number and $R_e = R_f\left(1-g_e\right)^{1/3}$ is the instantaneous sphere radius.

3.3.6 Columnar front tracking for the three-phase and truncated-Scheil-type models

As discussed in the subsections 3.3.4 and 3.3.5, in the three-phase and truncated-Scheil-type models (and not in the Scheil-type model), a phase-field ϕ appears in the phase-diagram relations.

In addition, in the three-phase model, ϕ appears in the equation for the envelope surface area (i.e., equation (3-19)). The phase-field ϕ is calculated using the sharp interface tracking method of Sun and Beckermann (51)

$$\frac{\partial \phi}{\partial t} + \nabla \cdot \left(\boldsymbol{w}_{env} \phi \right) - \phi \nabla \cdot \boldsymbol{w}_{env} = b \left[\nabla^2 \phi + \frac{\phi \left(1 - \phi^2 \right)}{W^2} - \left| \nabla \phi \right| \nabla \cdot \left(\frac{\nabla \phi}{\left| \nabla \phi \right|} \right) \right] \tag{3-21}$$

where $\boldsymbol{w}_{env}$ is the envelope growth velocity vector and the parameters b and W are numerical parameters that control the stability of the method and the thickness of the interface, respectively. This parameters need to be chosen following the guidelines discussed in Sun and Beckermann (51). To calculate $\boldsymbol{w}_{env}$, it is assumed that the envelope growth is perpendicular to the local isotherms and $\boldsymbol{w}_{env}$ is therefore calculated from

$$\boldsymbol{w}_{env} = w_{env} \frac{\nabla T}{\left| \nabla T \right|} \tag{3-22}$$

In the three-phase model, the average growth velocity of the envelope is calculated from (3, 10)

$$w_{env} = \frac{4 \sigma^* D_0 m_l \left(k_0 - 1 \right) C_l^*}{\Gamma} \left[Iv^{-1} \left(\Omega_e \right) \right]^2 \tag{3-23}$$

where $\sigma^* = 0.02$, Γ, $Iv^{-1}(\ )$, and Ω_e are the tip selection parameter, Gibbs-Thomson coefficient, inverse Ivantsov function and the averaged undercooling in the extra-dendritic liquid, which is defined as (3)

$$\Omega_e = \frac{C_l^* - \bar{C}_e}{C_l^* \left(1 - k_0 \right)} \tag{3-24}$$

In equation (3-23), the inverse Ivantsov function is calculated from (3)

$$Iv^{-1}\left(\Omega_e\right)=0.4567\left(\frac{\Omega_e}{1-\Omega_e}\right)^{1.195} \tag{3-25}$$

In the truncated-Scheil-type model, the average envelope velocity is calculated from equations similar to equations (3-23) to (3-25), except that, instead of the average undercooling in the extra-dendritic liquid Ω_e, average undercooling in liquid Ω_l, which is defined as

$$\Omega_l=\frac{C_l^*-\bar{C}_l}{C_l^*\left(1-k_0\right)} \tag{3-26}$$

is used. It is emphasized again that the Scheil-type model doesn't required interface tracking. For this model, an "undercooling" can be calculated from equation (3-26), but the values of Ω_l are then expected to be zero inside the mush and negative in the superheated liquid. This is because inside the mush one has $C_l^*=\bar{C}_l$ and therefore $\Omega_l=0$. Outside the mush (i.e., for the superheated liquid, which has $T>T_{liq}\left(\bar{C}_l\right)=T_f+m_l\bar{C}_l$) one has $C_l^*<\bar{C}_l$ (note that $m_l<0$) and therefore $\Omega_l<0$.

3.4 Solid fraction updating scheme

Note that none of the three-phase, truncated-Scheil-type, or Scheil models have an explicit relation for the solid fraction. In other words, there is no relation to calculate the solidification fraction directly from. An equation to calculate the solid fraction can be derived by first acknowledging that the equalities on the right-hand side of the arrows in equation (3-18) will be satisfied only if the "correct" solid fraction is used in calculating the temperature and solute concentration. If, with the current value of the solid fraction, this equation is not satisfied then the solid fraction needs to be corrected by an amount that can be assumed to be proportional to the imbalance between the two sides of the equalities. For the three-phase model, this can be written as

$$\begin{aligned}&\text{Primary solidification:}\quad g_s^{n+1}=g_s^n+\frac{\partial g_s}{\partial T}m_l\left(C_l^*-\bar{C}_d\right)\\&\text{Eutectic solidification:}\quad g_s^{n+1}=g_s^n+\frac{\partial g_s}{\partial T}\left(T_{eut}-T\right)\end{aligned} \tag{3-27}$$

where the superscripts n and $n+1$ refer to the current and previous iteration levels, respectively. Note that at each time step in the numerical simulations updating the solid fraction using this equation should be continued until $g_s^{n+1} = g_s^n$ (within the numerical precision). For the truncated-Scheil-type and Scheil-type models, $\bar{C}_d$ in the first equality in equation (3-27) needs replaced with $\bar{C}_l$. Next relations to calculate $\partial g_s / \partial T$ during the primary and eutectic solidification need to be derived.

To obtain a relation to calculate $\partial g_s / \partial T$ during the primary solidification, equation is first discretized explicitly as

$$g_l^{old}\frac{\bar{C}_d - \bar{C}_d^{old}}{\Delta t} + \nabla\cdot\left(\bar{\boldsymbol{v}}_m \bar{C}_d\right)^{old} = \left(1-k_0\right)\bar{C}_d\frac{g_s^n - g_s^{old}}{\Delta t} - \frac{\partial}{\partial t}\left[g_e\left(\bar{C}_e - \bar{C}_d\right)\right]^{old} - \nabla\cdot\left[\bar{\boldsymbol{v}}_m\frac{g_e}{g_l}\left(\bar{C}_e - \bar{C}_d\right)\right]^{old} \tag{3-28}$$

Substituting $g_l^{old} = 1 - g_s^{old}$ and $\bar{C}_d = \left(T - T_f\right)/m_l$ into equation (3-28) gives

$$\left(1-g_s^{old}\right)\frac{\left(T-T_f\right)/m_l - \bar{C}_d^{old}}{\Delta t} + \nabla\cdot\left(\bar{\boldsymbol{v}}_m \bar{C}_d\right)^{old} = \left(1-k_0\right)\frac{T-T_f}{m_l}\frac{g_s^n - g_s^{old}}{\Delta t} - \frac{\partial}{\partial t}\left[g_e\left(\bar{C}_e - \bar{C}_d\right)\right]^{old} - \nabla\cdot\left[\bar{\boldsymbol{v}}_m\frac{g_e}{g_l}\left(\bar{C}_e - \bar{C}_d\right)\right]^{old} \tag{3-29}$$

Both sides of this equation are now differentiated with respect to T, which gives

$$\left(1-g_s^{old}\right) = \left(1-k_0\right)\left(g_s^n - g_s^{old}\right) + \left(1-k_0\right)\left(T-T_f\right)\frac{\partial g_s}{\partial T} \tag{3-30}$$

This equation is rearranged to give

$$\frac{\partial g_s}{\partial T} = \frac{1 - g_s^n + k_0\left(g_s^n - g_s^{old}\right)}{\left(1-k_0\right)\left(T - T_f\right)} \tag{3-31}$$

To obtain a relation to calculate $\partial g_s / \partial T$ during the eutectic solidification, equation (3-4) is first discretized explicitly as

$$\frac{T - T^{old}}{\Delta t} + \nabla \cdot \left(\overline{\boldsymbol{v}}_m T\right)^{old} = \alpha \nabla^2 T^{old} + \frac{h_{sl}}{c_p}\frac{g_s - g_s^{old}}{\Delta t} \tag{3-32}$$

Differentiating both sides of this equation with respect to g_s gives

$$\frac{\partial g_s}{\partial T} = \frac{c_l}{h_{sl}} \tag{3-33}$$

Combining equations (3-31) and (3-34) one gets:

$$\begin{aligned} &\text{Primary solidification:} \quad \frac{\partial g_s}{\partial T} = \frac{1 - g_s^n + k_0\left(g_s^n - g_s^{old}\right)}{\left(1-k_0\right)\left(T - T_f\right)} \\ &\text{Eutectic solidification:} \quad \frac{\partial g_s}{\partial T} = \frac{c_l}{h_{sl}} \end{aligned} \tag{3-34}$$

An in-house parallel computing code was developed on the OpenFOAM platform. OpenFOAM is an open source C++ library for the solution of the continuum mechanics problems (52, 53). The details of the numerical implementation of the equations are not discussed here and an interested reader should contact the author for more numerical details.

3.5 Problem statement

The problem studied in this chapter is the solidification numerical benchmark problem introduced in Bellet et al. (38). A schematic of the problem is shown in Figure 3-1. It consists of solidification of lead-18 wt. pct. tin alloy in a rectangular cavity that is insulated from the top and bottom and is cooling from the sides through an external cooling fluid with ambient temperature T_∞ and an overall heat transfer coefficient h_T. The width and height of the cavity are 0.1 and 0.06 cm, respectively. Due to the symmetry along the vertical mid-plane, only half of the cavity needs to be simulated. Initially, the melt is stationary and its temperature is uniform and equal to the liquidus temperature at the initial concentration $C_{ref} = 18$ wt. pct.

The thermophysical and phase diagram properties were taken from Bellet et al. (38). In addition, the liquid mass diffusivity D_l and the Gibbs-Thomson coefficient Γ, which are required in simulating the three-phase and truncated Scheil models, are $D_l = 7\times10^{-9} m^2 s^{-1}$ and $\Gamma = 7.9\times10^{-8} mK$ (54, 55). Finally, the primary arm spacing was calculated using $\lambda_1 = 2\lambda_2$ (56, 57).

3.6 Results and discussion

3.6.1 Results in the absence of melt convection

In Figure 3-2, a comparison between the predictions of the Scheil, truncated-Scheil and three-phase models in the absence of melt convection is shown. The predictions of the Scheil, truncated-Scheil and full models are shown as back, red, and blue curves, respectively. Plot (a) shows the comparison between the solid fraction profiles at t = 60 s, and plot (b) shows the comparison between the liquid undercoolings at that time. The vertical dashed lines show the position of the columnar front predicted by the different models. For the truncated-Scheil and three-phase models, as already discussed, the columnar front corresponds to the isoline $\phi = 0$ and in the Scheil model it corresponds to the isoline $g_s = 0.01$. The choice of 0.01 instead of another small value, 0.001 for example, is arbitrary, but should not distract because it has no influence on the results nor the following discussion. From plot (a) it can be seen that the columnar front position and the solid fractions predicted by the truncated-Scheil and full models are essentially equal. Behind the

columnar fronts, these solid fractions agree very well with the solid fractions predicted by the Scheil model. From plot (b) it can be seen that the undercooling predicted by the Scheil model is, as expected, zero, while the undercoolings predicted by the truncated-Scheil and three-phase models are zero behind the columnar front, have their maximum value (about 0.15) at the columnar front and decrease to zero as one moves away from the columnar front towards the liquid.

In Figure 3-3, the solid fractions and liquid undercoolings predicted by the truncated-Scheil model (shown in plots (a) and (b), respectively) with different values of the tip selection parameter σ^* are compared with the corresponding predictions of the Scheil model. The vertical lines show the position of the columnar front. It can be seen from the plots that as σ^* in the truncated model is increased, the length of the undercooled liquid region and the value of undercooling in this region decrease; the front position predicted by this model get closer and closer the front position predicted by the Scheil model and with $\sigma^* = 200$, the front position predicted by the two models nearly collapse.

3.6.2 Results in the presence of melt convection

Predictions of the three-phase, truncated-Scheil-type, and Scheil-type models in the presence of melt convection are shown in Figure 3-4 to Figure 3-6. Figure 3-4 shows the results at an early solidification time (i.e., t = 10 s) and Figure 3-5 and Figure 3-6 show the results at two intermediate solidification times (i.e., t = 60 and 120 s, respectively). With all the models, the total solidification time was about 550 s. Predictions of the three-phase and truncated-Scheil models are shown for $\sigma^* = 0.02$ and $\sigma^* = 200$. The contour plots of the temperature, solid fraction, liquid/extra-dendritic liquid undercooling, liquid density, and mixture concertation are shown in the first through fifth columns, respectively. In the solid fraction contour plots, the vectors and the white curves represent the mixture velocity and the columnar front, respectively. From these plots it can be seen that the predictions of the different models and for the different values of σ^* are overall very similar. The only noticeable differences are the predicted flow pattern in the bulk liquid ahead of the front (see the vectors in contour plots of the second column) and the predicted depth and number of channel segregates. When undercooling is not taken into account (i.e., the Scheil-type

model and the three-phase and truncated-Scheil-type models with $\sigma^* = 200$) the melt flow is strongest inside the mush. When the undercooling is taken into account, however, there is no significant melt flow inside the mush (except in the channels region) and the melt flow is mainly in the bulk liquid ahead of the front. The reason for the difference in the flow pattern is discussed next.

The main reason for the difference in the flow patterns in the absence and presence of tip undercooling is the difference in the magnitude of the solid fractions behind the columnar front. From the plots it can be seen that when undercooling is not taken into account (i.e., the Scheil model and the three-phase and truncated-Scheil-type models with $\sigma^* = 200$) , the solid fractions immediately behind the front are, as expected (see the results in the absence of melt convection show in Figure 3-2), relatively low (less than 0.05), while when the undercooling is taken into account, they have intermediate values (about 0.3). Low solid fractions behind the columnar front permit relatively strong local melt flow. This strong flow requires feeding by the flow in the bulk melt. Because the flow inside the mush is upwards, the feeding melt flow needs to be downwards counter-clock wise. When the solid fraction behind the columnar front is high, the flow inside the mush will be much weaker and, therefore, will not require significant feeding from the bulk melt. Therefore, the direction of flow in the bulk liquid ahead of the front is determined by the downward thermal buoyancy forces.

From the solid fraction contour plots shown in figures (4-6) it can also be seen that at t = 60 s few channel segregates have fully established. Channel segregates have been the subject of extensive studies in the past (15). They are initiated by convective instabilities in the high liquid fraction regions of the semi-solid mush. Most of the metallic alloys, including the lead-tin alloy considered in this chapter, have a partition coefficient less than unity; therefore, during their solidification, the solute will be rejected into the melt. The solute rejection changes the density of the melt and induces buoyancy forces. To understand how channels form, imagine a parcel of highly segregated liquid located deep in the mush. Two type of forces act on the parcel: buoyancy forces and frictional forces. Under certain conditions, the buoyancy forces will be strong enough to overcome the frictional retarding forces (excreted to the parcel by the semi-solid mush) and move the parcel towards upper regions of the mush (near the primary columnar dendrite tips). The parcel will retain

its composition as it flows to the upper regions of the mush (since the mass diffusivity of the parcel is much lower than its heat diffusivity) where the temperature is higher. In these regions, this still highly-segregated, displaced parcel will delay solidification (or even locally re-melt the solid) which will increase the local permeability of the mush. The local increase in the permeability allows the subsequent parcels to flow more easily. This, in turn, delays solidification (or enhances re-melting) even further until open channels form that are completely free of solid.

In Figure 3-7, the final macrosegregation patterns (i.e., the final distribution of the mixture concentration C, which is equal to $g_s\overline{C}_s + g_d\overline{C}_d + g_e\overline{C}_e$ in the three-phase model and $g_s\overline{C}_s + g_l\overline{C}_l$ in the truncated-Scheil-type and Scheil-type models) predicted by the three models are shown. Again, results for the three-phase and truncated-Scheil-type models are shown for two different values of $\sigma^* = 0.02$ and 200. From the plots it can be seen that accounting for undercooling does not change the overall macrosegregation pattern. This pattern consists of a region with negative segregation (i.e., $C < C_0$) at the bottom of the cavity. This is because solute rejected during solidification at this part of the cavity is carried away by the local melt convection. This negative segregation region forms at the expense of positively segregated regions at the top near the symmetry line and in the middle so that the global species balance is maintained.

3.7 Conclusions

A truncated-Scheil-type two-phase model was developed for columnar solidification of binary alloys in the presence of melt convection. The model accounts for primary dendrite tip undercooling and assumes Scheil-type solidification behind the primary tips. The model was used to perform simulations of a numerical solidification benchmark problem. Predictions of the model were compared with the predictions of the Scheil-type, which neglects undercooling entirely, and a three-phase model, which accounts for undercooling both ahead and behind the columnar primary tips. It was shown that predictions of the truncated-Scheil-type model and the three-phase models are nearly identical, which indicates that the truncated-Scheil-type model introduced in this chapter can be used instead of the significantly more complex three-phase model to account for columnar dendrite tip undercooling.

It is also found that the dendrite tip selection parameter σ^* is a key parameter in the truncated Scheil-type and three-phase models. With the real value of σ^* (i.e., $\sigma^* = 0.02$) these models account for undercooling; as the value of σ^* is increased in the simulations the predicted undercooling vanishes and the predictions of these models converge to the predictions of the Scheil model. It is also found that accounting for undercooling has no significant impact on the predicted final overall macrosegregation pattern. It only influences the flow pattern in the bulk liquid ahead of the primary tips during solidification and also the depth and number of the predicted channel segregates.

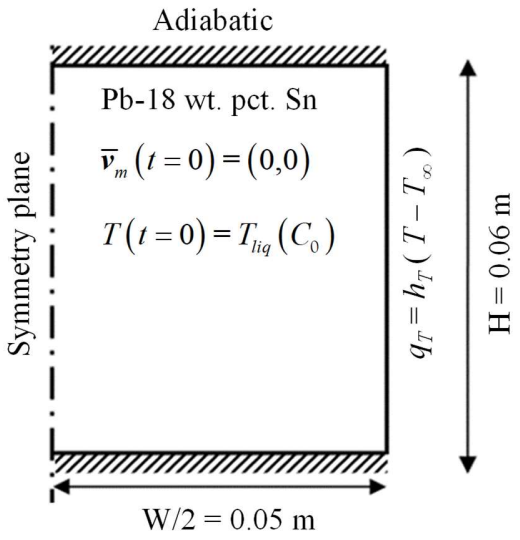

Figure 3-1. Schematic of the solidification numerical benchmark problem.

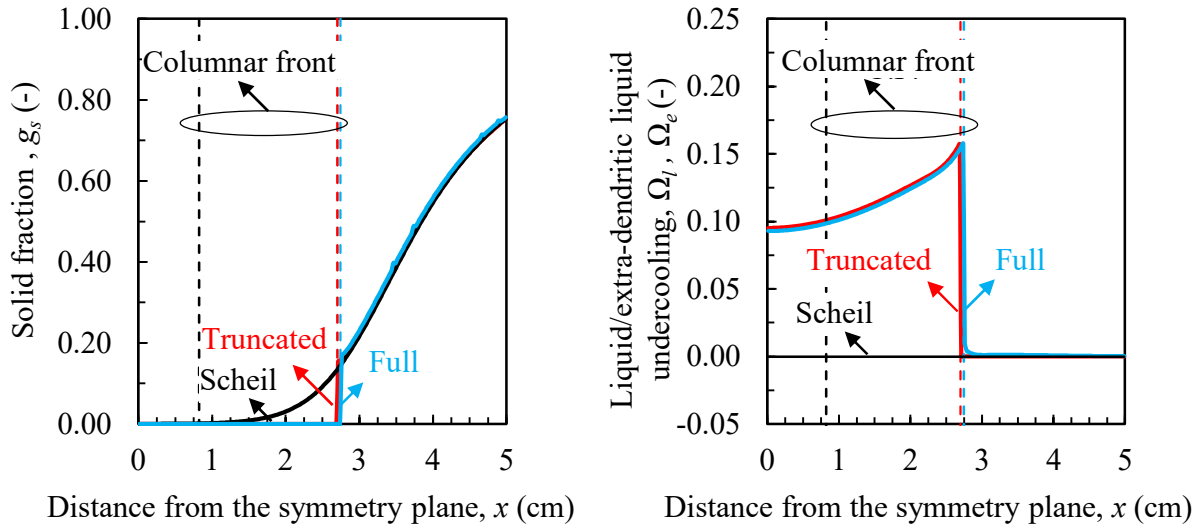

(a) (b)

Figure 3-2. Comparison between the predictions of the truncated-Scheil-type, three-phase and Scheil models in the absence of melt convection. Profiles of the (a) solid fraction and (b) liquid/extra-dendritic liquid undercooling at t = 60 s.

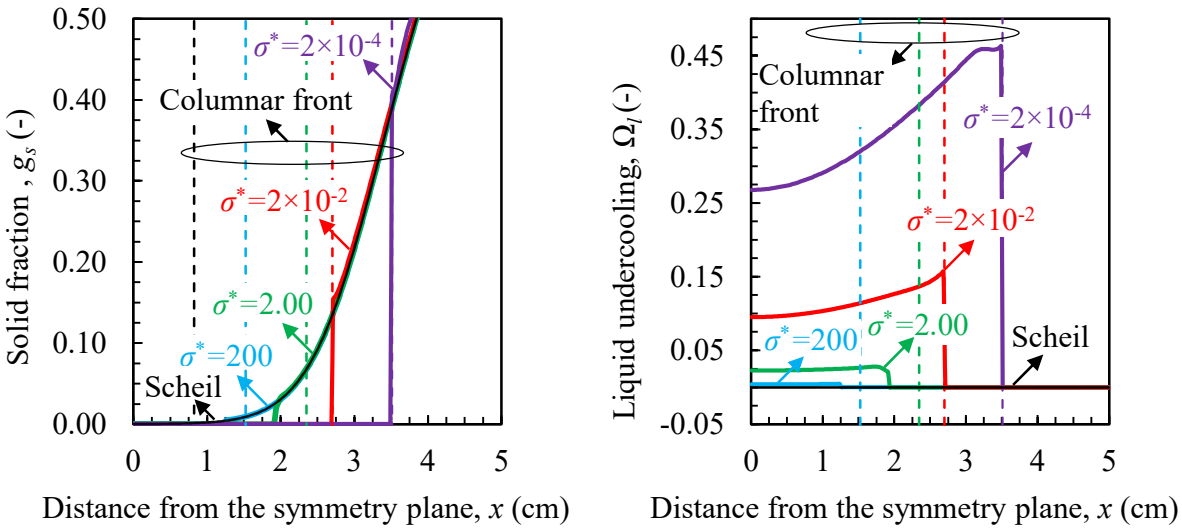

(a) (b)

Figure 3-3. Convergence of the predictions of the truncated-Scheil-type model to the Scheil model as the liquid undercooling vanishes with increase in the value of the tip selection parameter σ^*. The solid fraction (a) and liquid undercooling (b) profiles at t = 60 s.

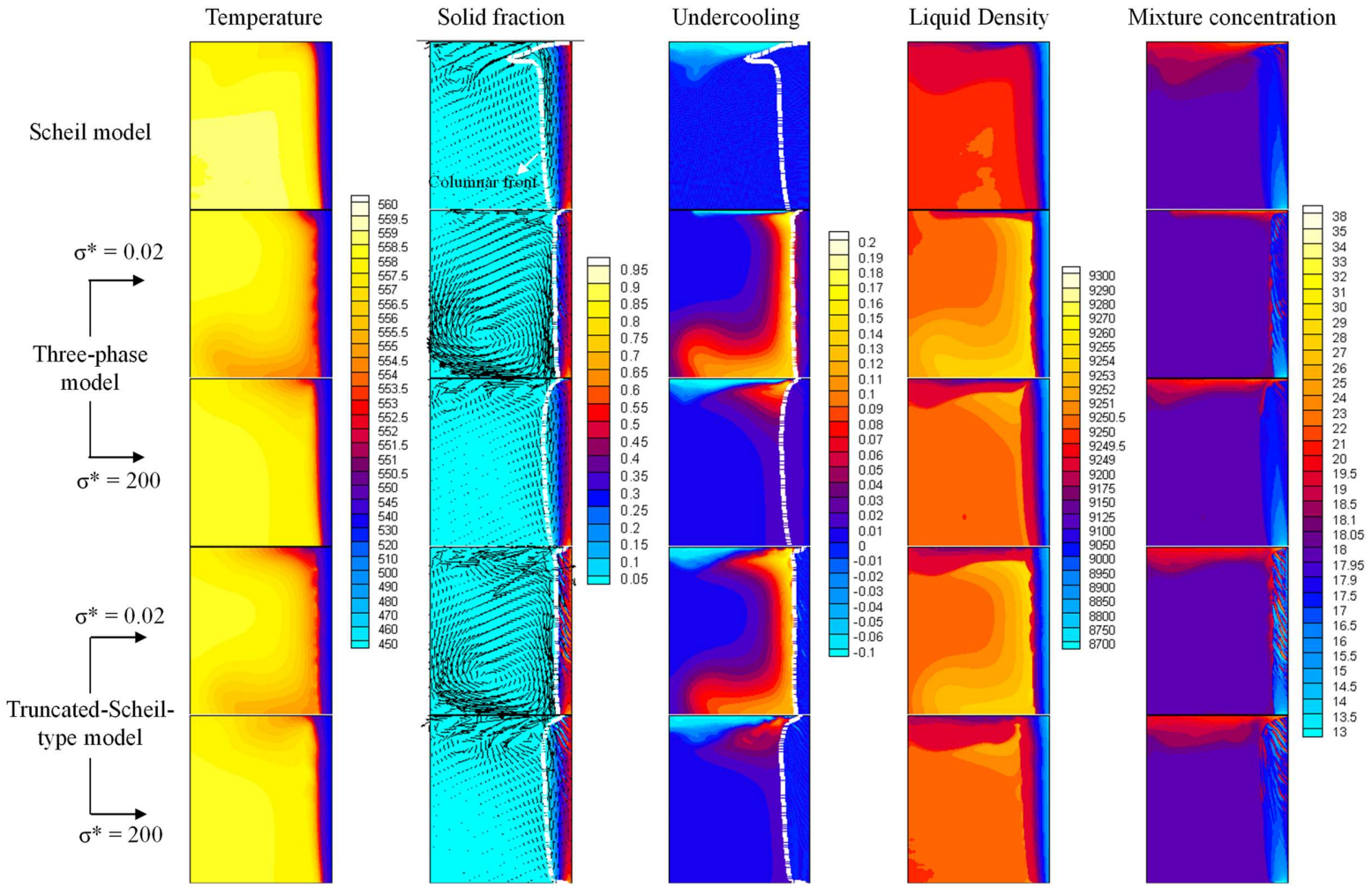

Figure 3-4. Snapshots at $t = 10$ s of the different quantities predicted by the Scheil, three-phase, and truncated-Scheil-type models. In the second and third columns, the vectors represent the mixture velocity and the white curve represents the columnar front, which corresponds to isoline $g_s = 0.01$ or $\phi = 0$.

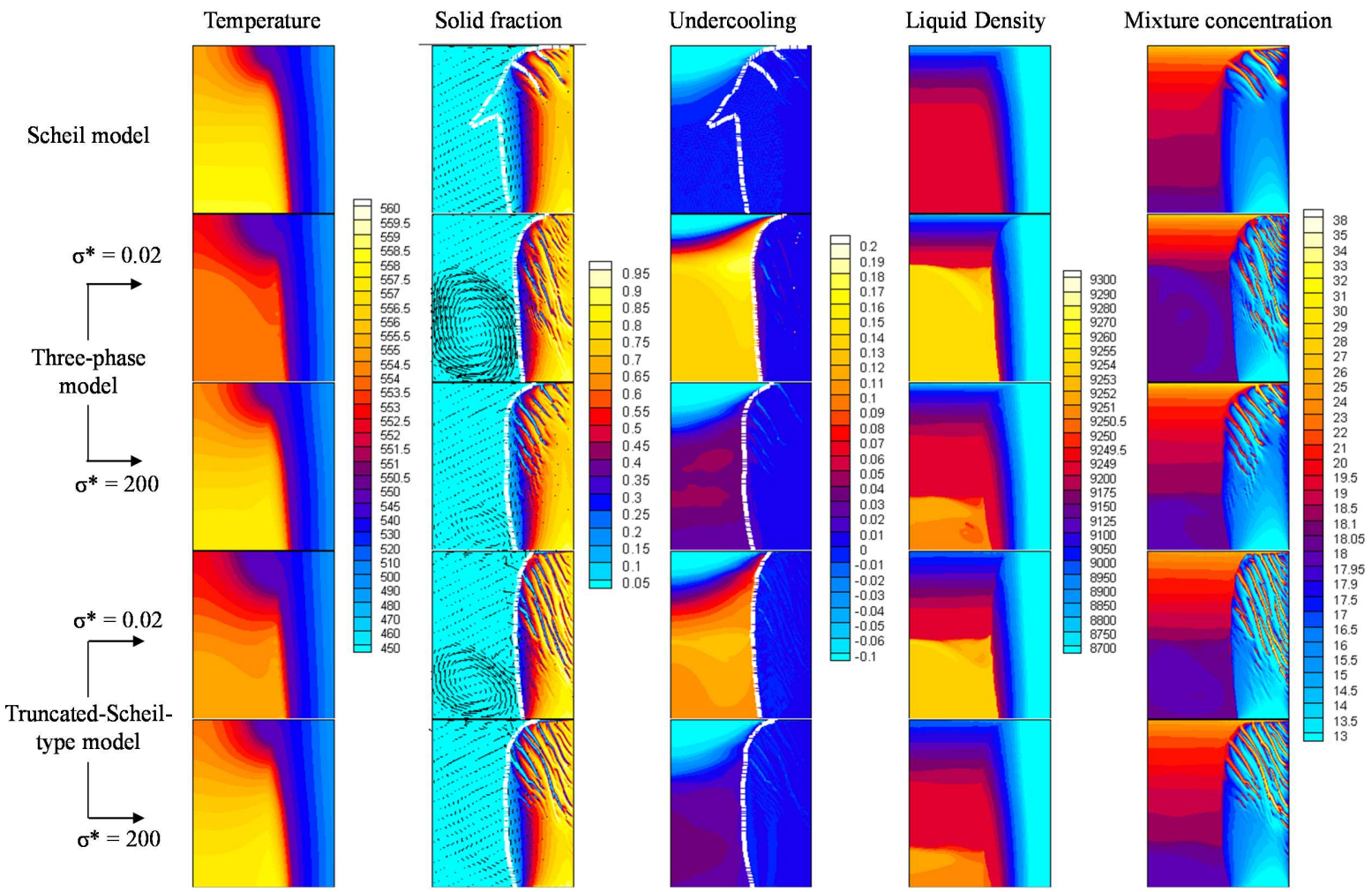

Figure 3-5. Snapshots at $t = 60$ s of the different quantities predicted by the Scheil, three-phase, and truncated-Scheil-type models. In the second and third columns, the vectors represent the mixture velocity and the white curve represents the columnar front, which corresponds to isoline $g_s = 0.01$ or $\phi = 0$.

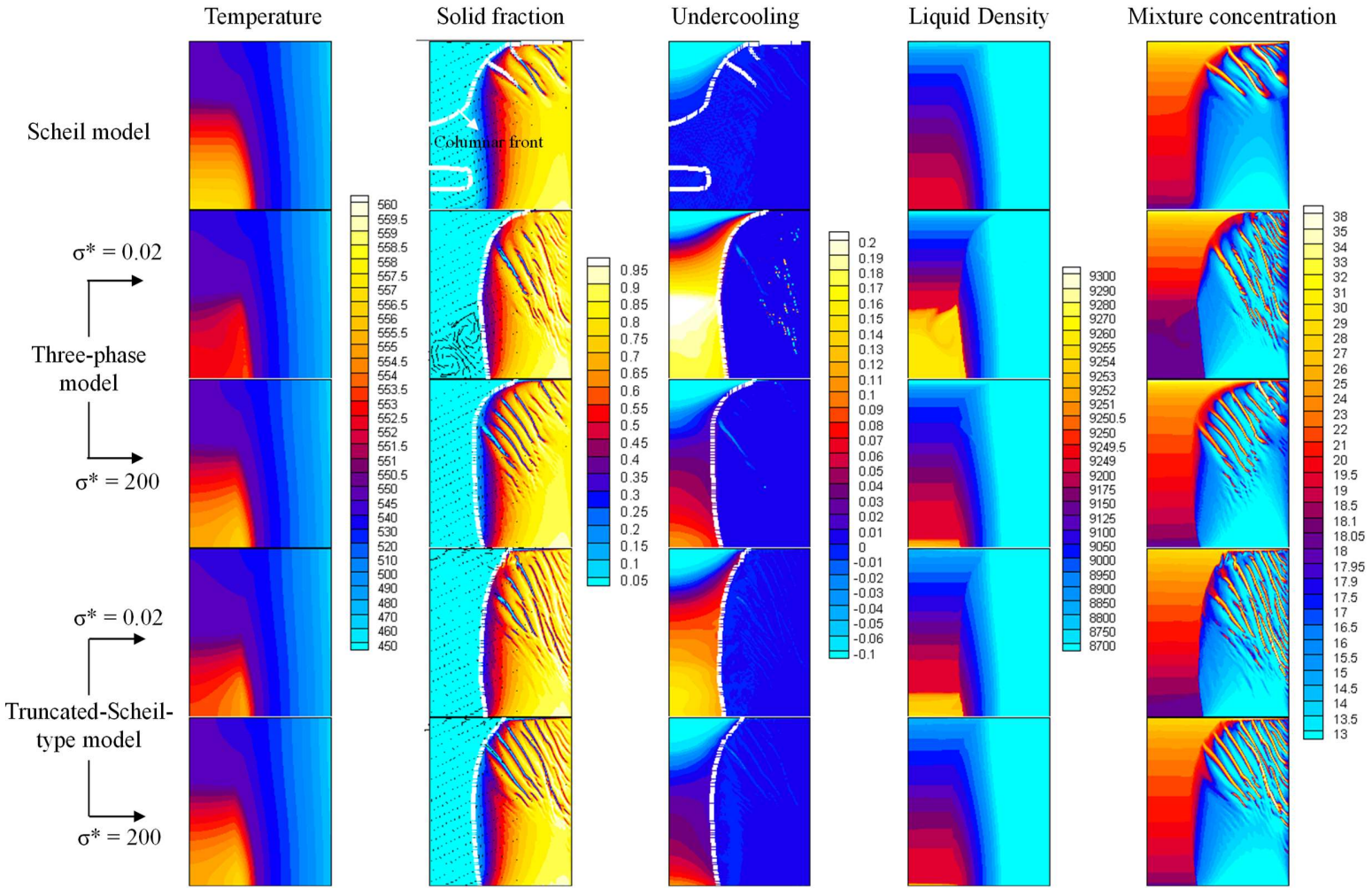

Figure 3-6. Snapshots at t = 120 s of the different quantities predicted by the Scheil, three-phase, and truncated-Scheil-type models. In the second and third columns, the vectors represent the mixture velocity and the white curve represents the columnar front, which corresponds to isoline $g_s = 0.01$ or $\phi = 0$.

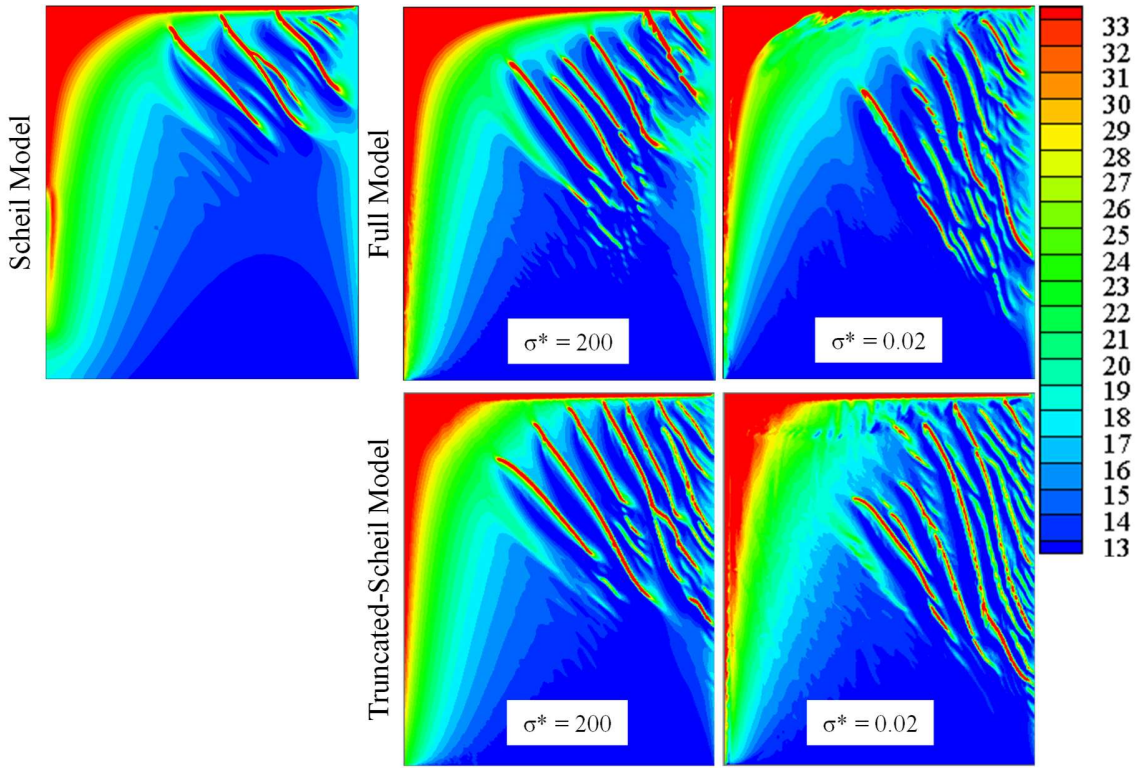

Figure 3-7. Final macrosegregation maps predicted by the Scheil, three-phase, and truncated-Scheil-type models.

Chapter 4: A macroscale model for columnar to equiaxed transition in the presence of melt convection

4.1 Abstract

In the field of metal casting, the prediction of the columnar to equiaxed transition (CET) in the presence of melt convection is still an important challenge. One of the open questions is the role of melt convection on the CET and the effect of the CET on macrosegregation. A three-phase Eulerian volume-averaged model for CET in the presence of melt convection is developed. The model accounts for columnar dendrite tip undercooling and nucleation of equiaxed grains ahead of the columnar tips. The model is used to perform macrosegregation and CET simulations of a numerical benchmark problem involving solidification of a lead-18 wt. pct. tin alloy in a side-cooled cavity. It is found that accounting for undercooling and the nucleation of motionless equiaxed grains dese not change the overall macrosegregation pattern. It only changes the predicted shape and number of channel segregates.

4.2 Introduction

The transition from the elongated grains in the outer portions of a casting to the more rounded grains in the center is termed columnar to equiaxed transition (CET) (15). CET has fascinated researchers in the solidification area for more than 50 years (1). Understanding CET is fundamental in determining what type of grain structure forms in castings of most metal alloys. Often, a fully equiaxed structure is preferred, but the fully columnar structure of many turbine blades are an important exception. Realistic modeling and simulation of CET is still very challenging, because it requires one to simultaneously take into account numerous physical phenomena at several length scales: heat/solute transfer, melt flow, nucleation of equiaxed grains, and growth of columnar and equiaxed grains into an undercooled melt (10).

Hunt (16) proposed the first CET mechanism which is now referred to as *mechanical-blocking*. The hypothesis behind this mechanism is that equiaxed grains nucleate and grow in the

undercooled liquid region ahead of the columnar front. If the volume fraction of the equiaxed grains just ahead of the columnar front becomes greater than 0.49, equiaxed grains will mechanically block further advancement of the front; therefore, CET will occur. Hunt's criterion has been widely used in the literature to predict CET, but the mathematical derivation of the criterion is based on empirical equations. Furthermore, it can be expected that the blocking grain fraction will be different for different alloy systems. For example, Biscuola and Martorano (17) showed that, at least for the Al-Si alloys, using the equiaxed blocking gain fraction of 0.2 will result in CET predictions that are in better agreement with experiments.

To overcome the shortcomings of the mechanical blocking criterion, Martorano et al. (3) introduced the concept of *solutal-blocking*. The physical basis of this criterions is as follows: equiaxed grains can nucleate and grow in the undercooled region ahead of the columnar front. These grains reject solute into the liquid surrounding the grains and enrich it. When the liquid ahead of the columnar front is highly enriched the local undercooling becomes zero; and, therefore, the columnar gets solutally blocked. To incorporate this concept into the mathematical model, the undercooling had to be defined relative to the average local liquid solute concentration, rather than the initial liquid concentration, as was done in the study of Hunt (16). As a result of this new definition for undercooling, when the liquid concentration reaches the equilibrium concentration locally, the local undercooling ahead of the columnar front becomes zero and the columnar front stops: CET happens.

Developing macroscale models to predict CET has been the subject of numerous studies in the past decade (3, 11, 13, 58). Most of these studies are based on the framework developed in the pioneering work of Wang and Beckermann (2, 10, 48, 49). In the framework of Wang and Beckermann, a solidifying system is assumed to consist of three phases: a solid phase, an inter-dendritic liquid phase, and an extra-dendritic liquid phases. The two liquid phases are separated by the grain envelope, which is a virtual and smooth surface that connects the primary tips and the tips of actively growing secondary arms. A secondary arm is defined as active when it is longer than the next active secondary arm closer to the primary tip. Two liquid phases are introduced in the model because the solute diffusion is governed by length scales of different orders of magnitude: the secondary arm spacing in the inter-dendritic liquid and the distance between grains

in the extra-dendritic liquid. This framework has been extensively by other researcher to develop solidification models (11-13, 22, 23, 43-45, 59).

Wang and Beckermann used their framework (60) to develop a model for equiaxed solidification in the presence of melt convection (2, 48, 49) and a model for CET (50) in the *absence* of melt convection. In this chapter, the framework of Wang and Beckermann (60) is used to develop a model for CET in the presence of melt convection.

4.3 Mathematical model

The equations of the CET model introduced in this chapter are similar to the equations of the three-phase model developed for fully columnar solidification in the previous chapter. The only difference is that equations this and that need to be modified as follows to account for nucleation of equiaxed grains. This modification is discussed next.

To incorporate equiaxed solidification, in the phase-diagram relation for the three-phase model developed in the previous chapter (i.e., equation (3-18)), the term on the left-hand side of the top arrow should be replace with $T \le T_{nuc} = T_{liq}\left(\bar{C}_d\right) - \Delta T_{nuc}$, where T_{nuc} is the nucleation temperature and ΔT_{nuc} is the nucleation undercooling. So, in the CET model, the phase-diagram relation reads

$$\begin{aligned} &\text{Primary solidification}: \; T \le T_{nuc} = T_{liq}\left(\bar{C}_d\right) - \Delta T_{nuc} \quad \rightarrow \quad \bar{C}_d = C_l^* = \frac{T - T_f}{m_l} \\ &\text{Eutectic solidification}: \; \bar{C}_d = C_{eut} \text{ and } g_l \ge 0 \quad \rightarrow \quad T = T_{eut} \quad \text{and} \quad k_0 = 1 \end{aligned} \tag{4-1}$$

In addition, the relation to calculate the envelope surface area per unit volume of the REV, S_{env}, in the previous chapter (i.e., equation (3-19)) needs to be modified as

$$S_{env} = \begin{cases} 0 & \phi < 0 \quad \text{and} \quad T > T_{liq}\left(\bar{C}_e\right) - \Delta T_{nuc} \\ \dfrac{3\left(1-g_e\right)^{2/3}}{R_f} & \text{otherwise} \end{cases} \tag{4-2}$$

where R_f is calculated form (3)

$$R_f = \begin{cases} \lambda_1/2 & \phi > 0 \quad : \text{columnar} \\ \left[3/(4\pi n)\right]^{1/3} & \phi < 0 \text{ and } T < T_{nuc}\left(\bar{C}_e\right) \quad : \text{equiaxed} \end{cases} \tag{4-3}$$

4.4 Problem statement

The problem studied in this chapter is the same as the numerical solidification benchmark problem studied in the previous chapter and for conciseness its description is not repeated here.

4.5 Results and discussion

In Figure 4-1, the prediction of the model in the absence of melt convection (the top row) and in the presence of melt convection (the bottom row) and at t = 10 s, are shown. First, the results in the absence of melt convection are discussed. From the contour plots at the top row, one can see the prediction of the model in the absence of melt convection are, as expected, one dimensional. In other words, the different quantities vary only in the horizontal direction and the columnar front is a vertical line. From these plots one can also see that the solid fraction ahead of the columnar front is about 0.05, which indicates that the equiaxed grains have already nucleated ahead of the front. However, the solute rejected from these grains was not strong enough to vanish the undercooling and the undercooling ahead of the columnar front is still relatively high. Therefore, the columnar front is expected to continue moving to the left parts of the cavity towards to middle. Next, the results in the presence of melt convection are discussed.

In the presence of melt convection, the main flow pattern in the cavity is a clock-wise rotating convection cell. This cell is produced by the downwards flow ahead of the columnar front, which is itself, due to the downwards thermal buoyancy forces. This convection cell carries the low temperature liquid ahead of the columnar front to the bottom parts of the cavity and, therefore, there is more undercooled liquid at the bottom parts of the cavity than at the top. The flow inside

the mush, in contrast to the flow ahead of the columnar front, is moving upwards due to the upwards solutal buoyancy forces. This upwards flow needs to make a sharp turn left when it reaches the top of the cavity and this give the highly localized left moving flow near the top wall of the cavity. This flow carries the solute rejected during the solidification inside the mush away to the bulk and therefore the liquid ahead of the front at the top right corner of the cavity is highly undercooled. Therefore, the equiaxed grains start nucleating there. These equiaxed grains slow down the columnar front locally.

In Figure 4-2Figure 4-3, the prediction of the model in the absence of melt convection (the top row) and in the presence of melt convection (the bottom row) and at t = 20 s, are shown. The distributions of the different quantities at this time are very similar to what was observed at t = 10 s. The front has moved further to the left. The clock-wise rotating convection cell in front of the edge of the mushy zone and the left moving flow near the top of the cavity are both visible at t = 20 s. More equiaxed grains have nucleated in front of the columnar front at the top right corner of the cavity and the undercooling starts to vanish locally. This indicates that CET is expected to happen soon at this part of the cavity. Also, formation of channel segregates is clearly visible from the solid fraction contours. Also, note that, due to the upwards flow inside the mush, the solid that is forming at the bottom right corner of the cavity has concentration lower than the nominal concentration $C_0 = 18$ wt. pct.

In Figure 4-3, the prediction of the model in the absence of melt convection (the top row) and in the presence of melt convection (the bottom row) and at $t = 60$ s, are shown. From the solid fraction contour plots, it can be seen that the channels exist both in the columnar and equiaxed regions of the mush. Formation of channels in the equiaxed region is attributed to the fact that the equiaxed grains are assumed to be motionless. In other words, it is assumed that these grains are fixed in their place after nucleation. The convection cell that was observed in the earlier times is now much smaller. The flow inside the mush is now much weaker than the previous times and, as the result of that, the left moving flow that was observed close to that top wall of the cavity at the earlier times has now fully disappeared; the isothermal inside the mush are nearly vertical and very similar to the no flow isotherms. Flow at the upper parts of the cavity in front of the mush does not have

a regular pattern and that is probably because the flow there is being influenced by the highly unsteady flow that is being rejected from the channels in the mush.

In Figure 4-4 and Figure 4-5, similar predictions but at two late solidification times of t = 120 s and t = 240 s, respectively, are shown. From these plots, it can be seen that, at t = 120 s, CET at the upper half of the cavity has already happened, while, at the bottom parts of the cavity, the columnar front is still moving to the left, due to the significant local undercooling ahead of the front. At t = 240 s, the undercooling ahead of the columnar front at the bottom parts of the cavity has also vanished and CET has happened everywhere in the cavity.

In Figure 4-6, the final macrosegregation patterns (i.e., the final distribution of the mixture concentration $\overline{C} = g_s\overline{C}_s + g_d\overline{C}_d + g_e\overline{C}_e$) predicted by the model in the absence and presence of equiaxed grains (the second and third columns) are compared with the macrosegregation pattern predicted by the Scheil-type model introduced in the previous chapter. From the plots it can be seen that the overall macrosegregation are very similar. Similar to the patterns observed in the previous chapter, it consists of a region with negative segregation (i.e., $C < C_0$) at the bottom of the cavity. This is because solute rejected during solidification at this part of the cavity is carried away by the local melt convection. This negative segregation region forms at the expense of positively segregated regions at the top near the symmetry line and in the middle so that the global species balance is maintained. It can also be observed that accounting for the nucleation of motionless equiaxed grains dese not change the overall macrosegregation pattern.

4.6 Conclusions

A three-phase Eulerian volume-averaged model for CET in the presence of melt convection was developed. The model accounts for columnar dendrite tip undercooling and nucleation of equiaxed grains ahead of the columnar tips. The model was used to perform macrosegregation and CET simulations of a numerical benchmark problem involving solidification of a lead-18 wt. pct. tin alloy in a side-cooled cavity. It was found that accounting for the nucleation of motionless equiaxed grains dese not change the overall macrosegregation pattern.

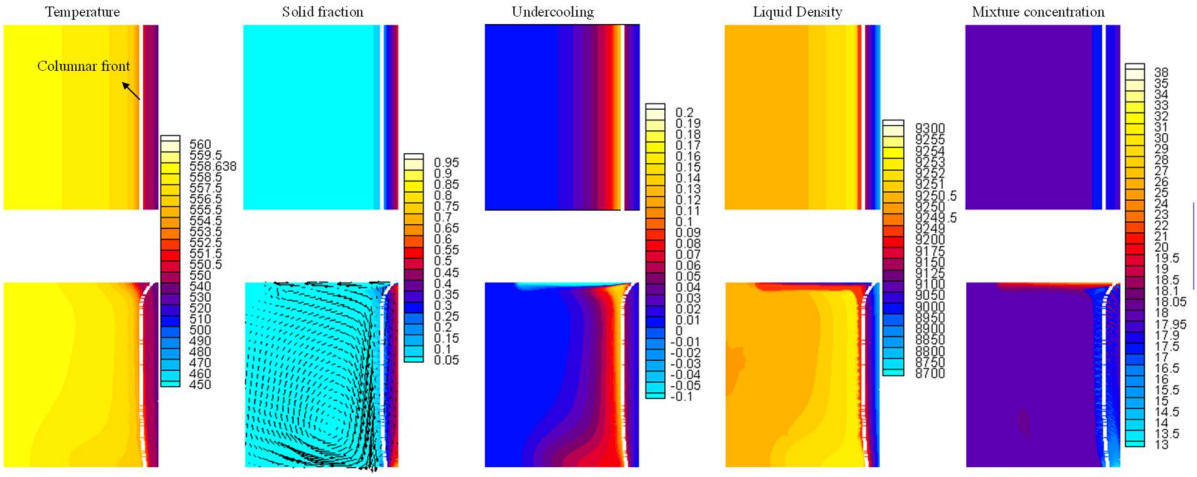

Figure 4-1. Snapshots at t = 10 s of the different quantities and the position of the columnar front, which corresponds to isoline $\phi = 0$. In the second and third columns, the vectors represent the mixture velocity.

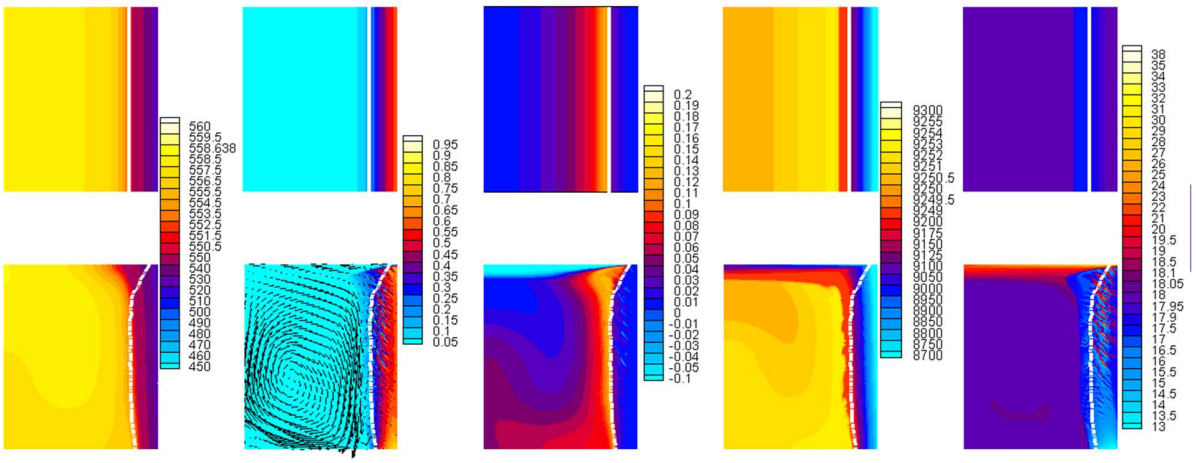

Figure 4-2. Snapshots at t = 20 s of the different quantities and the position of the columnar front, which corresponds to isoline $\phi = 0$. In the second and third columns, the vectors represent the mixture velocity.

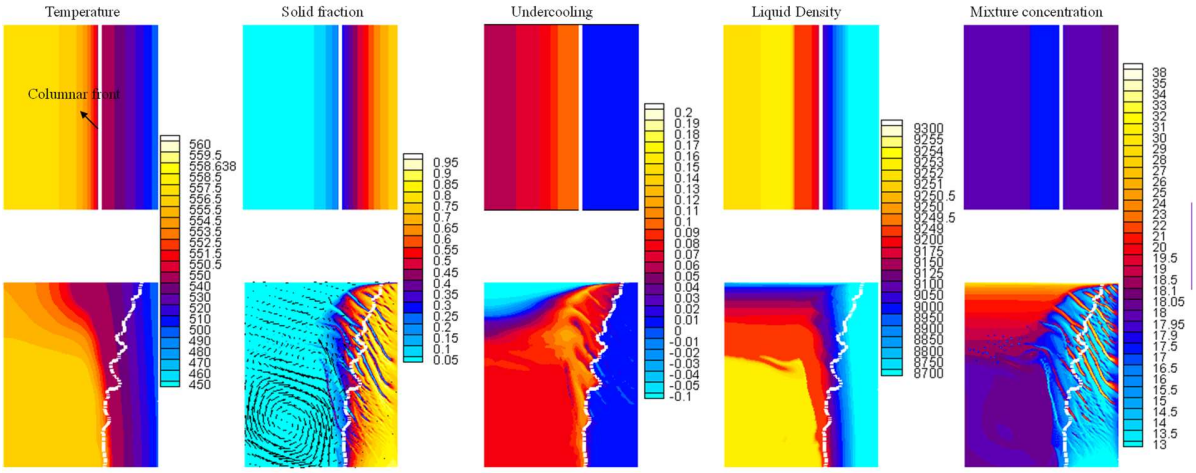

Figure 4-3. Snapshots at t = 60 s of the different quantities and the position of the columnar front, which corresponds to isoline $\phi = 0$. In the second and third columns, the vectors represent the mixture velocity.

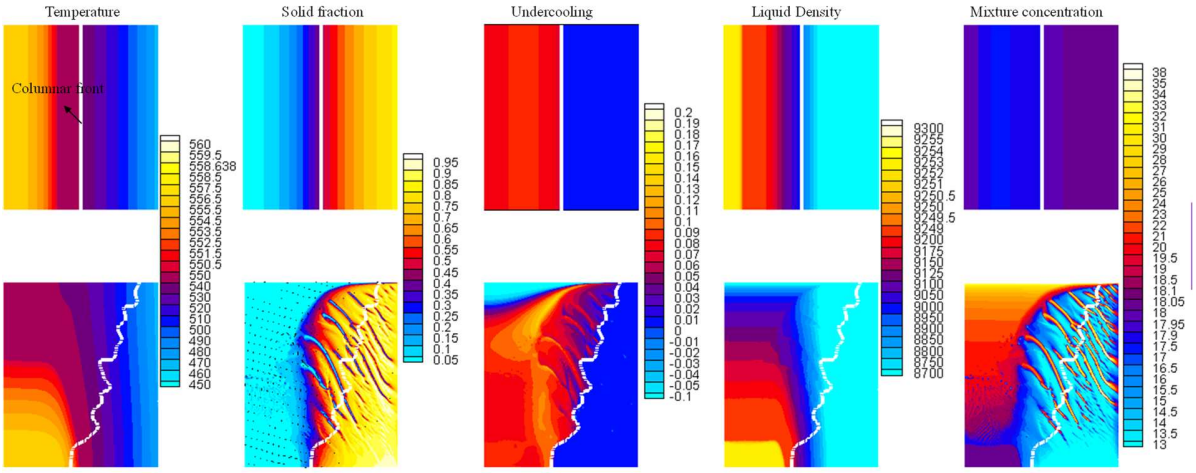

Figure 4-4. Snapshots at t = 120 s of the different quantities and the position of the columnar front, which corresponds to isoline $\phi = 0$. In the second and third columns, the vectors represent the mixture velocity.

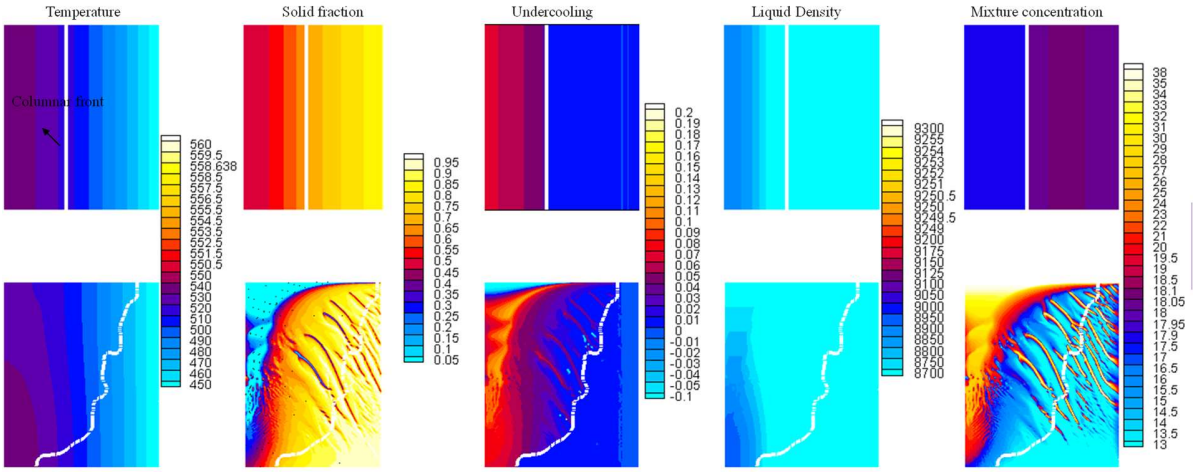

Figure 4-5. Snapshots at t = 240 s of the different quantities and the position of the columnar front, which corresponds to isoline $\phi = 0$. In the second and third columns, the vectors represent the mixture velocity.

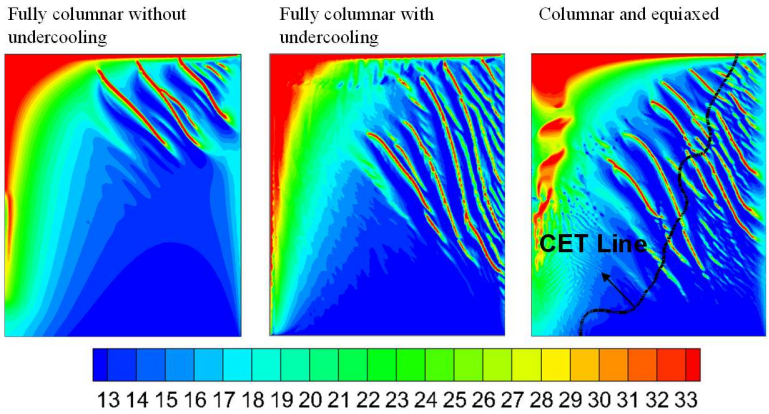

Figure 4-6. final macrosegregation map predicted in the absence and presence of undercooling and for fully columnar and mixed columnar and equiaxed.

Chapter 5: Upscaling mesoscopic simulation results to develop constitutive relations for macroscopic modeling of equiaxed dendritic solidification

5.1 Abstract

Macroscale solidification models incorporate the microscale and mesoscale phenomena using constitutive relations. These relations can be obtained by simulating those phenomena inside a Representative Elementary Volume (REV) and then upscaling the results to the macroscale. In the present study, a previously developed mesoscopic envelope model was used to perform three-dimensional simulations of equiaxed growth at a spatial scale that corresponds to a REV. The mesoscopic results were upscaled by averaging them over the mesoscopic simulation domain. The upscaled results were used to develop new constitutive relations, which, unlike the currently available relations, do not rely on highly simplified assumptions about the grain envelope shape or the solute diffusion conditions around it. The relations are verified by comparing the predictions of the macroscopic model with the upscaled mesoscopic results at different solidification conditions. These relations can now be used in macroscopic models of equiaxed solidification to incorporate more realistically the microscale and mesoscale phenomena.

5.2 Introduction

Solidification is a complex multiscale problem that is controlled by phenomena occurring at length scales that are distinct from each other and range over roughly five orders of magnitude (61, 62). At the macroscale (i.e., the scale of the whole casting) heat transfer and typically melt convection take place, grains can move, and the solid might deform. At the mesoscale (i.e., the scale of the primary arms spacing ranging from 1 to 0.1 mm) grains grow and determine the final grain structure. At the microscale (i.e., the scale of a dendrite tip radius ranging from 10^{-2} to 10^{-3} mm) the competition between the microscale heat/solute diffusion and surface tension determines the dendrite tip radius and velocity. What makes solidification modeling a complex task is that there is a strong inter-scale coupling between the phenomena occurring at the different length scales.

For example, macroscale melt convection influences the microscale solute diffusion, and is, itself, influenced by the microscopic structure of the semi-solid mush. Because of this coupling, macroscale models need to incorporate the microscale and mesoscale phenomena. One might, however, wonder how this can be achieved because, in macroscale models, a unit cell is always much larger than the scale on which the microscale and mesoscale phenomena take place.

Microscale and mesoscale phenomena can be incorporated in the macroscale models using volume-averaging methods. Averaging concepts were first applied in the solidification field by Beckermann and Viskanta (63) in the mid to late 1980s and later significantly extended by Ni and Beckermann (64) and Wang and Beckermann (2, 10, 48, 49, 60). Volume-averaging is now a widely accepted method in developing macroscale solidification models as is indicated by more than one thousand citations to the original chapters. Volume-averaged macroscale models have been used to simulate solidification in systems as large as steel ingots (65, 66). It is beyond the scope of this chapter to review the governing equations in detail, but thorough reviews are available (60, 67). In brief, these models are derived by averaging the local equations (i.e., equations that are valid at the microscopic scale) for each phase over a small volume that contains all the phases present in the system and is called the Representative Elementary Volume (REV). The size of a REV corresponds to a unit cell in macroscopic simulations. The resulting volume-averaged equations contain phase fractions and source terms. These source terms, which account for the microscale and mesoscale transport phenomena occurring at the interfaces between the different phases, depend on variables that are not predicted by the macroscopic model, because the lower scale information that these variables represent has been lost in the averaging process. Accurate calculation of these source terms, therefore, requires one to do a formal analysis on the REV scale and then pass up the information to the macroscale, through constitutive relations, in a process called upscaling. The term upscaling simply means that in the ladder of length scales information is passed up from a smaller scale to a larger scale by averaging. This upscaling has never been tried in the field of solidification, mainly because of the complexity that arises as the result of the large range of length scales that need to be resolved. In other words, in solidification, there is a large gap between the involved micro and macro length scales. Therefore, the currently available constitutive relations have been based on simplifying assumptions rather than a formal REV scale analysis.

The gap between the micro and macro scales can be bridged using the mesoscopic model originally developed for pure materials by Steinbach et al. (61, 62), extended for binary alloys by Delaleau et al. (68), and further validated by Souhar et al. (69) by performing three-dimensional simulations of equiaxed growth and comparing the results with experimental scaling laws (70). Mesoscopic models directly resolve the transport phenomena on the REV scale, by solving an equation for the heat/solute transport on this scale, and incorporate microscale phenomena, by using a local analytical solution for the microscale heat/solute transport. The computational power requirement of these models is significantly lower than the models that resolve the microscale phenomena directly, such as the phase field models (61, 62). This allows one to do three-dimensional simulations at low undercoolings and at relatively large domain sizes that correspond to a REV.

In this chapter, the mesoscopic envelope model of Delaleau et al. (68) was used to perform three-dimensional simulations of equiaxed growth on a REV scale. Simulations were performed at a large range of initial undercoolings and grain densities and the results were upscaled by averaging them over the volume of the REV. The upscaled results are examined in detail and used to develop constitutive relations for macroscale solidification models. The constitutive relations were verified by comparing the predictions of the volume-averaged macroscopic model with the upscaled mesoscopic results at different solidification conditions.

The rest of the chapter is organized as follows: The macroscopic model is introduced in section 5.3. A brief introduction of the mesoscopic model and mesoscopic results are presented in section 5.4. The constitutive relations are developed in section 5.5 and are verified in section 5.6.

5.3 Volume-averaged macroscopic model

In this section, the conservation equations of the volume-averaged macroscopic model used in the present study are first introduced. It is shown that these equations contain variables that need to be obtained from constitutive relations. The constitutive relations are discussed next.

5.3.1 Conservation equations

Following the pioneering work of Wang and Beckermann (2, 10, 48, 49, 60), to develop a macroscopic model for equiaxed solidification in an undercooled melt, a solidifying system is first assumed to consist of three phases: solid, inter-dendritic liquid, and extra-dendritic liquid. The two liquid phases are separated by the grain envelope, which is a virtual and smooth surface that connects the primary tips to the tip of actively growing secondary arms. A secondary arm is defined as active when it is longer than the next active secondary arm closer to the primary tip. Figure 1 shows a schematic of a grain envelope and the regions of the solid, inter-dendritic liquid, and extra-dendritic liquid phases, denoted by *s*, *d*, and *e*, respectively. Writing the local (i.e., microscopic level) equations for continuity and solute balance in the extra-dendritic liquid in the absence of melt convection and solid motion, and then averaging them over the volume of the REV results in the following volume-averaged equations for the average growth kinetics of and solute diffusion rates from the dendrite envelopes, respectively:

$$\frac{dg_{env}}{dt} = S_{env} w_{env} \tag{5-1}$$

$$\frac{\partial}{\partial t}\left(g_e \bar{C}_e\right) = \frac{\partial g_e}{\partial t} C_l^* + S_{env} \frac{D_l}{\delta_{env}} \left(C_l^* - \bar{C}_e\right) \tag{5-2}$$

where g_{env}, $g_e = 1 - g_{env}$, S_{env}, w_{env}, $\bar{C}_e$, C_l^*, D_l and δ_{env} are the envelope fraction (i.e., grain fraction), extra-dendritic liquid fraction, envelope surface area per unit volume of the REV, average envelope growth velocity, average solute concentration in the extra-dendritic liquid, equilibrium solute concentration in the liquid, solute mass diffusivity in the liquid, and average diffusion length around the envelopes, respectively. Equation (5-1) indicates that the envelope volume fraction g_{env} will increase and growth will continue, as long as w_{env} is greater than zero. On the right-hand-side of equation (5-2), the first and second terms represent the microscopic solute transfer (from the inter-dendritic to extra-dendritic) at the d-e interface due to the movements of this interface and due to the diffusion at this interface, respectively. Finally, the term $C_l^* - \bar{C}_e$ is linked to the average undercooling in the extra-dendritic liquid undercooling, which is the driving force for growth.

In equations (5-1) and (5-2), the variables S_{env}, w_{env}, and δ_{env} need to be obtained from constitutive relations. The next section discusses the procedure to derive these relations and also the assumptions that have been commonly used in the literature to derive the currently available constitutive relations.

5.3.2 Constitutive relations

To obtain the constitutive relations for the envelope variables S_{env}, w_{env}, and δ_{env}, the envelope is first approximated by the volume-equivalent sphere, referred to as sphere hereafter. A schematic of the sphere is also shown in Figure 1. Then, the envelope variables are related to the sphere variables as follows.

5.3.2.1 Relating envelope variables to sphere variables

The envelope surface area per unit volume of the REV, S_{env}, is related to the sphere surface area per unit volume of the REV, S_{sp}, directly from the definition of the envelope sphericity ψ

$$S_{env} = \frac{S_{sp}}{\psi} \tag{5-3}$$

One should note that the sphericity ψ is a purely geometrical variable (i.e., it depends solely on the geometry of the envelope). The sphericity of a sphere is equal to unity by definition, and any other shape has a sphericity less than unity (for example, the sphericity of an octahedron is 0.85 (71)).

To relate w_{env} to the sphere growth velocity w_{sp}, one needs to recognize that equation (5-1) holds for any shape including a sphere; since the volume of an envelope and its sphere are equal, the time derivative of envelope volume fraction and sphere volume fraction will be equal and one can, therefore, write $S_{env} w_{env} = S_{sp} w_{sp}$. In this relation, S_{env} can be substituted from equation (3) to give:

$$w_{env} = \psi w_{sp} \tag{5-4}$$

Next, the variation of ψ during growth is discussed. Equiaxed growth starts from a spherical nucleus, which has ψ=1 and, from equation (5-4), $w_{env}/w_{sp} = 1$. As the spherical nucleus grows into the undercooled melt surrounding it, its shape becomes unstable and relatively fast growth along the energetically favorable crystallographic directions, compared to growth along the other directions, gradually transitions the shape into a dendrite, which has ψ<1and, again from equation (5-4), $w_{env}/w_{sp} < 1$. Therefore, during growth, ψ and w_{env}/w_{sp} decrease from their initial value of unity.

In the current literature, there are no relations to predict the decrease in ψ or w_{env}/w_{sp} during growth. Therefore, macroscopic models had to rely on pre-determined and constant values for ψ and w_{env}/w_{sp} . For example, in the study of Martorano et al. (3), ψ and w_{env}/w_{sp} have been assumed to be equal to unity during the entire growth period; in other words, it is assumed that grains retain their initial spherical shape. In the studies of Ludwig and Wu (12, 59), ψ is assumed to be equal to 0.85 (i.e., the sphericity of an octahedron) and w_{env}/w_{sp} is assumed to be equal to unity. Disregarding the decrease in ψ and w_{env}/w_{sp} during growth can be expected to result in inaccuracies in the macroscopic models. In fact, Rappaz and Thevez (72), compared the cooling curves measured in the experiments with the ones predicted by their solute diffusion model and noticed that their model does not predict the recalescence very well. They attributed this partly to the fact that in their model, sphericity was assumed to be equal to unity during the entire growth. As another example, Wu et al. (11, 13) did columnar to equiaxed (CET) simulations with different values for sphericity and found that the CET position is highly sensitive to the sphericity value. Developing a relation to predict the decreases in ψ and, therefore, in w_{env}/w_{sp} , during growth is one of the objectives of this study.

To relate δ_{env} to the sphere diffusion length δ_{sp}, one needs to realize that the envelope diffusion length is determined by the diffusion field around the envelope. It is therefore, in general, a

complicated function of the envelope shape, size and growth velocity and a relation between δ_{env} and δ_{sp} cannot be obtained from a simple and purely geometrical analysis, such as the one we did to obtain equation (5-4). Such a relation has never been proposed in the literature mainly because the complex nature of solute diffusion field around an envelope precludes one from finding an analytical relation for δ_{env}. Macroscopic models, therefore, have simply assumed $\delta_{env} = \delta_{sp}$. This assumption might have reasonable accuracy during the initial stages of growth, when the envelope is spherical; however, as the envelope becomes dendritic with growth, the assumption can be expected to become increasingly inaccurate. Developing a relation for δ_{env} is another objective of this study.

5.3.2.2 Relations for Sphere Variables

In the previous section, the envelope variables were related to the sphere variables. In this section, the relations for the sphere variables are outlined first and then interesting limiting cases of the relation for δ_{sp} are discussed.

The sphere surface area per unit volume of the REV, S_{sp}, is calculated from

$$S_{sp} = \frac{4\pi n R_{sp}^2}{\left(4\pi n R_{sp}^3/3\right)/g_{env}} = \frac{3g_{env}}{R_{sp}} \tag{5-5}$$

where R_{sp} is the sphere radius. Note that the denominator of the right-hand side of the first equality represents the volume of the REV. The sphere radius R_{sp} is calculated from

$$\frac{dR_{sp}}{dt} = w_{sp} \tag{5-6}$$

Next, the model needs a relation for w_{sp}. Currently, most of the macroscopic models assume $w_{sp} = V_t$ (2, 3). However, this assumption simply contradicts the definition of the sphere. This is

because a sphere with $w_{sp} = V_t$ will have $R_{sp} = l_t$ and, therefore, its volume will be higher than the envelope volume and not equal to it. Developing a relation for w_{sp} is one of the objectives of the present study.

The sphere diffusion length δ_{sp} is calculated from the relation developed by Martorano et al. (3)

$$\frac{\delta_{sp}}{R_{sp}} = \frac{R_{sp}}{R_f^3 - R_{sp}^3}\left\{\left(\frac{R_f R_{sp}}{Pe_{sp}} + \frac{R_{sp}^2}{Pe_{sp}^2} - R_f^2\right)e^{-Pe_{sp}\left(\frac{R_f}{R_{sp}}-1\right)} - \left(\frac{R_{sp}^2}{Pe_{sp}} + \frac{R_{sp}^2}{Pe_{sp}^2} - \frac{R_f^3}{R_{sp}}\right)\right.$$
$$\left. + Pe_{sp}\frac{R_f^3}{R_{sp}}\left(e^{-Pe_{sp}\left(\frac{R_f}{R_{sp}}-1\right)}\frac{\mathrm{Iv}\left(Pe_{sp}R_f/R_{sp}\right)}{Pe_{sp}R_f/R_{sp}} - \frac{\mathrm{Iv}\left(Pe_{sp}\right)}{Pe_{sp}}\right)\right\} \quad (5\text{-}7)$$

where $Pe_{sp} = w_{sp}R_{sp}/D_l$ is the sphere growth Péclet number, R_f is the final grain radius, and $\mathrm{Iv}(\ )$ is the Ivantsov function. This equation indicates that the diffusion length around a sphere depends on the radius and growth velocity of the sphere and the final grain radius. A better insight into this dependence can be obtained by simplifying equation (5-7) in two interesting limiting cases: the high Pe_{sp} limit and the high R_f limit (i.e., the single grain limit). This is discussed next.

In the high Pe_{sp} limit, $e^{-Pe_{sp}\left[\left(R_f/R_{sp}\right)-1\right]}$ converges to zero and therefore, inside the curly brackets on the right-hand-side of the equation, the first three terms and the seventh term can be dropped; the fifth term becomes negligible compared to the fourth term; and, finally, in the last term, $\mathrm{Iv}\left(Pe_{sp}\right)$ can be approximated by $1 - 1/Pe_{sp}$ (73). Therefore, equation (5-7) simplifies to

$$\frac{\delta_{sp}}{R_{sp}} = \frac{1}{Pe_{sp}} \quad (5\text{-}8)$$

Interestingly, equation (5-8) indicates that in in the high Pe_{sp} limit, δ_{sp} does not depend on R_f. Using the definition of Pe_{sp}, equation (5-8) can be recast into

$$\delta_{sp} = \frac{D_l}{w_{sp}} \tag{5-9}$$

The second interesting limiting case of equation (5-7) is the high R_f limit. In this limit, similar to the high Pe_{sp} limit discussed above, $e^{-Pe_{sp}\left[\left(R_f/R_{sp}\right)-1\right]}$ converges to zero. Therefore, inside the curly brackets, the first three terms and the seventh term can be dropped; the fourth and fifth terms become negligible compared to the sixth term; finally, in the denominator of the term outside the curly brackets, R_{sp}^3 becomes negligible compared to R_f^3; therefore, equation (5-7) reduces to

$$\frac{\delta_{sp}}{R_{sp}} = 1 - \mathrm{Iv}\left(Pe_{sp}\right) \tag{5-10}$$

Note that the high Pe_{sp} limit of this equation is, as expected, identical to the high Pe_{sp} limit of equation (5-7) (i.e., equation (5-8)). In the low Pe_{sp} limit, one has $\mathrm{Iv}\left(Pe_{sp}\right) \to 0$ (3) and equation (5-10) reduces to

$$\delta_{sp} = R_{sp} \tag{5-11}$$

5.3.2.3 Primary tip velocity

Macroscopic models need to predict the primary tip velocity V_t, referred to as the tip velocity hereafter, because the growth of an envelope, at least during the early stages, is mainly driven by the growth of its primary arms. Therefore, the tip velocity V_t can be expected to be one of the main, if not the main, factor in determining w_{sp}. In addition, V_t is required in predicting the primary arm length l_t from

$$\frac{dl_t}{dt} = V_t \tag{5-12}$$

To understand the variations of V_t during the quasi-steady growth of assembly of dendrites, let us first consider two dendrites located at the distance $2R_f$ from each other inside a uniformly undercooled melt, as shown schematically in Figure 2 at (a) an early time and (b) a late time during growth. Due to the symmetry, only half of the dendrites are shown. The profiles of solute concentration in the extra-dendritic liquid are also shown in the figure. Note that the concentration at the tip is equal to the equilibrium concentration C_l^* and, at some distance ahead of the tip, it declines to the far field solutal concentration C_f.

At the early stage of growth, shown in Figure 2(a), there is a distance between the edges of the solutal boundary layers ahead of the tips and, therefore, the solutal field ahead of one dendrite is not influenced by the presence of the other. In other words, the dendrites are not interacting. This stage of growth is, therefore, referred to as the non-interacting stage. At this stage, the growth of the dendrites is virtually the same as the growth of a single dendrite into an essentially infinite medium. As the dendrites keep growing, the distance between the edges of the boundary layers decreases and at some intermediate time the edges meet. Once that happens, the solutal boundary layer ahead of each of the dendrites starts to get influenced by the presence of the other dendrite. In other words, the dendrites start to interact. This stage is called the interacting stage. Next, the variations of $\overline{C}_e$ and $\overline{C}_f$ during these two stages are discussed. During the non-interacting stage, the far field solute concentration C_f is constant and equal to the initial solute concentration $\overline{C}_e(t=0)$; furthermore, C_f is less than the average solute concentration in the extra-dendritic liquid $\overline{C}_e(t)$: $C_f = \overline{C}_e(t=0) < \overline{C}_e(t)$. During the interacting stage, however, C_f is greater than $\overline{C}_e(t=0)$ but still less than $\overline{C}_e(t)$: $\overline{C}_e(t=0) < C_f < \overline{C}_e(t)$. These two relations are important, and we will refer to them subsequently when we discuss the time variations of V_t during these two stages.

As the primary arm of a dendrite grows, it rejects solute (assuming $k_0 < 1$). For growth to continue, the rejected solute needs to be dissipated away from the tip towards the bulk liquid. The balance between the solute flux rejected at the tip and the solute flux diffusing away from the tip determines the tip velocity. The latter flux is proportional to the solute gradient at the tip. During the non-interacting stage of growth, the diffusion field ahead of the tip and therefore the diffusion flux at the tip remain constant. This causes V_t to remain constant. During the interacting stage, however, C_f increases with time, which makes the solute profiles progressively smoother; therefore, the solute diffusion flux at the tip and consequently V_t both decrease with time. Prediction of V_t during these stages is discussed next.

In macroscopic models of solidification, the most commonly used relation for predicting V_t is the relation proposed by Ivantsov (74):

$$\Omega_f = Pe_t \exp\left(Pe_t\right) \mathrm{E}_1\left(Pe_t\right) \tag{5-13}$$

where Ω_f is the far field undercooling defined as

$$\Omega_f = \frac{C_l^* - C_f}{\left(1-k_0\right) C_l^*} \tag{5-14}$$

and $Pe_t = V_t R_t / \left(2D_l\right)$ is the dendrite tip Péclet number, $R_t = \sqrt{d_0 D_l / \left(V_t \sigma^*\right)}$ is the tip radius, k_0 is the partition coefficient, d_0 is the capillary length, σ^* is the tip selection parameter, and the function $\mathrm{E}_1(\ )$ is the exponential integral function. Equation (5-13) is the exact similarity solution for the solute diffusion field around a paraboloid of revolution during its quasi-steady shape-preserving growth into an infinite medium with uniform and constant far field undercooling Ω_f. This equation has been shown to provide accurate predictions of the primary tip velocity V_t during the quasi-steady growth of a single dendrite into an essentially infinite medium (75). For the quasi-steady growth of multiple dendrites, equation (5-13) can be expected to accurately predict V_t

during the non-interacting stage. To predict V_t during the interacting stage, modifications to this equation have been proposed (76, 77). These modifications are, however, limited to isothermal dendrites and specific dendritic arrangements and a generally valid relation to predict V_t during the interacting stage is still not available. Therefore, similar to numerous studies in the literature (2, 3, 10, 49, 58), in this chapter, equation (5-13) is used to predict V_t during both non-interacting and interacting stages.

In using equation (5-13) to predict V_t during growth of multiple dendrites it should be kept in mind that, as already discussed in connection with Figure (2), during the entire growth period (i.e., interacting and non-interacting stages), one has $C_f < \bar{C}_e$. Therefore, the far field undercooling Ω_f will always be higher than the average undercooling in the extra-dendritic liquid Ω_e, which is defined as

$$\Omega_e = \frac{C_l^* - \bar{C}_e}{(1-k_0)C_l^*} \tag{5-15}$$

In other words, during the entire growth period, $\Omega_e < \Omega_f$. Therefore, if, in equation (5-13), one uses Ω_e instead of Ω_f, the tip velocity V_t will be underpredicted. Using Ω_e in this equation has been, however, a common practice in the literature (2, 10, 49) because, currently, there are no relations to predict Ω_f. Developing a relation to predict Ω_f is one of the objectives of this study.

5.4 Mesoscopic envelope model

The mesoscopic envelope model used in the present study was originally developed by Delaleau (68) and recently used by Souhar et al. (69) to perform three-dimensional simulations of equiaxed growth. The reader is referred to these chapters for the details of the model and the complete set of equations. In brief, the model approximates the complex dendritic structure with an envelope and a solid fraction field inside the envelope. The normal growth velocity at any point on the envelope is calculated from the local dendrite tip velocity, obtained from an analytical stagnant

film model, and the angle between the growing dendrite arm and the envelope normal. The liquid inside the envelope and on the envelope surface is assumed to be well-mixed and in equilibrium with the solid while the liquid outside the envelope is generally undercooled. The solid fraction field inside the envelope and the solute concentration field in the extra-dendritic liquid outside the envelope C_e are obtained from the numerical solution of a solute conservation equation that is valid both inside and outside the envelope. Hence, the solutal interactions between the growing grains are fully resolved.

5.4.1 Mesoscopic simulations

The first set of mesoscopic simulations were performed for the *isothermal* growth of a single grain growing into an essentially infinite domain (Figure 3a) and for multiple grains (Figure 3b) with high/low grain densities of $R_f/\left[D_l/V_{Iv}\left(\Omega_0\right)\right]$ = 4.03/6.31, where $V_{Iv}\left(\Omega_0\right)$ is the Ivantsov tip velocity (i.e., the velocity predicted by equation (5-13)) corresponding to the initial undercooling Ω_0. Each case was simulated for Ω_0 = 0.05 and 0.15. For the multiple grain cases, the grains were arranged periodically in a BCC lattice, with the primary arms growing along the axes (Figure 3b).

In figure (4), an example of the mesoscopic simulation results is shown. The figure, which is for the multiple grain case with the low undercooling ($\Omega_0 = 0.05$) and high grain density ($R_f/\left[D_l/V_{Iv}\left(\Omega_0\right)\right] = 4.03$), shows the solid fraction g_s and the solute concentration in the extra-dendritic liquid C_e, plotted in the interior and exterior of the envelopes, respectively, at different times. It can be seen that (see plot 4(a)), as expected (see the discussion below equation (5-4)), the envelope is initially spherical, but it gradually becomes dendritic during the growth. It can also be seen that during the growth, the envelopes reject solute to the extra-dendritic liquid and, therefore, C_e increases. At the early times (i.e., $\tau < 0.37$), this increase is limited to a relatively small distance ahead of the envelopes; therefore, C_e further away from the envelopes is still its initial value (i.e., 0.5 wt. pct.). At the later times (i.e., $\tau > 2.23$), C_e everywhere in the domain has become greater than the initial value. Finally, at $\tau = 5.94$, C_e everywhere has reached the

equilibrium solute concentration $C_l^* = 0.523$; the undercooling has fully vanished and the growth has ended.

5.4.2 Upscaling mesoscopic results

To upscale the mesoscopic simulations results, they were averaged over the volume of the REV. For example, at any time during growth, the solute concentration field in the extra-dendritic liquid was averaged over the volume of the REV to give the value of $\overline{C}_e$ at that time. In Figure 4, the upscaled mesoscopic results are plotted as a function of the non-dimensional time defined as $\tau = tV_{Iv}^2(\Omega_0)/D_l$. Results for a single grain are shown as black curves and for multiple grains with high and low grain density as red and blue curves, respectively. Results for $\Omega_0 = 0.05$ and 0.15 are plotted as solid and dashed curves, respectively.

Plot 5(a) shows the envelope volume fraction g_{env}. Squares in the plot represent the start of the second stage of growth and the definitions of the first and second stages will become clear subsequently, when plot 5(g) is discussed. Plot 5(b) shows the non-dimensional average undercooling in the extra-dendritic liquid Ω_e/Ω_0, where Ω_e was calculated from equation (5-15). Plot 5(c) and plot 5(d), a close-up of 5(c) around $\tau = 5$, show the sphericity, which was calculated using equation (5-3) after calculating S_{env} and S_{sp} as follows: S_{env} was measured directly from the simulated envelope shape, and S_{sp} was calculated from equation (5-5), after computing R_{sp} from an equation that is derived subsequently in connection with plot 5(h). Plot 5(e) shows the non-dimensional primary arm length $l_t/\left[D_l/V_{Iv}(\Omega_0)\right]$, where l_t was measured directly from the simulated envelope shape. Plot 4(f) shows the non-dimensional tip velocity $V_t/V_{Iv}(\Omega_0)$, where V_t was back-calculated from equation (5-12). Plot 5(g) shows the scaled primary arm length l_t^* defined as

$$l_t^* = \frac{l_t}{l_{diff}} \tag{5-16}$$

where l_{diff} is the instantaneous diffusion length ahead of the primary tip, which is defined as

$$l_{diff} = \frac{D_l}{V_t} \tag{5-17}$$

Plot 5(h) shows the non-dimensional sphere radius $R_{sp}/\left[D_l/V_{lv}(\Omega_0)\right]$. The sphere radius R_{sp} was calculated from an integrated form of equation (5-1) which gives an explicit relation for R_{sp} as a function of g_{env}. This integrated form is derived as follows: first, the right-hand side of equation (5-1) was substituted by $S_{sp}w_{sp}$ (see the discussion above equation (5-4)); then, S_{sp} and w_{sp} were substituted from equations (5-5) and (5-6), respectively, to give

$$\frac{1}{g_{env}}\frac{dg_{env}}{dt}dt = \frac{3}{R_{sp}}\frac{dR_{sp}}{dt} \tag{5-18}$$

Next, the definite integrals of both sides of this equation were taken from time zero to time t to give

$$\frac{g_{env}}{g_{env}(t=0)} = \left[\frac{R_{sp}}{R_{sp}(t=0)}\right]^3 \tag{5-19}$$

In this equation, $g_{env}(t=0)$ and $R_{sp}(t=0)$ are the envelope fraction and sphere radius corresponding to the initial spherical seeds. Since the initial seeds have the same size, $g_{env}(t=0)$ and $R_{sp}(t=0)$ can be related as $R_{sp}(t=0) = 2\left[3/(4\pi n)\right]^{1/3} R_f g_{env}^{1/3}(t=0)$, where n is the effective number of grains inside the REV, which is equal to unity for a single grain and two for multiple grains in the BCC arrangement. Substituting this equation into equation (5-19) gives

$$R_{sp} = 2\left(\frac{3}{4\pi n}\right)^{1/3} R_f g_{env}^{1/3} \tag{5-20}$$

Note that this equation has a simple physical meaning: it indicates that, as expected, at any time during growth, the total volume of the spheres (i.e., $n \times 4\pi R_{sp}^3/3$) is equal to the total volume of the envelopes (i.e., $8R_f^3 g_{env}$). In fact, one can write this equation directly from the definition of the sphere. Here, however, this equation was derived using a more formal procedure to show that it is indeed the integrated form of equation (5-1).

Plot 5(i) shows the non-dimensional sphere velocity $w_{sp}/V_{Iv}(\Omega_0)$, where w_{sp} was calculated from equation (5-6). Plot 5(j) shows the non-dimensional average diffusion length around the envelopes $\delta_{env}/\left[D_l/V_{Iv}(\Omega_0)\right]$, where δ_{env} was back-calculated from equation (5-2) by solving this equation for δ_{env}, using the mesoscopic values for all the other quantities. Finally, plot 5(k) shows the comparison between the mesoscopic primary tip velocities and the Ivantsov tip velocities corresponding to Ω_e. Next, the important observations that can be made from these plots are discussed.

From plots 5(a) and 5(b) it can be seen that for a single grain g_{env} and Ω_e remain close to zero and Ω_0, respectively, during the entire growth. This is because for the single grain cases the size of the simulation domain was chosen to be large enough to remain much larger than the envelope size during the entire growth. For the multigrain cases, however, the envelope fraction increase relatively fast initially because Ω_e, which is the driving force for growth, is relatively high; as Ω_e decreases, due to the solute rejection from the envelopes to the extra-dendritic liquid, the rate of increase in g_{env} decreases. Finally, when the undercooling is fully consumed (at τ about 4 and 9 for the high and low grain density cases, respectively) g_{env} ceases to increase further and growth ends.

From plots 5(c) and 5(d) it can be seen that, as expected, the initial value of ψ is equal to unity and as the envelope becomes progressively more dendritic with growth, ψ decreases. For a single grain, this decrease continues until $\tau = 40$. At this time, we stopped the simulations because the diffusion field around the envelope started to interact with the boundaries of the simulation domain. For the multigrain cases, however, after a relatively small initial decrease (of about 0.1 for the high grain density cases and 0.2 for the low grain density cases) ψ stops to decrease further and then remains constant.

From plot 5(f) it can be seen that at an early stage of growth (τ less than two) we have $1 < V_t / V_{Iv}(\Omega_0)$: the mesoscopic tip velocities V_t are greater than the Ivantsov tip velocities corresponding to the initial undercooling $V_{Iv}(\Omega_0)$. This is because of the presence of an initial transient stage in the mesoscopic simulations, where the C_e field is transitioning from the initial value of $C_e = C_0$ (see plot 4(a)) to the quasi-steady values. During this stage, the solutal gradient ahead of the tip and therefore the tip velocity is greater than the quasi-steady values predicted by equation (5-13).

At the end of the initial transient stage (τ about 2), the quasi-steady stage starts. During this stage, V_t for a single grain (i.e. the black curves) remains, as expected, constant, but at a value that is slightly (about 10 percent) lower than the Ivantsov tip velocity corresponding to the initial undercooling Ω_0. This minor underprediction of the tip velocities by the mesoscopic model is of no significant consequence and should not distract; however, for the sake of completeness, the reason for it is explained next. As already discussed in detail by Steinbach et al. (61, 62) and Souhar et al. (69, 78), in the mesoscopic model, the predicted tip velocities depend on a parameter in the model known as the stagnant film thickness δ_f. For the high values of δ_f (i.e. $\delta_f > 3l_{diff}$ (69, 78)) the mesoscopic tip velocity for a single grain will be equal to the Ivantsov tip velocity. However, with such a high value of δ_f, the predicted grain envelope shapes will be unrealistic (compared to the experimentally observed ones (70)). Therefore, to have relatively accurate predictions for *both* V_t and the envelope shape, a compromising intermediate value for δ_f needs to be chosen. As a result of this compromise, the quasi-steady mesoscopic tip velocities are slightly lower than the Ivantsov tip velocities.

The tip velocity V_t for the multiple grain cases starts to rapidly decrease at some intermediate time (about $\tau = 2$ for the high grain density cases and 4.5 for the low grain density cases). This rapid decrease is physically important and indicates that the tips are solutally interacting.

From plot 5(g) it can be seen that l_t^*, which was defined in equation (5-16), for single grain cases increases with time during the entire growth period. For the multigrain cases, however, l_t^* increases with time initially, but, at some intermediate time which is denoted by the squares in the plot, l_t^* starts to decrease with time and eventually reaches zero (since $l_{diff} \to \infty$ as the result of $V_t \to 0$). Therefore, the entire growth period can be divided into two stages: the first stage, where $dl_t^*/dt > 0$, and the second stage, where $dl_t^*/dt \le 0$. Diving the entire growth period into two stages based on the sign of dl_t^* is an important premise that is proposed in this study and will be used in section 5.5, where the constitutive relations are developed.

Variations of l_t^* during these two stages can be understood by following the variations of l_t and V_t, shown in plots 5(d) and 5(e), respectively, and focusing on how the nominator and denominator of equation (5-16) change with time. During the first stage, V_t is relatively high (i.e., greater than $0.8 \times V_{Iv}(\Omega_0)$) and therefore, l_t, which appears in the nominator of equation (5-16), increases relatively fast; this causes l_t^* to increase with time during the first stage. When the second stage starts, V_t has an intermediate value and, more importantly, is decreasing fast. Therefore, unlike the first stage, the increase in l_t is not fast anymore and becomes insignificant compared to the fast increase in l_{diff}, which appears in the denominator of equation (5-16); this causes, l_t^* starts to decrease with time during the second stage.

There is one last interesting point about plot 5(c) that can be discussed now because the first and second stages of growth were defined. In this plot, sphericity for the multiple grain cases becomes constant at about the same time that the second stage of growth starts. This is an important

observation and has inspired the postulate that is the basis of the constitutive relation for the sphericity. This postulate will be introduced in section 5.5.1.

Plot 5(i) shows the time variations of the non-dimensional sphere velocity. From the plot, it can be seen that during the first stage of growth (i.e., the left-hand side of the squares), the multigrain curves collapse on the single grain curves. This indicates that during the first stage of growth, w_{sp} for multigrain and single grain cases can be expected to be predicted by the same relation. When the second stage starts, however, the multigrain curves cease to collapse on the single grain curves, and they start decreasing relatively rapidly. This indicates that w_{sp} during the second stage of growth needs to be predicted from a separate relation.

Comparing the time variations of V_t, shown in plots 5(f), and time variations of w_{sp}, shown in plot 5(i), reveals another interesting observation. Focusing first on the low grain density cases (the blue curves), one can see that at $\tau \approx 8$, V_t is zero: the primary tips have fully stopped. At the same time, however, w_{sp} is still greater than zero: the envelopes are still growing. This indicates that growth continues (at least until $\tau \approx 10$) even after the primary tips stop. A similar trend is observed for the low grain density curves. Growth of an envelope after the primary tips stop is due to the growth of the secondary arms.

In plot 5(k), the mesoscopic primary tip velocities (the thin curves) are compared with the Ivantsov tip velocities, predicted using equation (5-13) with $\Omega_f = \Omega_e$ (the thick curves). Data are shown only for the multigrain cases. One can see from the plot that, as expected (see the discussion below equation (5-15)), setting $\Omega_f = \Omega_e$ in the Ivantsov solution significantly underpredicts the tip velocities.

Finally, this section is ended by summarizing the important observations that can be made from the upscaled mesoscopic results: 1) for the multiple grain cases, the entire growth period can be divided into the first stage and the second stage and these two stages correspond to the positive and negative values of dl_t^*, respectively; 2) for the single grain cases, the growth takes place

entirely in the first stage; 3) during the second stage, the sphericity remains nearly constant; 4) setting $\Omega_f = \Omega_e$ in t

he Ivantsov relation will significantly underpredict the tip velocities.

5.5 Constitutive eelations

5.5.1 Postulates

It is postulated that during the first stage of growth, ψ is a function of l_t/R_{sp} only and (inspired by what was observed in plot 5(c)) during the second stage of growth, ψ is constant:

$$\begin{aligned} dl_t^* > 0 \quad &\rightarrow \quad \psi = \psi\left(\frac{l_t}{R_{sp}}\right) \\ dl_t^* <= 0 \quad &\rightarrow \quad d\psi = 0 \end{aligned} \tag{5-21}$$

During the first stage, w_{sp} is assumed to scale with V_t and the ratio w_{sp}/V_t is postulated to be a function of l_t/R_{sp} only; during the second stage, w_{sp} is assumed to scale with $w_{sp}(t_s)$, where t_s is the time at the start of the second stage, and the ratio $w_{sp}/w_{sp}(t_s)$ is postulated to be a function of the scaled Ivantsov velocity corresponding to Ω_e, $V_{Iv}(\Omega_e)/V_{Iv}\left[\Omega_e(t_s)\right]$, only:

$$\begin{aligned} dl_t^* > 0 \quad &\rightarrow \quad \frac{w_{sp}}{V_t} = \frac{w_{sp}}{V_t}\left(\frac{l_t}{R_{sp}}\right) \\ dl_t^* \le 0 \quad &\rightarrow \quad \frac{w_{sp}}{w_{sp}(t_s)} = \frac{w_{sp}}{w_{sp}(t_s)}\left\{\frac{V_{Iv}(\Omega_e)}{V_{Iv}\left[\Omega_e(t_s)\right]}\right\} \end{aligned} \tag{5-22}$$

Through the entire growth period, Ω_f is assumed to scale with Ω_e, and the ratio Ω_f/Ω_e is assumed to be a function of the scaled length of the free liquid region ahead of the primary tip up to the symmetry line between two adjacent grains $l_l^* = R_f^* - l_t^*$, where $R_f^* = R_f/l_{diff}$:

$$\frac{\Omega_f}{\Omega_e} = \frac{\Omega_f}{\Omega_e}\left(l_l^*\right) \tag{5-23}$$

The envelope diffusion length δ_{env} is assumed to scale with the sphere diffusion length δ_{sp}, and the ratio δ_{env}/δ_{sp} is assumed to be a function of sphericity only:

$$\frac{\delta_{env}}{\delta_{sp}} = \frac{\delta_{env}}{\delta_{sp}}\left(\psi\right) \tag{5-24}$$

5.5.2 Fitting functions

In this section, the upscale mesoscopic results, presented in section 5.4.2, are used to plot the left-hand-side of equations (5-21) to (5-24) as a function of the independent variable on the right-hand-side. The constitutive relations are then developed by curve fitting these plots. In the following figures, mesoscopic results for a single grain are shown as black curves and for multiple grains with high and low grain density as red and blue curves, respectively. Results for $\Omega_0 = 0.05$ and 0.15 are plotted as solid and dashed curves, respectively; the green curves depict our curve fits and the squares show the start of the second stage of growth.

In figure 6, the sphericity ψ is plotted as a function of the ratio of the primary dendrite arm length to the sphere radius l_t/R_{sp}. It can be seen that for a single grain, the mesoscopic simulation results for the two different initial undercoolings Ω_0 collapse onto a single curve. This indicates that the sphericity is indeed a function of l_t/R_{sp} only. The multigrain data in the plot fall on the same curve as the single grain data during the first stage of growth. However, when the second stage starts, the multigrain data start to deviate slightly from the sphericity curve for a single grain. The variation of ψ during this stage are, however, extremely small and are disregarded. The final fit of the sphericity data for both the single grain and the multigrain cases is then given by:

$$dl_t^* > 0 \quad \rightarrow \quad \psi = 1 - \frac{6.34}{6.02 + \frac{8.08}{\left(l_t/R_{sp} - 1\right)^{1.93}}}$$
$$dl_t^* <= 0 \quad \rightarrow \quad d\psi = 0 \tag{5-25}$$

Note that in implementing the first equality in this equation, a tiny number (10^{-10}) needs to be added inside the parentheses in the denominator to avoid division by zero. This equality can be understood as follows. Initially (i.e., $\tau = 0$), the envelope is spherical and l_t/R_{sp} is equal to unity; therefore the denominator on the right-hand side will be large, which will make the sphericity become equal to unity. During growth, as the envelope shape transitions from a spherical to a dendritic, l_t/R_{sp} increases; the second term on the right-hand-side increases, and therefore ψ decreases.

In figure 6(a), w_{sp}/V_t during the first stage of growth is plotted as a function of l_t/R_{sp}. It can be seen that w_{sp}/V_t decreases monotonically as l_t/R_{sp} increases. Since the single grain and multigrain data for the two different initial undercoolings Ω_0 collapse, w_{sp}/V_t during the first stage of growth is indeed a function of l_t/R_{sp} only, and can be fit by $w_{sp}/V_t = 0.80 - 0.78\left[1 - 1/\left(l_t/R_{sp}\right)\right]^{0.85}$. In figure 6(b), $w_{sp}/w_{sp}(t_s)$ is plotted as a function of $V_{Iv}\left(\Omega_e\right)/V_{Iv}\left[\Omega_e\left(t_s\right)\right]$. Single grain data cannot be included in this plot because, as discussed in connection with plot 5(g), for a single grain growth takes place solely at the first stage. One can see that the multigrain data for the two different initial undercoolings Ω_0 collapse onto a single curve. This indicates that $w_{sp}/w_{sp}(\tau_s)$ is indeed a function of $V_{Iv}\left(\Omega_e\right)/V_{Iv}\left[\Omega_e\left(\tau_s\right)\right]$ only. The final fit for $w_{sp}/w_{sp}(\tau_s)$ is then given by $w_{sp}/w_{sp}(t_s) = \left\{V_{Iv}\left(\Omega_e\right)/V_{Iv}\left[\Omega_e\left(t_s\right)\right]\right\}^{0.50}$. Summarizing the fits proposed in plots 6(a) and 6(b), we get

$$dl_t^* > 0 \quad \rightarrow \quad \frac{w_{sp}}{V_t} = 0.80 - 0.78\left(1 - \frac{1}{l_t / R_{sp}}\right)^{0.85}$$
$$dl_t^* \le 0 \quad \rightarrow \quad \frac{w_{sp}}{w_{sp}(t_s)} = \left\{\frac{V_{Iv}(\Omega_e)}{V_{Iv}\left[\Omega_e(t_s)\right]}\right\}^{0.50} \tag{5-26}$$

In Figure 8, Ω_f / Ω_e is plotted as a function of l_l^*; Ω_f was calculated from equation (5-10) using the mesoscopic values for V_t. Data is shown only during the first stage of growth because, as will become clear at the end of this section, in the macroscopic model, calculation of V_t and therefore Ω_f are required during the first stage only. Variations of Ω_f / Ω_e with l_l^* can be best understood by first focusing on the data for the high undercooling low grain density case (i.e., the dashed blue curve). Initially (i.e., at $\tau = 0$), l_l^* has its highest value (about six) and Ω_f is slightly greater than Ω_e, which is equal to Ω_0; this is because, as shown in plot 5(f) and due to the presence of the initial transient stage, V_t is initially greater than $V_{Iv}(\Omega_0)$. During growth, l_t increases and therefore l_l^* decreases. For $l_l^* > 2$, Ω_f / Ω_e remains almost constant because the rate of decrease in Ω_f and Ω_e are almost the same; however, at l_l^* about three, Ω_f / Ω_e starts to increase because the rate of decrease in Ω_e starts to become greater than the rate of decrease in Ω_f. The curves for the other mesoscopic cases behave in a similar fashion and all the curves can be fit by a single curve given by

$$\frac{\Omega_f}{\Omega_e} = \frac{1}{0.97 - \dfrac{0.28}{1 + \left(l_l^* / 1.3\right)^{1.95}}} \tag{5-27}$$

Note that the first term in the denominator of the right-hand-side is chosen to be slightly less than unity so that for a single grain and at the early stages of multigrain growth, where the second term in the denominator is almost zero because l_l^* is high, Ω_f becomes slightly higher than Ω_e ($\Omega_f = 1.031\Omega_e$). Therefore, initially (i.e., at $\tau = 0$), the predicted tip velocity V_t will be higher than $V_{Iv}(\Omega_0)$. This means that the macroscopic model can predict the initial transient effects on the tip

velocity. However, since the Ivantsov solution (i.e., equation (5-13)) does not incorporate these effects, the tip velocities predicted by the macroscopic model during the initial transient stage can only be expected to be approximate.

In Figure 9, δ_{env}/δ_{sp} for the single grain cases is plotted as a function of ψ. It can be seen that as ψ decreases during growth, δ_{env}/δ_{sp} increases monotonically above unity. This indicates that the diffusion length around a complex shaped dendritic envelope is greater than the diffusion length for the sphere. Since the data for the two different initial undercoolings collapse, δ_{env}/δ_{sp} is indeed a function of ψ only. A curve fit to the data for the single grain is given by:

$$\frac{\delta_{env}}{\delta_{sp}} = 1 + 1.3\left(1-\psi\right)^{2.5} \tag{5-28}$$

In summary, the macroscopic model consists of equations (5-1) to (5-7), (5-12) to (5-17), and (5-25) to (5-28). It requires two inputs: the initial undercooling Ω_0 and the final grain radius R_f. Also, note that l_t and V_t appear only in the first relation of equations (5-25) and (5-26), respectively. Therefore, the model needs to calculate V_t during the first stage only.

5.6 Comparing macroscopic and mesoscopic results

In this section, the constitutive relations are verified by comparing the predictions of the macroscopic model against the upscaled mesoscopic results. The comparisons are first made for the isothermal mesoscopic cases, presented in section 5.4.2, and used in section 5.5 to develop the constitutive relations. Next, to provide further confidence in the constitutive relations, comparisons are made against new upscaled mesoscopic results.

5.6.1 Isothermal cases

Figures 10 through 13 show the comparisons between the predictions of the macroscopic model for different quantities (the blue curves) with the corresponding upscaled mesoscopic results (the

red curves) for the four isothermal cases. Figures 10 and 11 show the comparisons for the low grain density cases with the low and high undercoolings, respectively and figures 12 and 13 show the similar comparisons for the high grain density cases. For all the four cases, the overall agreements between the macroscopic predictions and the upscaled mesoscopic results are good and, as we discuss next, cannot realistically be expected to be much better. The minor difference between the two can be attributed to the difference between mesoscopic and macroscopic values of the tip velocities V_t during the initial transient stage.

In plots 10(e) to 13(e) the tip velocities predicted by the macroscopic model are compared with the mesoscopic tip velocities. Note that, as discussed at the end of section 5.5, in the macroscopic model the tip velocities need to be predicted only during the first stage. Plotting the tip velocities during the second stage here is only for the sake of completeness. It can be seen that, during the entire growth period, the predicted tip velocities agree reasonably well with the mesoscopic tip velocities. Contrasting this agreement with the vast difference that was observed in plot 5(k) between the mesoscopic tip velocities and the Ivantsov velocities corresponding to Ω_e, one can easily acknowledge that the tip velocities predicted by our model (i.e., the Ivantsov velocities corresponding to Ω_f) are, as expected, significantly more accurate (when compared against the mesoscopic tip velocities) than the Ivantsov velocities corresponding to Ω_e.

The minor difference between the macroscopic and mesoscopic tip velocities is attributed to the presence of the initial transient stage in the mesoscopic simulations. Recall that the Ivantsov solution (i.e. equation (5-13)) does not incorporate the initial transient effects and a similar relation that incorporates these effects does not exist in the literature. Therefore, the agreement between the macroscopic and mesoscopic tip velocities cannot realistically be expected to be much better.

5.6.2 Recalescence cases

To further verify the constitutive relations, new mesoscopic simulations were performed and the predictions of the macroscopic model were compared with the upscaled mesoscopic results. These new cases are inspired by the experiments of Rappaz and Thevoz (72), which involve solidification of Al-7 wt. pct. Si in a small unit cell, with uniform temperature, under external cooling. These

cases are called the recalescence cases because, as is shown below, a temperature recalescence was observed in the cooling curves. To simulate these cases with the macroscopic model, this model needs to be supplemented by three additional equations that are discussed next.

The equation for the energy conservation reads

$$c_p \frac{\partial T}{\partial t} = L_f \frac{\partial g_s}{\partial t} + \dot{q} \tag{5-29}$$

where c_p, L_f, and $\dot{q}$ are the specific heat capacity, latent heat, and heat extraction rate, respectively. To predict the solid fractions, the solute concentration in the inter-dendritic liquid (i.e., the liquid inside the envelopes) was first calculated from (79):

$$g_l \frac{\partial \bar{C}_d}{\partial t} = (1-k_0)\bar{C}_d \frac{\partial g_s}{\partial t} - \frac{\partial}{\partial t}\left[g_e\left(\bar{C}_e - \bar{C}_d\right)\right] \tag{5-30}$$

where $g_l = 1 - g_s$ is the liquid fraction. Then, since the inter-dendritic liquid is not undercooled, the solid fraction can be calculated by equating the inter-dendritic liquid solute concentration with the equilibrium solute concentration C_l^*:

$$\text{For } T < T_{liq}\left(\bar{C}_e\right) - \Delta T_{nuc} : \ \bar{C}_d = C_l^* \tag{5-31}$$

where ΔT_{nuc} is the nucleation undercooling and C_l^* is calculated from the liquidus line of the phase diagram

$$C_l^* = \frac{T - T_f}{m_l} \tag{5-32}$$

where m_l is the slope of the liquidus line and T_f is the melting point of the pure material. Note that equation (5-31) assumes that nucleation occurs instantaneously at the nucleation temperature.

Similar to the isothermal cases, the recalescence cases correspond to the growth of multiple grains, in a BCC arrangement, with low/intermediate/high grain densities (i.e., $R_f = 0.8/1.6/2.4$ mm). In the simulations, the properties were taken from Rappaz and Thevoz (72); the initial temperature was set equal to the liquidus temperature (i.e., no initial undercooling), and the nucleation undercooling was set to zero.

Figures (14) through (17) show the comparisons between the macroscopic predictions of the different quantities (the blue curves) with the corresponding upscaled mesoscopic results (the red curves) for the recalescence cases with low/intermediate/high grain densities. From the plots it can be seen that the overall agreement between the two is good. For example, the recalescence observed in the mesoscopic simulations is predicted to within better than 0.5 K accuracy and the mesoscopic and macroscopic solid fractions are in an almost excellent agreement. Note that the existence of a minor difference between the macroscopic and mesoscopic temperatures while the solid fractions are in excellent agreement, shows extremely high sensitivity of the system. Predicting temperatures with accuracy of 0.5 K for such a sensitive system is a remarkable achievement of the new constitutive relations.

Finally, it is useful to mention that, for the recalescence cases, the macroscopic and mesoscopic values of V_t are initially in an excellent agreement. This is because these cases do not have an initial transient stage as they start with undercooling zero. This also further supports the argument that we had at the end of section 5.6.1, where we attributed the minor difference between macroscopic and mesoscopic values of V_t to the presence of an initial transient stage.

5.7 Conclusions

A previously developed mesoscopic envelope model was used to perform three-dimensional simulations of equiaxed dendritic growth on a spatial scale that corresponds to a REV, which is used in developing volume-averaged macroscopic models. The first set of mesoscopic simulations were performed for isothermal growth at a large range of initial undercoolings and grain densities (including a single grain). The results were upscaled by averaging them over the REV. The upscaled results were examined in detail. It was found that the entire growth period can be divided

into two stages based on the sign of the time derivative of the scaled primary arm length. During the first stage, the envelope growth is mainly due to the growth of the primary arms, while during the second stage it is mainly due to the growth of the secondary arms. In addition, during the second stage, the sphericity remains nearly constant. It was also found that using the average undercooling in the extra-dendritic liquid in the Ivantsov solution significantly underpredicts the tip velocities.

For the first time in the field of solidification, the upscaled mesoscopic results were used to develop constitutive relations for macroscopic models of equiaxed solidification. Relations were proposed for the envelope sphericity, average growth velocity, far-field undercooling that needs to be used in the Ivantsov solution to accurately predict the primary tip velocities, and for the average diffusion length around the envelopes.

The constitutive relations were verified by comparing the predictions of the macroscopic model with the upscaled mesoscopic results for the isothermal cases and also for the new mesoscopic cases. These new cases involve external cooling and a recalescence in the cooling curves. For all the cases, the predicted macroscopic quantities were found to be in good agreement with the corresponding upscaled mesoscopic results. The minor difference between the two was attributed to a minor difference in the macroscopic and mesoscopic values of the primary tip velocity, and that was attributed to the presence of an initial transient stage in the mesoscopic simulations.

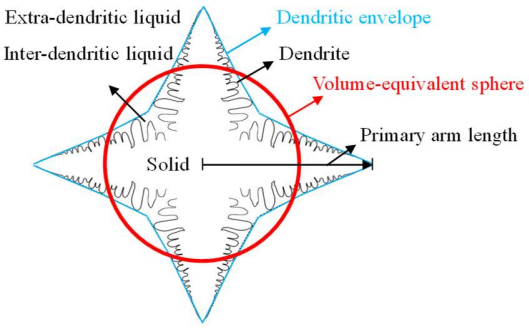

(a)

Figure 5-1. Two-dimensional schematic of a single equiaxed dendrite growing into an essentially infinite medium; the dendritic envelope and volume-equivalent sphere; and regions of solid (s), inter-dendritic liquid (d), and extra-dendritic liquid (e).

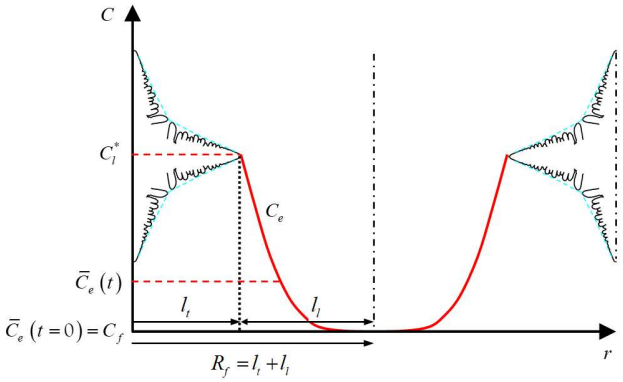

(a)

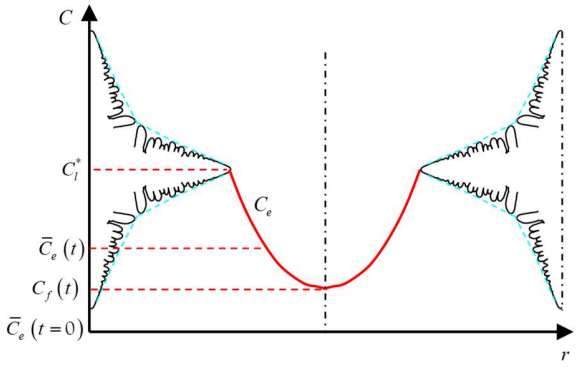

(b)

Figure 5-2. Schematics of the extra-dendritic liquid solute concentration profiles ahead of the primary tips of two adjacent dendrites, at a time instance in the (a) non-interacting stage and (b) interacting stage.

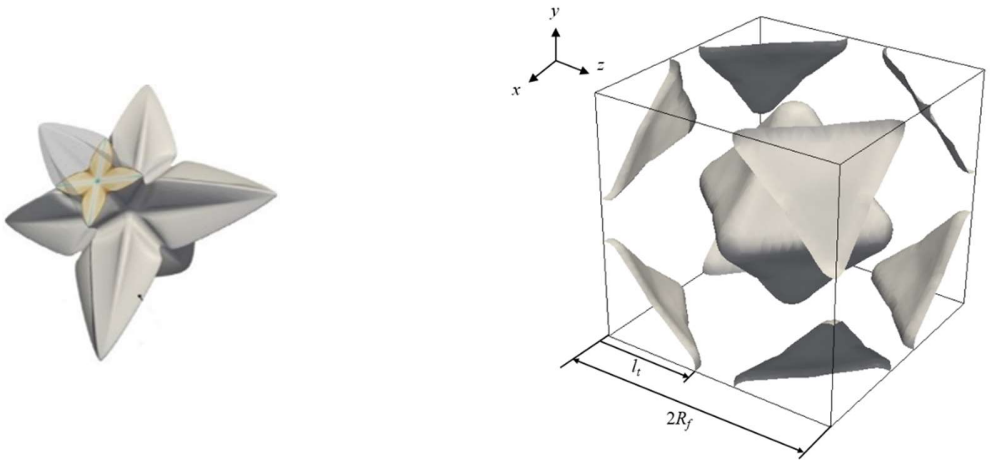

(a) (b)

Figure 5-3. Mesoscopic grain envelopes for (a) a single grain and (b) multiple grains in the BCC arrangement with the primary arms growing along the *x*, *y*, and *z* axes.

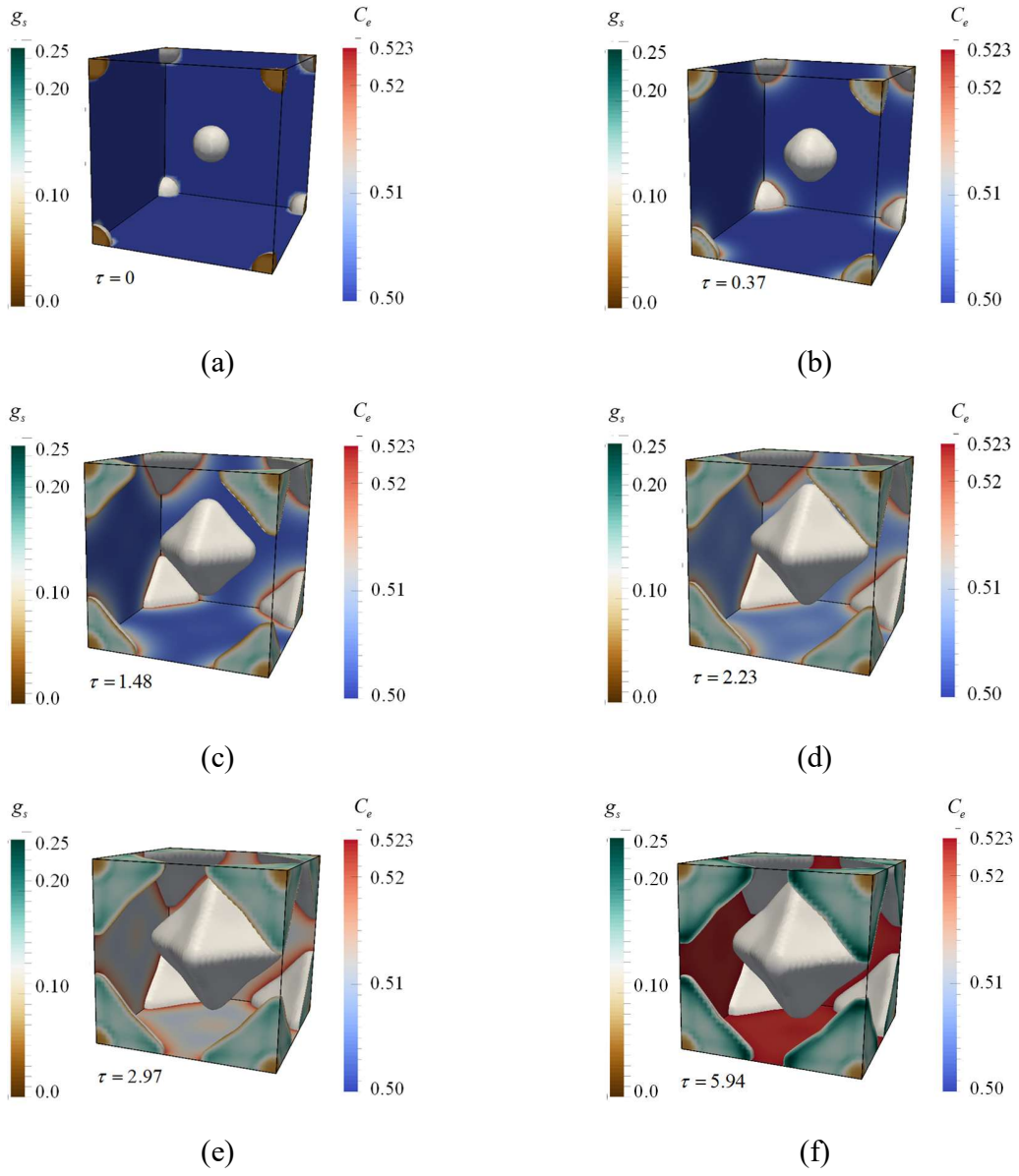

Figure 5-4. Mesoscopic simulation results showing solid fraction g_s (plotted in the interior of the envelopes) and solute concentration in the extra-dendritic liquid C_e (plotted in the exterior of the envelopes) at different non-dimensional times $\tau = tV_{Iv}^2(\Omega_0)/D_l$: (a) τ=0, (b) 0.37, (c) 1.48, (d) 2.23, (e) 2.97, and (f) 5.94. This simulations is for the isothermal case with low undercooling (Ω_0 = 0.05) and high grain density ($R_f/\left[D_l/V_{Iv}(\Omega_0)\right]$= 4.03).

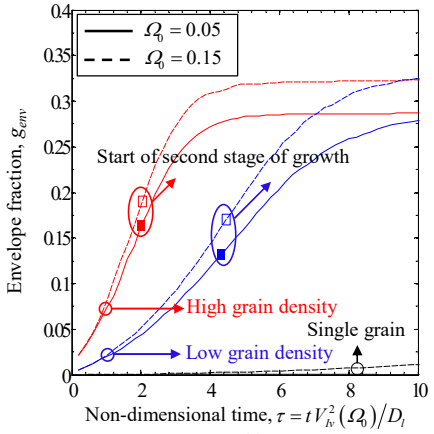

(a)

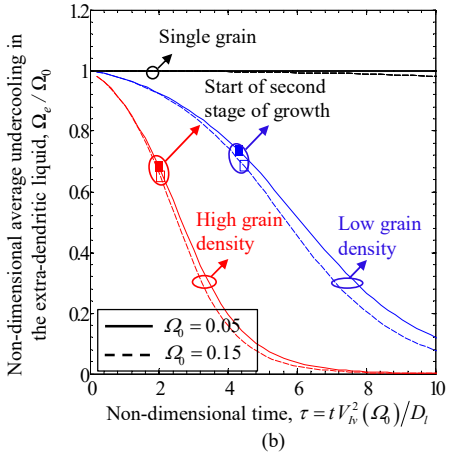

(b)

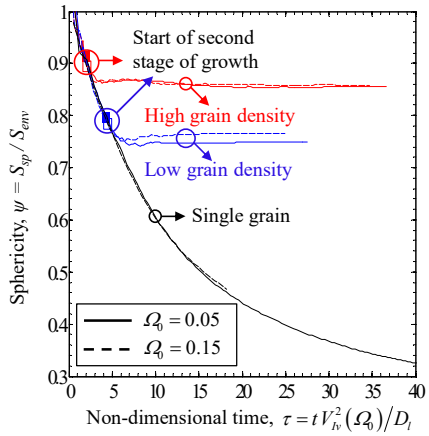

(c)

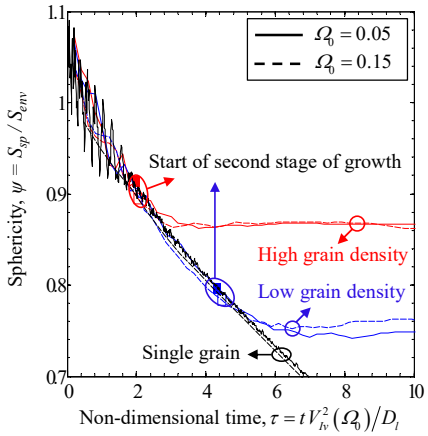

(d)

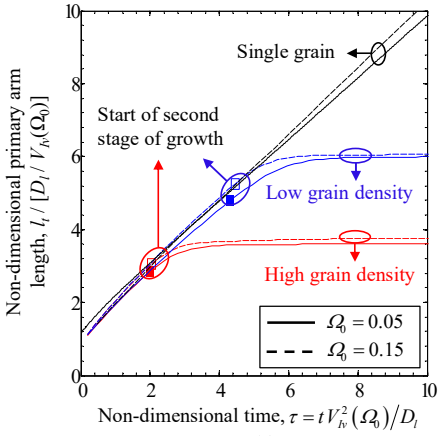

(e)

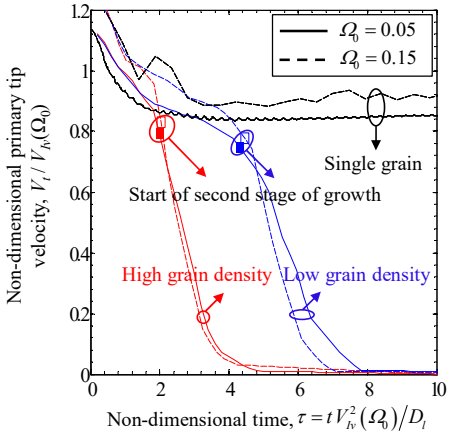

(f)

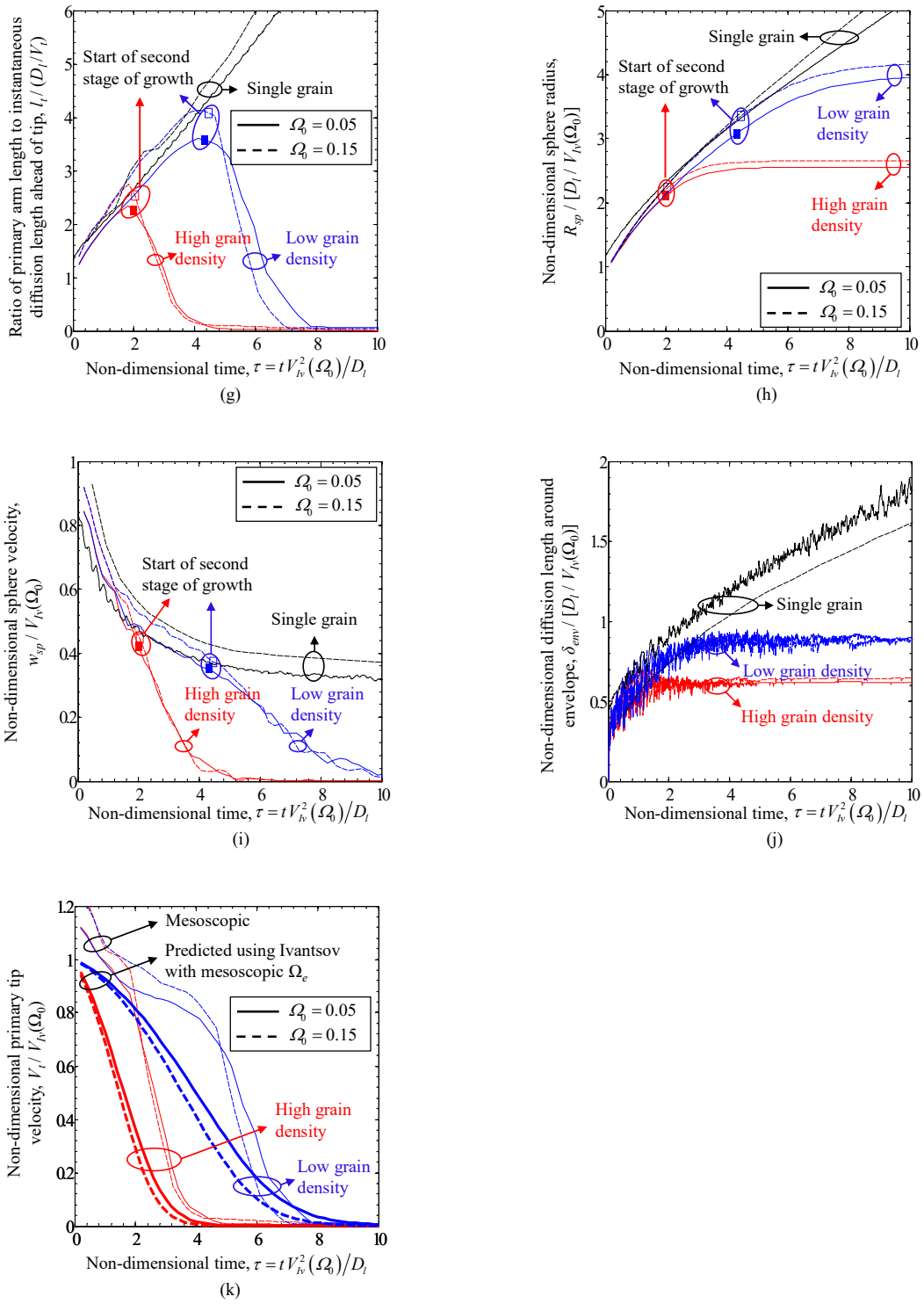

Figure 5-5. (a-j) Upscaled mesoscopic results plotted as a function of non-dimensional time and (k) comparison between the mesoscopic primary tip velocities and the Ivantsov primary tip

velocities corresponding to the average undercooling in the extra-dendritic liquid. High and low grain density cases correspond to $R_f/\left[D_l/V_{hv}(\Omega_0)\right]$= 4.03 and 6.31, respectively.

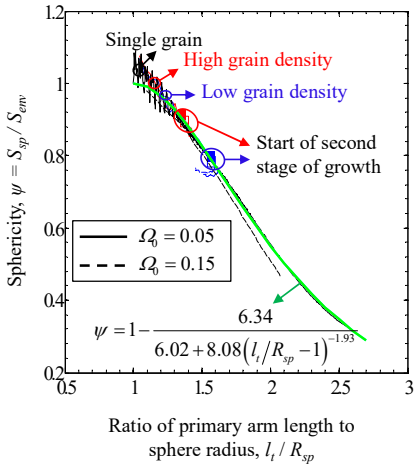

Figure 5-6. The envelope sphericity as a function of the ratio of the primary arm length to sphere radius. The green curve represents our curve fit.

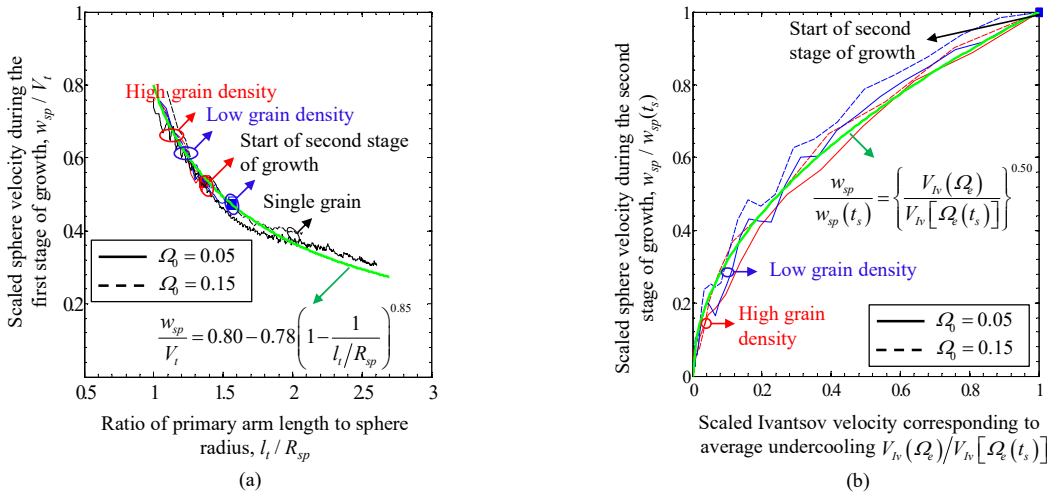

Figure 5-7. Scaled sphere growth velocity during (a) the first stage of growth as a function of the ratio of primary arm length to sphere radius, and during (b) the second stage of growth as a function of scaled Ivantsov velocity corresponding to the average undercooling in the extra-dendritic liquid. The green curves represent our curve fits.

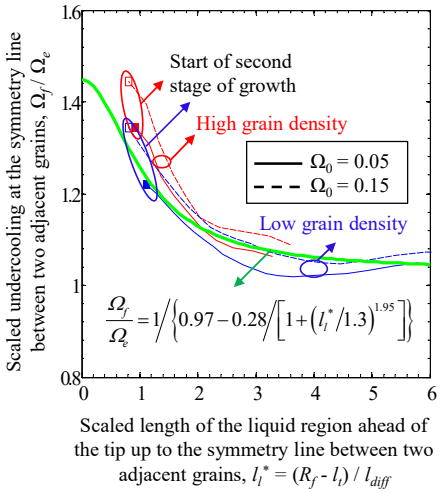

Figure 5-8. The scaled far field undercooling as a function of the scaled length of the liquid region ahead of the tip up to the symmetry line between two adjacent grains. The green curve represents our curve fit.

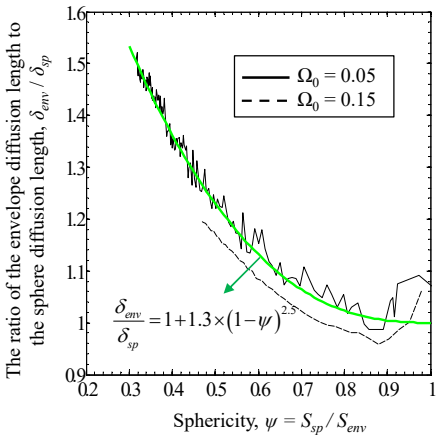

Figure 5-9. The ratio of the envelope diffusion length to the sphere diffusion length as a function of the envelope sphericity for a single grain at two different initial undercoolings. The green curve represents our curve fit.

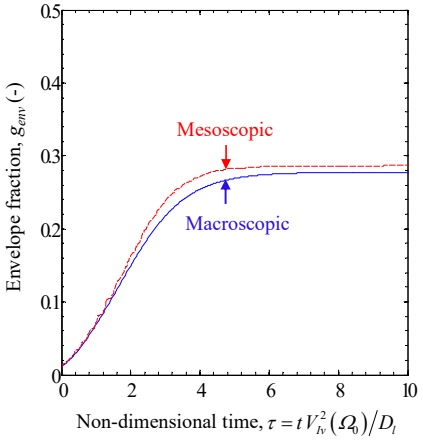

(a)

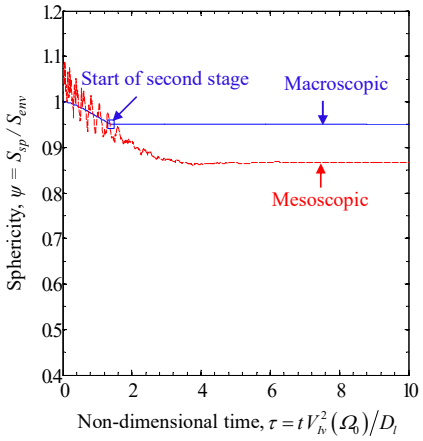

(b)

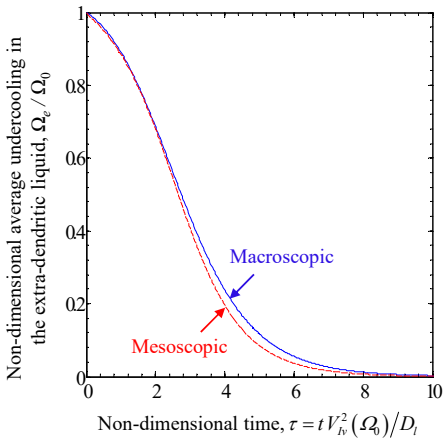

(c)

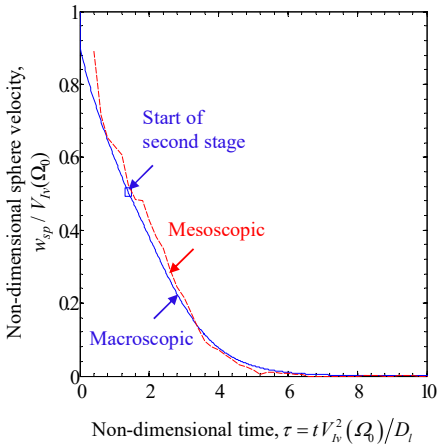

(d)

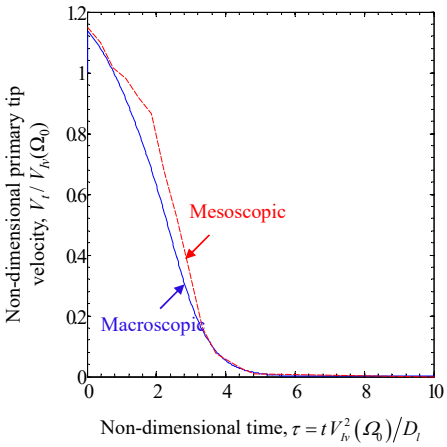

(e)

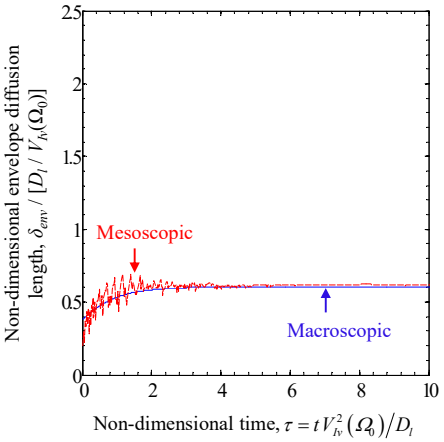

(f)

Figure 5-10. Comparison between the mesoscopic and macroscopic quantities plotted as a funciton of non-dimensional time. This comparison is for the isothermal case with high grain density and low undercooling: $R_f/\left[D_l/V_{Iv}\left(\Omega_0\right)\right]=4.03$ and $\Omega_0=0.05$.

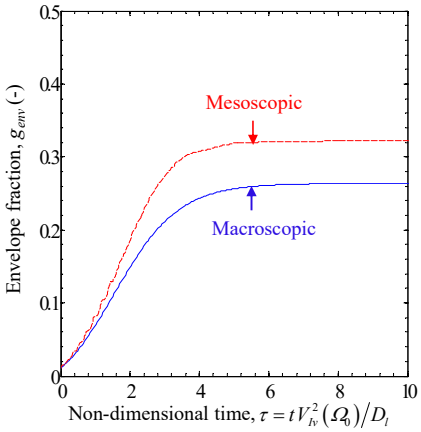

(a)

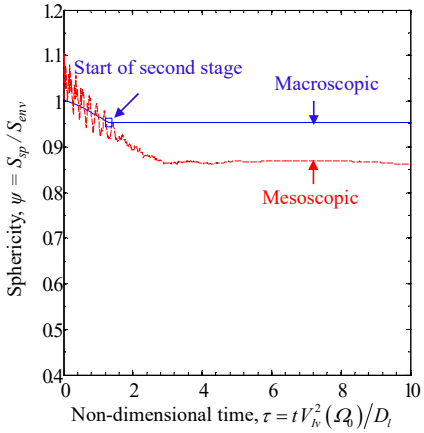

(b)

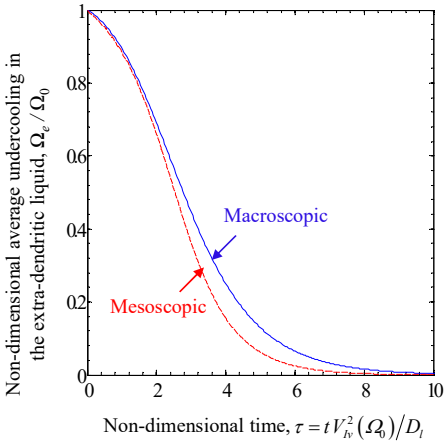

(c)

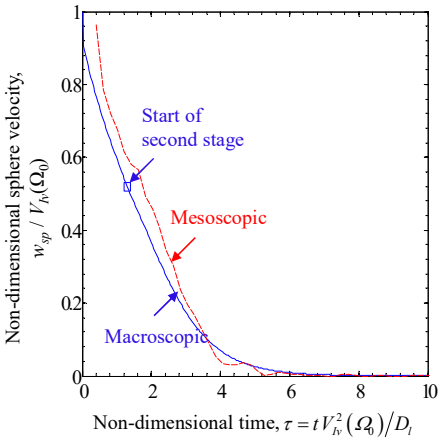

(d)

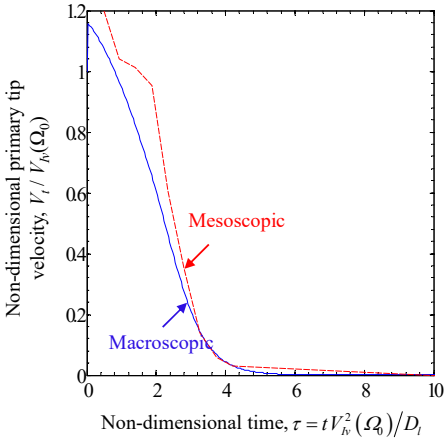

(e)

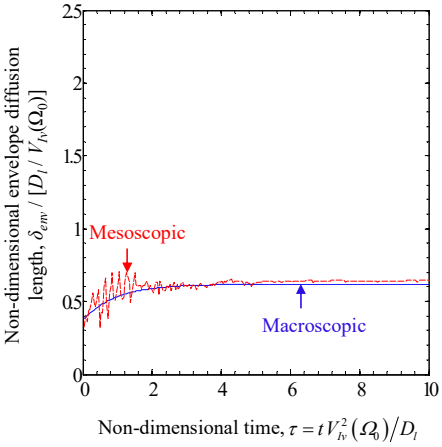

(f)

Figure 5-11. Comparison between the mesoscopic and macroscopic quantities plotted as a funciton of non-dimensional time. This comparison is for the isothermal case with high grain density and high undercooling: $R_f/\left[D_l/V_{Iv}\left(\Omega_0\right)\right]=4.03$ and $\Omega_0=0.15$.

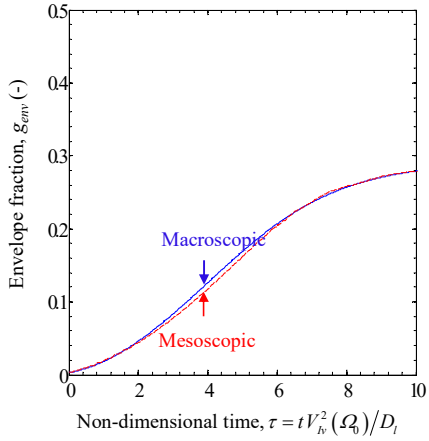

(a)

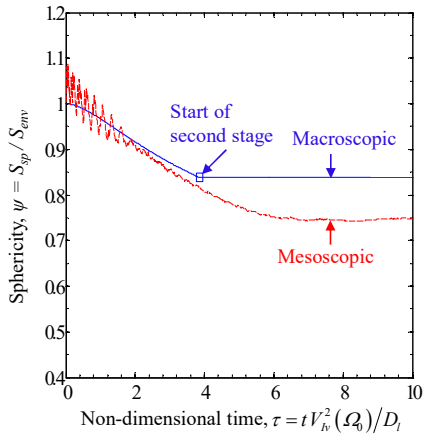

(b)

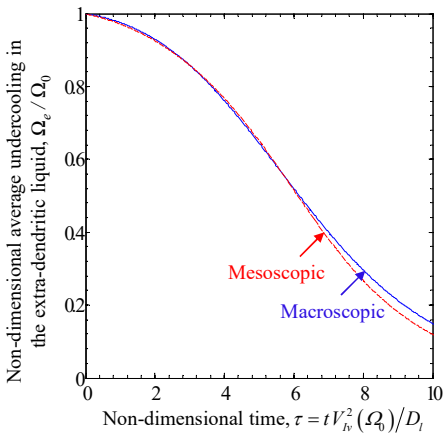

(c)

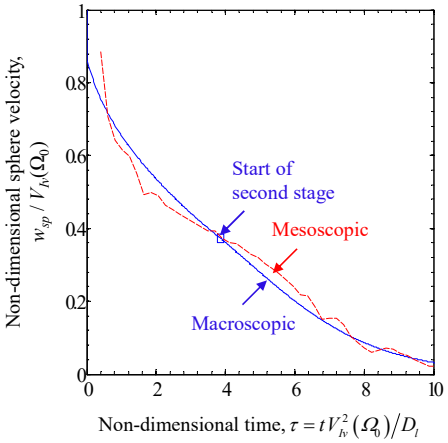

(d)

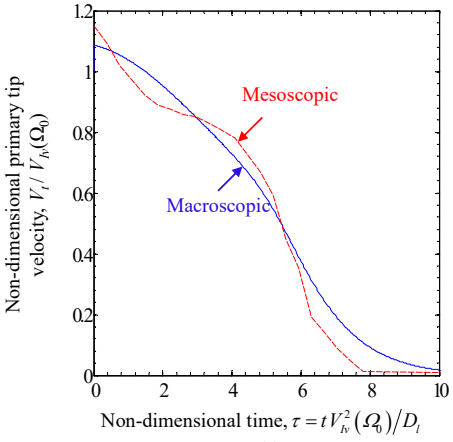

(e)

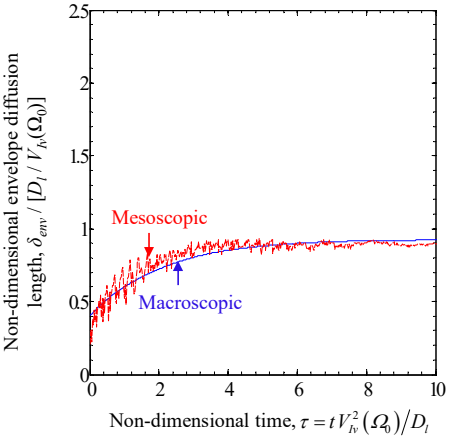

(f)

Figure 5-12. Comparison between the mesoscopic and macroscopic quantities plotted as a funciton of non-dimensional time. This comparison is for the isothermal case with low grain density and low undercooling: $R_f / \left[D_l / V_{lv} \left(\Omega_0 \right) \right] = 6.31$ and $\Omega_0 = 0.05$.

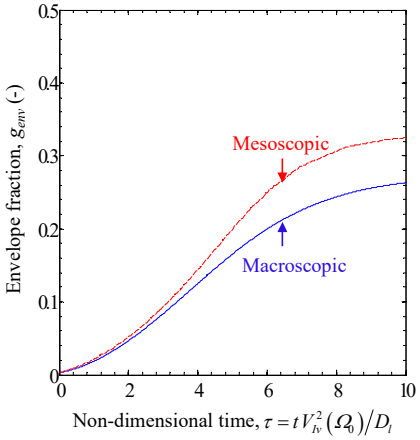

(a)

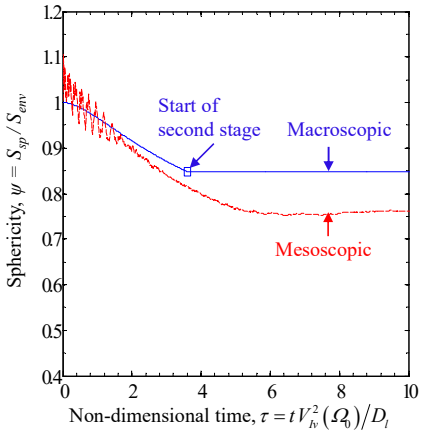

(b)

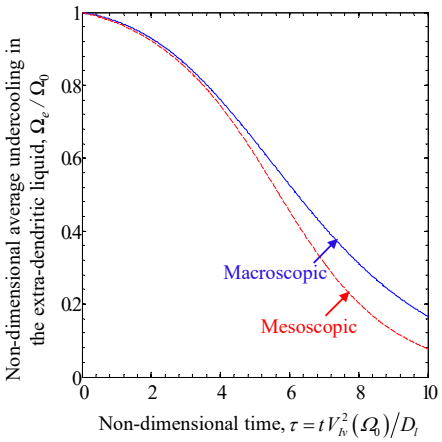

(c)

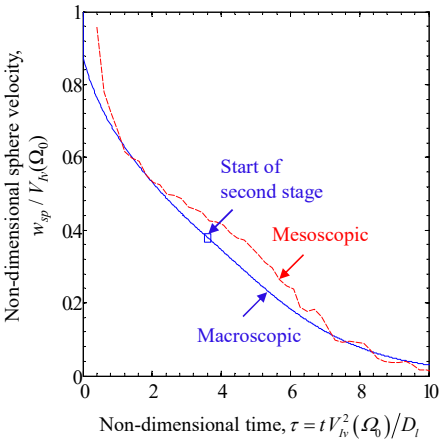

(d)

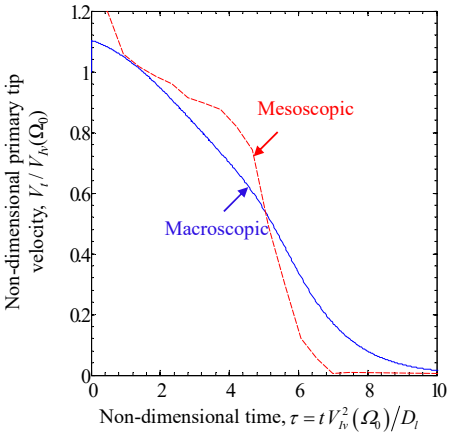

(e)

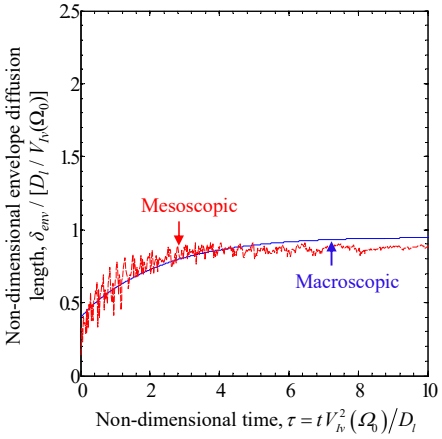

(f)

Figure 5-13. Comparison between the mesoscopic and quantities plotted as a funciton of non-dimensional time. This comparison is for the isothermal case with low grain density and high undercooling: $R_f/\left[D_l/V_{lv}\left(\Omega_0\right)\right]=6.31$ and $\Omega_0=0.15$.

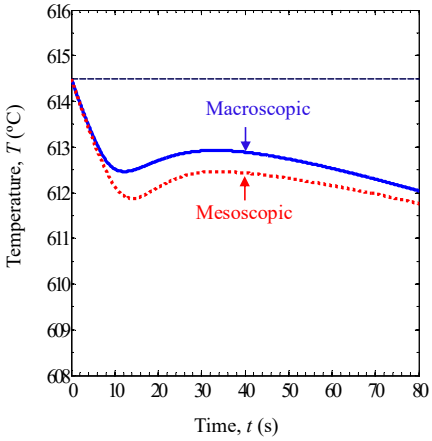

(a)

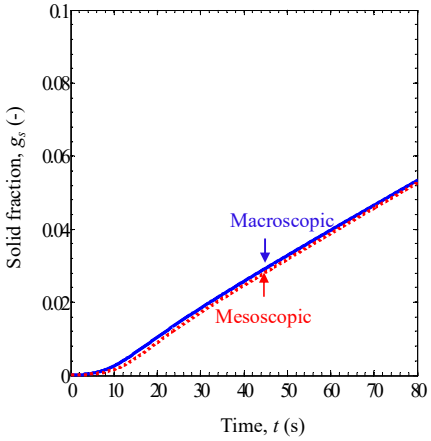

(b)

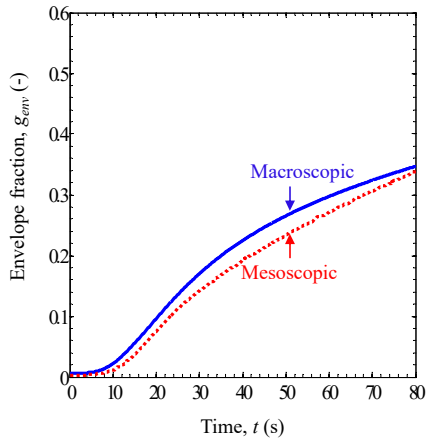

(c)

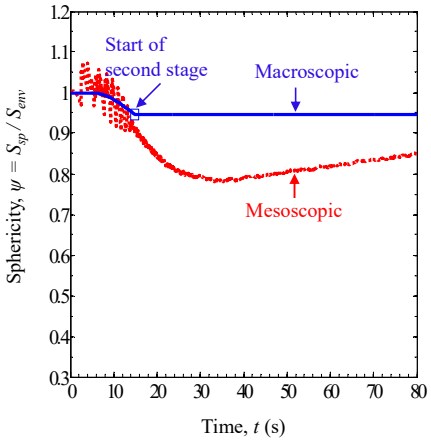

(d)

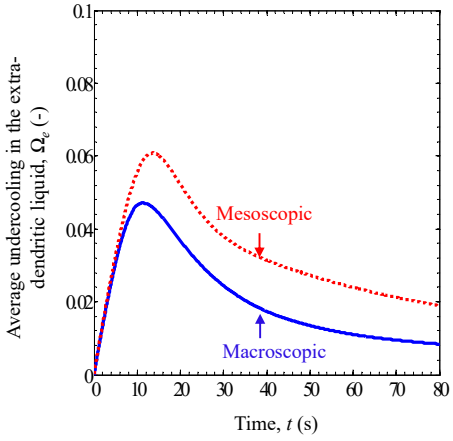

(e)

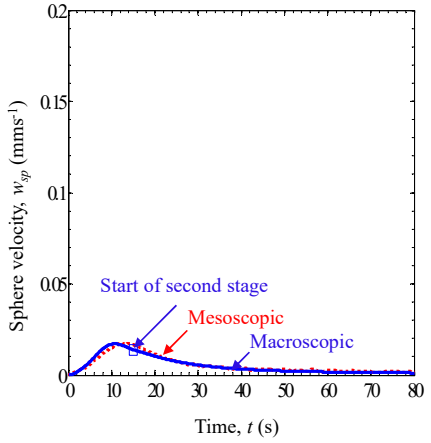

(f)

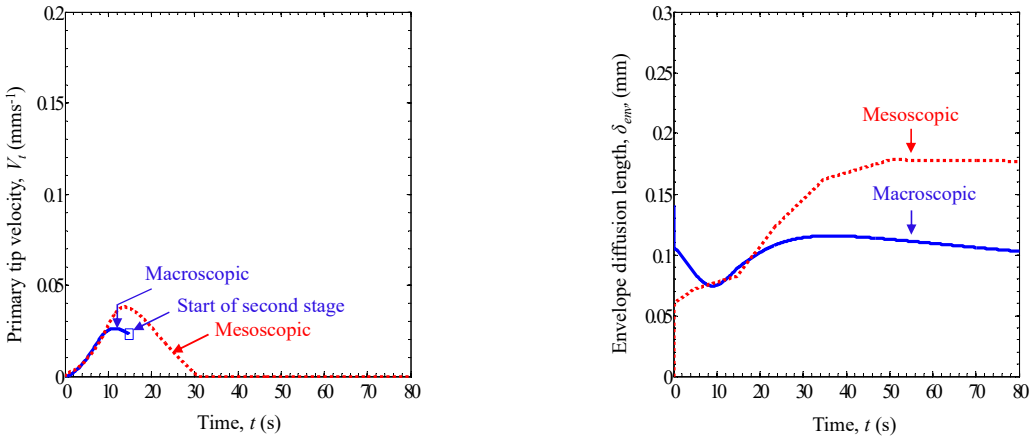

Figure 5-14. Comparison between the mesoscopic and macroscopic quantities plotted as a function of time. This comparison is for the recalescence case with high grain density: $R_f = 0.8\,mm$.

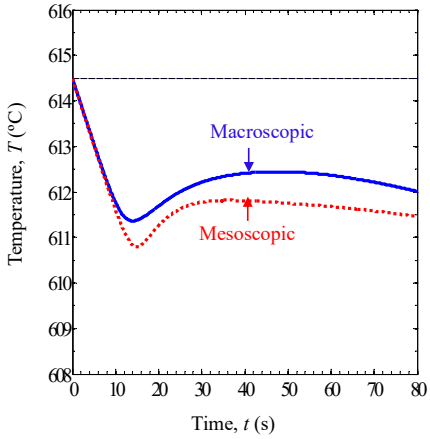

(a)

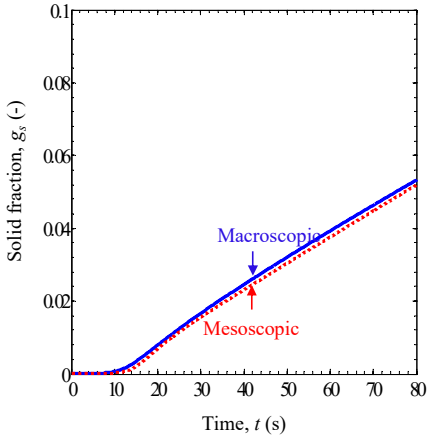

(b)

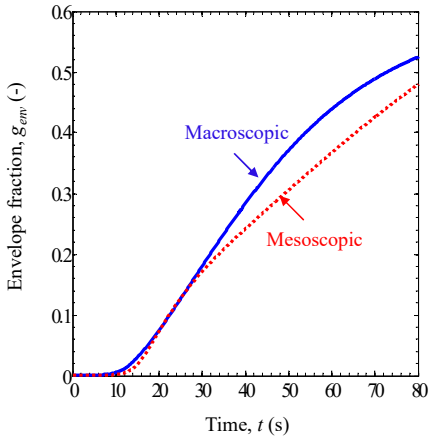

(c)

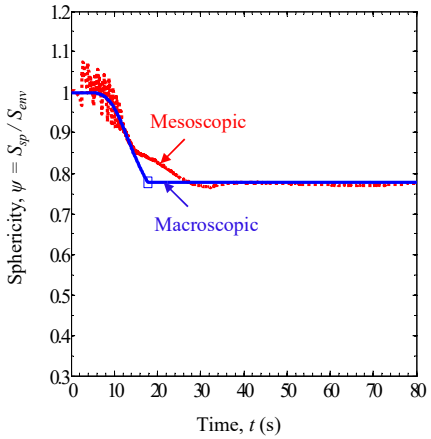

(d)

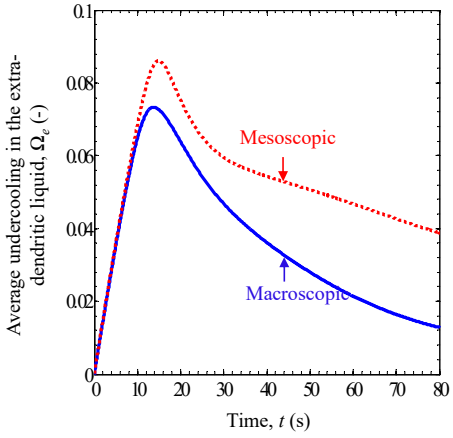

(e)

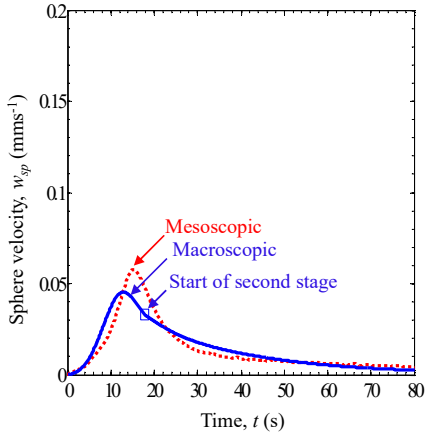

(f)

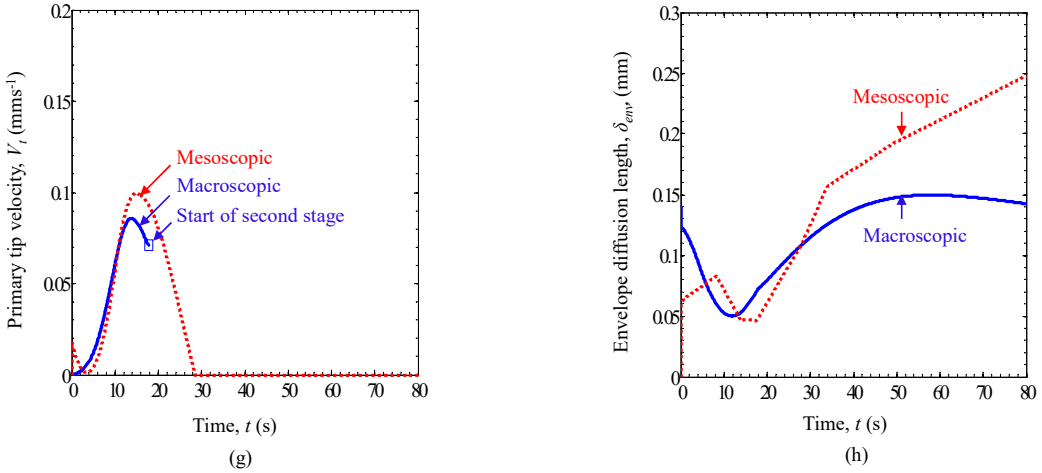

Figure 5-15. Comparison between the mesoscopic and macroscopic quantities plotted as a function of time. This comparison is for the recalescence case with intermediate grain density: $R_f = 1.6\ mm$.

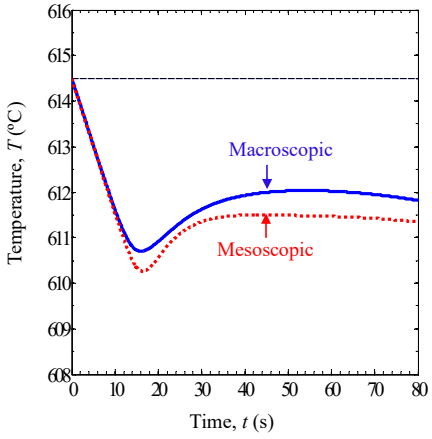

(a)

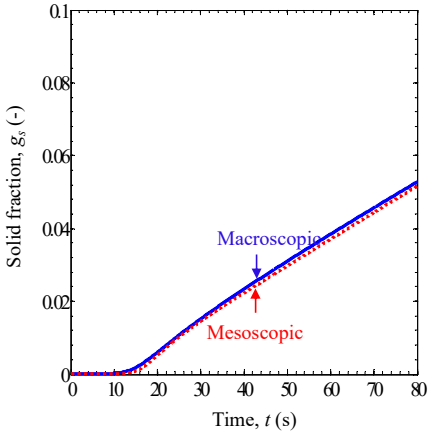

(b)

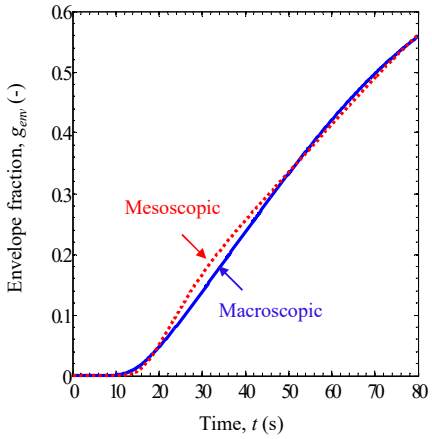

(c)

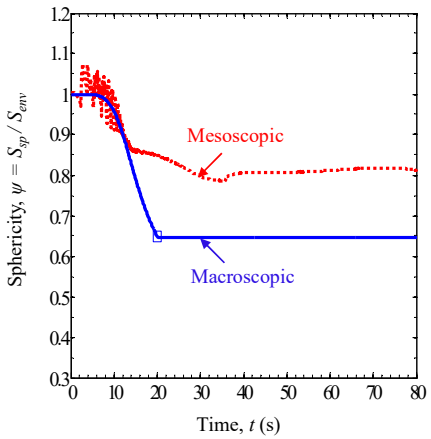

(d)

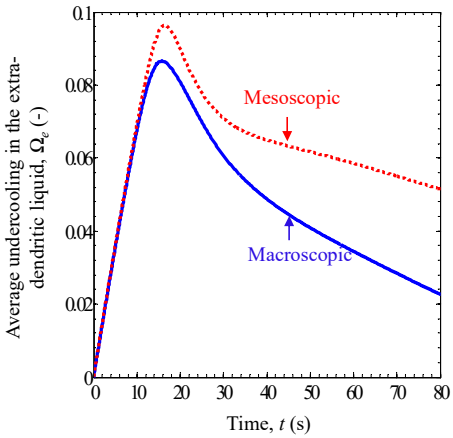

(e)

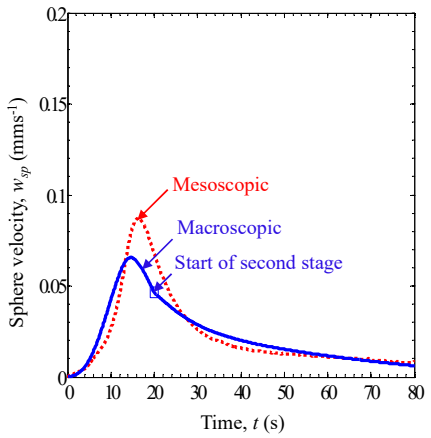

(f)

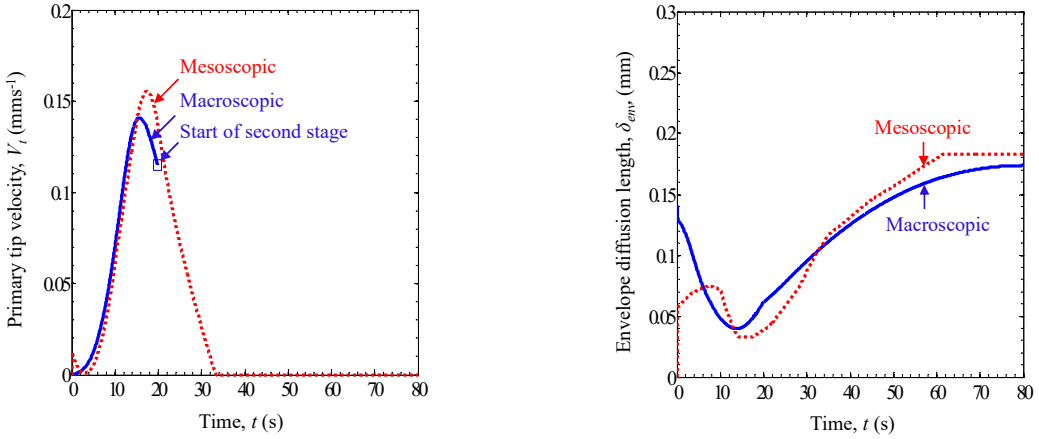

Figure 5-16. Comparison between the mesoscopic and macroscopic quantities plotted as a function of time. This comparison is for the recalescence case with low grain density: $R_f = 2.4\,mm$.

Chapter 6: Conclusions and future work

6.1 Conclusions

In this thesis, a three-phase model for simultaneous prediction of macrosegregation and CET was developed. This model accounts for numerous phenomena such as grain nucleation and liquid undercooling both behind and ahead of the columnar fronts. This model was used to develop a less complex, two-phase model for macrosegregation in the presence of primary tip undercooling. These models were used to perform columnar solidification simulations of a numerical solidification benchmark problem and it was found that the predictions of the two models are nearly identical. It was also found that the dendrite tip selection parameter σ^* plays a key role in these models. With the realistic value σ^* (i.e., $\sigma^* = 0.02$) these models account for columnar dendrite tip undercooling, but as its value is increased in the simulations, predictions of these models converge to predictions of a model that neglects undercooling. The three-phase model was used to perform CET simulations of the numerical solidification benchmark problem in the presence of melt convection. It was found that accounting for nucleation of stationary equiaxed grains does not change the overall macrosegregation pattern nor the form of channel segregates. Finally, for the first time in the field of solidification, accurate constitutive relations for macroscale solidification models were developed that are based on a formal mesoscale analysis on the scale of a representative elementary volume. This upscaling enabled us to present relations that incorporate changes in the shape of grains and solute diffusion conditions around them during growth. The models and constitutive relations we developed can now be used to predict critical phenomena such as macrosegregation, channel segregates, and CET in castings.

6.2 Future work

The research presented in this thesis can be continued in different directions. For example, the three-phase model for CET and macrosegregation assumes that the equiaxed grains are stationary

and that the inter-dendritic and extra-dendritic liquids have the same velocity. These assumptions can be relaxed in future works. As another example, this model and also the truncated-Scheil-type model can be extended for multicomponent alloys.

Another interesting area of future work is to validate the three-phase and truncated-Scheil-type models against experimental results. For example, these models can be used to perform simulations of the solidification benchmark *experiments* involving columnar solidification of tin-lead (33, 80) and gallium-indium alloys (81, 82). It would be very interesting to perform these simulations in 3D and compare the predicted shaper of channel segregates and the CET position with the experimental observations.

The work about the constitutive relations developed in chapter 5 can also be extended by, for example, comparing the predictions of the macroscopic model with the upscaled mesoscopic results for multiple grains in a *random arrangement*. For this arrangement, calculating the final grain radius R_f will be a key factor in macroscopic simulations. This can be achieved using methods such as grain count or linear intercept that are commonly used in microstructure analysis (83). Extension of the mesoscopic model for multicomponent alloys and incorporating melt flow in the model are also of great interest.

References

1. Spittle J. Columnar to equiaxed grain transition in as solidified alloys. International Materials Reviews. 2006;51(4):247-69.
2. Wang CY, Beckermann C. Equiaxed dendritic solidification with convection: Part I. Multiscale/multiphase modeling. Metallurgical and materials transactions A. 1996;27(9):2754-64.
3. Martorano MA, Beckermann C, Gandin C-A. A solutal interaction mechanism for the columnar-to-equiaxed transition in alloy solidification. Metallurgical and Materials Transactions A. 2003;34(8):1657-74.
4. Bozorgzad A. Consistent distribution of air voids and asphalt and random orientation of aggregates by flipping specimens during gyratory compaction process. Construction and Building Materials. 2017;132:376-82.
5. Bozorgzad A, Kazemi S-F, Nejad FM. Evaporation-induced moisture damage of asphalt mixtures: Microscale model and laboratory validation. Construction and Building Materials. 2018;171:697-707.
6. Bozorgzad A, Kim Y, Lee HD. Determining the Optimum Content and Stirring Time of Emerging Dry Polymer for Asphalt Using Rotational Viscometer, Dynamic Shear Rheometer, and Atomic Force Microscopy. Advances in Civil Engineering Materials. 2018;7(1):33-45.
7. Bozorgzad A CB, Sampath A, Kim Y, Lee HD Impacts of WMA Additives on Viscosity and Cracking of Asphalt Binder. Advances in Civil Engineering Materials. 2018;7(1):496–506.
8. Ni J, Beckermann C. A volume-averaged two-phase model for transport phenomena during solidification. Metallurgical and Materials Transactions B. 1991;22(3):349-61.
9. Wang C, Beckermann C. Single-vs dual-scale volume averaging for heterogeneous multiphase systems. International journal of multiphase flow. 1993;19(2):397-407.
10. Wang C, Beckermann C. A multiphase solute diffusion model for dendritic alloy solidification. Metallurgical and Materials Transactions A. 1993;24(12):2787-802.
11. Wu M, Fjeld A, Ludwig A. Modelling mixed columnar-equiaxed solidification with melt convection and grain sedimentation–Part I: Model description. Computational Materials Science. 2010;50(1):32-42.

12. Wu M, Ludwig A. Modeling equiaxed solidification with melt convection and grain sedimentation—I: Model description. Acta Materialia. 2009;57(19):5621-31.
13. Wu M, Ludwig A, Fjeld A. Modelling mixed columnar-equiaxed solidification with melt convection and grain sedimentation–Part II: Illustrative modelling results and parameter studies. Computational Materials Science. 2010;50(1):43-58.
14. Martorano MA, Aguiar DT, Arango JMR. Multigrain and Multiphase Mathematical Model for Equiaxed Solidification. Metallurgical and Materials Transactions A. 2015;46(1):377-95.
15. Dantzig J, Rappaz M. Solidification. CRC Press, EPFL; 2009.
16. Hunt J. Steady state columnar and equiaxed growth of dendrites and eutectic. Materials science and engineering. 1984;65(1):75-83.
17. Biscuola V, Martorano M. Mechanical blocking mechanism for the columnar to equiaxed transition. Metallurgical and Materials Transactions A. 2008;39(12):2885-95.
18. Gandin C-A. From constrained to unconstrained growth during directional solidification. Acta Materialia. 2000;48(10):2483-501.
19. Browne DJ. A new equiaxed solidification predictor from a model of columnar growth. ISIJ international. 2005;45(1):37-44.
20. Mcfadden S, Browne DJ, Gandin C-A. A comparison of columnar-to-equiaxed transition prediction methods using simulation of the growing columnar front. Metallurgical and Materials Transactions A. 2009;40(3):662-72.
21. Peres M, Siqueira C, Garcia A. Macrostructural and microstructural development in Al–Si alloys directionally solidified under unsteady-state conditions. Journal of Alloys and Compounds. 2004;381(1):168-81.
22. Wu M, Ludwig A. Using a three-phase deterministic model for the columnar-to-equiaxed transition. Metallurgical and Materials Transactions. 2007;38(7):1465.
23. Wu M, Ludwig A. A three-phase model for mixed columnar-equiaxed solidification. Metallurgical and Materials Transactions A. 2006;37(5):1613-31.
24. Ares A, Schvezov C. Solidification parameters during the columnar-to-equiaxed transition in lead-tin alloys. Metallurgical and Materials Transactions A. 2000;31(6):1611-25.
25. Ares A, Gassa L, Gueijman S, Schvezov C. Correlation between thermal parameters, structures, dendritic spacing and corrosion behavior of Zn–Al alloys with columnar to equiaxed transition. Journal of Crystal Growth. 2008;310(7):1355-61.

26. Ares A, Gueijman S, Schvezov C. An experimental investigation of the columnar-to-equiaxed grain transition in aluminum–copper hypoeutectic and eutectic alloys. Journal of crystal Growth. 2010;312(14):2154-70.

27. Mahapatra RB, Weinberg F. The columnar to equiaxed transition in tin-lead alloys. Metallurgical Transactions B. 1987;18(2):425.

28. Siqueira CA, Cheung N, Garcia A. Solidification thermal parameters affecting the columnar-to-equiaxed transition. Metallurgical and Materials Transactions A. 2002;33(7):2107-18.

29. Siqueira CA, Cheung N, Garcia A. The columnar to equiaxed transition during solidification of Sn–Pb alloys. Journal of Alloys and Compounds. 2003;351(1):126-34.

30. Canté MV, Cruz KS, Spinelli JE, Cheung N, Garcia A. Experimental analysis of the columnar-to-equiaxed transition in directionally solidified Al–Ni and Al–Sn alloys. Materials Letters. 2007;61(11):2135-8.

31. Spinelli JE, Ferreira IL, Garcia A. Influence of melt convection on the columnar to equiaxed transition and microstructure of downward unsteady-state directionally solidified Sn–Pb alloys. Journal of Alloys and Compounds. 2004;384(1):217-26.

32. Hachani L, Saadi B, Wang XD, Nouri A, Zaidat K, Belgacem-Bouzida A, et al. Experimental analysis of the solidification of Sn–3 wt.% Pb alloy under natural convection. International Journal of Heat and Mass Transfer. 2012;55(7):1986-96.

33. Hachani L, Zaidat K, Saadi B, Wang X, Fautrelle Y. Solidification of Sn–Pb alloys: Experiments on the influence of the initial concentration. International Journal of Thermal Sciences. 2015;91:34-48.

34. Liu DR, Mangelinck-Noël N, Gandin C-A, Zimmermann G, Sturz L, Thi HN, et al. Structures in directionally solidified Al–7wt.% Si alloys: Benchmark experiments under microgravity. Acta Materialia. 2014;64:253-65.

35. Liu DR, Mangelinck-Noël N, Gandin C-A, Zimmermann G, Sturz L, Nguyen-Thi H, et al. Simulation of directional solidification of refined Al–7wt.% Si alloys–Comparison with benchmark microgravity experiments. Acta Materialia. 2015;93:24-37.

36. Reinhart G, Gandin C-A, Mangelinck-Noël N, Nguyen-Thi H, Spinelli J-E, Baruchel J, et al. Influence of natural convection during upward directional solidification: A comparison between in situ X-ray radiography and direct simulation of the grain structure. Acta Materialia. 2013;61(13):4765-77.

37. Solidification. Lausanne: CRC Press; 2009.

38. Bellet M, Combeau H, Fautrelle Y, Gobin D, Rady M, Arquis E, et al. Call for contributions to a numerical benchmark problem for 2D columnar solidification of binary alloys. International Journal of Thermal Sciences. 2009;48(11):2013-6.

39. Combeau H, Bellet M, Fautrelle Y, Gobin D, Arquis E, Budenkova O, et al., editors. Analysis of a numerical benchmark for columnar solidification of binary alloys. IOP Conference Series: Materials Science and Engineering; 2012: IOP Publishing.

40. Kumar A, Založnik M, Combeau H, Goyeau B, Gobin D. A numerical simulation of columnar solidification: influence of inertia on channel segregation. Modelling and Simulation in Materials Science and Engineering. 2013;21(4):045016.

41. Kumar A, Založnik M, Combeau H. Study of the influence of mushy zone permeability laws on macro-and meso-segregations predictions. International Journal of Thermal Sciences. 2012;54:33-47.

42. De Felice V, Tveito K, Založnik M, Combeau H, M'Hamdi M, editors. Three-dimensional study of macro-and mesosegregation formation in a rectangular cavity cooled from one vertical side. IOP Conference Series: Materials Science and Engineering; 2012: IOP Publishing.

43. Li J, Wu M, Hao J, Kharicha A, Ludwig A. Simulation of channel segregation using a two-phase columnar solidification model–Part II: Mechanism and parameter study. Computational Materials Science. 2012;55:419-29.

44. Li J, Wu M, Hao J, Ludwig A, editors. Study of the channel segregation using a two-phase columnar solidification model. IOP Conference Series: Materials Science and Engineering; 2012: IOP Publishing.

45. Li J, Wu M, Hao J, Ludwig A. Simulation of channel segregation using a two-phase columnar solidification model–Part I: Model description and verification. Computational Materials Science. 2012;55:407-18.

46. Carozzani T, Gandin C-A, Digonnet H, Bellet M, Zaidat K, Fautrelle Y. Direct simulation of a solidification benchmark experiment. Metallurgical and Materials Transactions A. 2013;44(2):873-87.
47. Flood S, Hunt J. A model of a casting. Applied Scientific Research. 1987;44(1-2):27-42.
48. Beckermann C, Wang C. Equiaxed dendritic solidification with convection: Part III. Comparisons with NH4Cl-H2O experiments. Metallurgical and Materials Transactions A. 1996;27(9):2784-95.
49. Wang C, Beckermann C. Equiaxed dendritic solidification with convection: Part II. Numerical simulations for an Al-4 Wt pct Cu alloy. Metallurgical and Materials Transactions A. 1996;27(9):2765-83.
50. Wang C, Beckermann C. Prediction of columnar to equiaxed transition during diffusion-controlled dendritic alloy solidification. Metallurgical and Materials Transactions A. 1994;25(5):1081-93.
51. Sun Y, Beckermann C. Sharp interface tracking using the phase-field equation. Journal of Computational Physics. 2007;220(2):626-53.
52. Jasak H, Jemcov A, Tukovic Z, editors. OpenFOAM: A C++ library for complex physics simulations. International workshop on coupled methods in numerical dynamics; 2007: IUC Dubrovnik, Croatia.
53. Jasak H. OpenFOAM: open source CFD in research and industry. International Journal of Naval Architecture and Ocean Engineering. 2009;1(2):89-94.
54. Gündüz M, Hunt J. The measurement of solid-liquid surface energies in the Al-Cu, Al-Si and Pb-Sn systems. Acta Metallurgica. 1985;33(9):1651-72.
55. Cadirli E, Gündüz M. The directional solidification of Pb-Sn alloys. Journal of materials science. 2000;35(15):3837-48.
56. Imagumbai M. Behaviors of Manganese-Sulfide in Aluminum-killed Steel Solidified Uni-directionally in Steady State—Dendrite Structure and Inclusions. ISIJ International. 1994;34(11):896-905.
57. Imagumbai M. Relationship between primary-and secondary-dendrite arm spacing of C-Mn steel uni-directionally solidified in steady state. ISIJ International. 1994;34(12):986-91.

58. Zimmermann G, Sturz L, Nguyen-Thi H, Mangelinck-Noël N, Li Y, Gandin C-A, et al. Columnar and Equiaxed Solidification of Al-7 wt.% Si Alloys in Reduced Gravity in the Framework of the CETSOL Project. JOM. 2017;69(8):1269-79.

59. Wu M, Ludwig A. Modeling equiaxed solidification with melt convection and grain sedimentation—II. Model verification. Acta Materialia. 2009;57(19):5632-44.

60. Beckermann C, Wang C. Multiphase/-scale modeling of alloy solidification. Annual Review of Heat Transfer. 1995;6(6).

61. Steinbach I, Beckermann C, Kauerauf B, Li Q, Guo J. Three-dimensional modeling of equiaxed dendritic growth on a mesoscopic scale. Acta Materialia. 1999;47(3):971-82.

62. Steinbach I, Diepers H-J, Beckermann C. Transient growth and interaction of equiaxed dendrites. Journal of Crystal Growth. 2005;275(3-4):624-38.

63. Beckermann C, Viskanta R. Double-diffusive convection during dendritic solidification of a binary mixture. PhysicoChemical Hydrodynamics. 1988;10(2):195-213.

64. Ni J, Beckermann C. A volume-averaged two-phase model for transport phenomena during solidification. Metallurgical Transactions B. 1991;22B:349-61.

65. Založnik M, Combeau H. Thermosolutal flow in steel ingots and the formation of mesosegregates. International Journal of Thermal Sciences. 2010;49(9):1500-9.

66. Schneider MC, Beckermann C. Simulation of micro-/macrosegregation during the solidification of a low-alloy steel. ISIJ international. 1995;35(6):665-72.

67. Beckermann C. Modelling of macrosegregation: applications and future needs. International Materials Reviews. 2002;47(5):243-61.

68. Delaleau P, Beckermann C, Mathiesen RH, Arnberg L. Mesoscopic simulation of dendritic growth observed in X-ray video microscopy during directional solidification of Al–Cu alloys. ISIJ international. 2010;50(12):1886-94.

69. Souhar Y, De Felice VF, Beckermann C, Combeau H, Založnik M. Three-dimensional mesoscopic modeling of equiaxed dendritic solidification of a binary alloy. Computational Materials Science. 2016;112:304-17.

70. Melendez A, Beckermann C. Measurements of dendrite tip growth and sidebranching in succinonitrile–acetone alloys. Journal of Crystal Growth. 2012;340(1):175-89.

71. Nielsen Ø, Mo A, Appolaire B, Combeau H. Measurements and modeling of the microstructural morphology during equiaxed solidification of Al-Cu alloys. Metallurgical and Materials Transactions A. 2001;32(8):2049-60.

72. Rappaz M, Thevoz P. Solute diffusion model for equiaxed dendritic growth. Acta Metallurgica. 1987;35(7):1487-97.

73. Trivedi R, Kurz W. Dendritic growth. International Materials Reviews. 1994;39(2):49-74.

74. Dantzig JA, Rappaz M. Solidification: EPFL press; 2009.

75. Glicksman M, Koss M, Winsa E. Dendritic growth velocities in microgravity. Physical review letters. 1994;73(4):573.

76. Pines V, Chait A, Zlatkowski M, Beckermann C. Equiaxed dendritic solidification in supercooled melts. Journal of Crystal Growth. 1999;197(1-2):355-63.

77. Spencer BJ, Huppert HE. Steady-state solutions for an array of strongly-interacting needle crystals in the limit of small undercooling. Journal of Crystal Growth. 1995;148(3):305-23.

78. Souhar Y, De Felice VF, Založnik M, Combeau H, Beckermann C, editors. The role of the stagnant-film thickness in mesoscopic modeling of equiaxed grain envelopes. 4th International Conference on Advances in Solidification Processes (ICASP-4); 2016: IOP Publishing.

79. Torabi Rad M, Beckermann C. Validation of A Model for the Columnar to Equiaxed Transition with Melt Convection. CFD Modeling and Simulation in Materials Processing 2016: Springer; 2016. p. 85-92.

80. Boussaa R, Hachani L, Budenkova O, Botton V, Henry D, Zaidat K, et al. Macrosegregations in Sn-3 wt% Pb alloy solidification: Experimental and 3D numerical simulation investigations. International Journal of Heat and Mass Transfer. 2016;100:680-90.

81. Shevchenko N, Boden S, Gerbeth G, Eckert S. Chimney formation in solidifying Ga-25wt pct In alloys under the influence of thermosolutal melt convection. Metallurgical and Materials Transactions A. 2013;44(8):3797-808.

82. Shevchenko N, Roshchupkina O, Sokolova O, Eckert S. The effect of natural and forced melt convection on dendritic solidification in Ga–In alloys. Journal of Crystal Growth. 2015;417:1-8.

83. Underwood EE. Quantitative stereology for microstructural analysis. Microstructural Analysis: Springer; 1973. p. 35-66.